Layered solid state compounds for photocatalytic water splitting

Thesis Submitted to AcSIR for the Award of the Degree of

DOCTOR OF PHILOSOPHY
In CHEMISTRY

By
Soumya B. N.
(Enrollment No. 10CC11J26011)

Under the guidance of
Dr. R. Nandini Devi

Catalysis & Inorganic Chemistry Division
CSIR-National Chemical Laboratory
Pune- 411 008, India

August, 2015

राष्ट्रीय रासायनिक प्रयोगशाला
(वैज्ञानिक तथा औद्योगिक अनुसंधान परिषद)
डॉ. होमी भाभा रोड, पुणे - 411 008. भारत
NATIONAL CHEMICAL LABORATORY
(Council of Scientific & Industrial Research)
Dr. Homi Bhabha Road, Pune - 411008. India

CERTIFICATE

This is to certify that the work incorporated in this Ph.D. thesis entitled "**Layered solid state compounds for photocatalytic water splitting**" submitted by **Ms. Soumya B. N.** to Academy of Scientific and Innovative Research (AcSIR) in fulfillment of the requirements for the award of the Degree of **Doctor of Philosophy in Chemistry,** embodies original research work under my supervision/guidance. I further certify that this work has not been submitted to any other University or Institution in part or full for the award of any degree or diploma. Research material obtained from other sources has been duly acknowledged in the thesis. Any text, illustration, table etc., used in the thesis from other sources, have been duly cited and acknowledged.

Student
Soumya B. N.

Supervisor
Dr. R. Nandini Devi
Senior Scientist, CSIR-NCL, Pune, India
Assistant Professor, AcSIR, New Delhi, India

Communications Channels ☎ +91 20 25902000 +91 20 25893300 +91 20 25893400 Fax +91 20 25902601 (Director) +91 20 25902660 (Admin.) +91 20 25902639 (Business Development) URL : www.ncl-india.org

Declaration by the candidate

I hereby declare that the thesis entitled "**Layered solid state compounds for photocatalytic water splitting**" submitted for the award of the Degree of **Doctor of Philosophy in Chemistry** to the **Academy of Scientific & Innovative Research (AcSIR)**, New Delhi, has been carried out by me at Catalysis & Inorganic Chemistry Division, CSIR-National Chemical Laboratory, Pune-411008, India, under the supervision of Dr. R. Nandini Devi. The work is original and has not been submitted as a part or full by me for any degree or diploma to this or any other university.

August, 2015

Soumya B. N.

(Enrollment No. 10CC11J26011)

Dedicated to my parents

Acknowledgement

I express my deep sense of gratitude to my research guide Dr. R. Nandini Devi, who has always been very affectionately concerned, creatively helpful, and meticulously careful at every stage in the progress of my work. Her discretion and originality of thinking have significantly contributed to shaping my ideas in this thesis. I gratefully acknowledge her constant encouragement and support in the successful completion of this work.

My heartfelt thanks to Dr. P. A. Joy for valuable discussions and advice. I am thankful to Dr. T. G. Ajith Kumar for insightful suggestions, valuable opinions and fruitful collaboration work. I would like to express my gratitude to Dr. Ashok Kumar Yadav, Dibyendu Bhattacharyya and Dr. Shambu Nath (RRCAT, Indore) for EXAFS analysis. I would like to acknowledge Dr. Krishna K. Dey (Center of Biomedical Magnetic Resonance, Lucknow) for the solid state NMR analysis. I am thankful to my Doctoral Advisory Committee (DAC) members Dr. C. S. Gopinath, Dr. Mugdha Gadgil and Dr. P. A. Joy for continuously monitoring the progress of the research work and for scientific discussions. I sincerely acknowledge the help provided by Dr. T. Raja and Dr. Paresh L. Dephe. I am also thankful to Dr. K. R. Patil for XPS, Ketan and S.P. Dhanya for SEM. I acknowledge Mr. P. K. Mane and Mr. S. S. Deo for technical support during my Ph.D. I would like to thank Shibin, Sharanya and Akhil for assisting me at various stages.

It gives me immense pleasure to thank my labmates Dr. Kala Raj, Dr. Atul, Dr. Anupam Samanta, Dr. Rajesh, Jijil, Leena, Sumona, Sourik, Athira, Shibin, Monojit, Satej, Pranav Ghore and Anurag for their kind help and support, their prompt readiness to exchange perceptive ideas and the way they maintained a lively environment in the laboratory without which I could not have achieved this goal. I am obliged to the trainee students Remith, Rajith, Ali, Surya, Prakrithi, Saranya, Anantha, Shivesh, Sandhya, Ajay, Akhil and Fessy for their sincere cooperation.

I am thankful to my colleagues and friends, Dr. Eldho, Dr. Suresh, Alson, Venugopal, Dr. Vijaya Das, Hanumanth, Richa Bobade, Dr. Narasimha Rao, Nishitha, Srikanth, Atul, Laxmi, Lalit, Jay, Pranjal, Amlan, Dr. Ramakanta Sahu, Deepa, Anup Tathod, Presnjith, Sanil, Richa,

Tanusree, Sagar, Sandeep, Aneesh, Shoy, Jitesh, Prithi, Dr. Shivaranjini, Dr. Trupthi, Dr. Swathi, Atul, Vyshakh, Sunil, Sreedhala, Ashok, Periyasami, Manikandan, Aswathi, Dr. Khaja, Dr. Vijay, Mangesh, Govind, Jaya, Bindhu, Lenin, Mohan, Ram Sunder, Manjunath, Sharath K, Kiran, Sarath, Prajitha, Dr. Nisha, Dhanya, Bihag, Jaya C. Jose, Nishamol, Unnikrishanan, Anjali, Dr. Bhogesh, Dr. Prakash Chandra, Sreekuttan, Arun Torris, Anumon, Roshna, Aany, Hilda, Priya, Dr. Shijo, Dr. Prasanna Kumara, Renjith, Gireesh, Betsy, Sabareesh, Jeevan and Yadu for their indispensable help and for allowing me to spend wonderful time with them.

I would like to express deep affection to my friends Divya and Fousiya, who always stood by me encouraging and inspiring, never letting me down.

I would like to express my deep sense of gratitude to my parents and my brother for their enthusiastic encouragement, advice and moral support. Words are not enough to express my gratitude to my husband, Dr. A.V. Sijin Kumar, for his support, endless care, unconditional love and understanding throughout. I am thankful to my son, Aniruddh for not interrupting my work. I thank all family members for their constant encouragement to finish this work. Finally, my thanks are due to CSIR, Government of India, for awarding the research fellowship, and to Dr. S. Sivaram and Dr. Sourav Pal, former Directors, and Dr. Vijayamohanan K. Pillai, Director, CSIR-National Chemical Laboratory, for allowing me to carry out my research work by providing all possible infrastructural facilities, and for permitting me to submit this work in the form of a thesis for the award of Ph.D. degree.

Soumya B. N.

Table of Contents

Abstract

Hydrogen is considered as the greenest fuel for the planet for future. Generating hydrogen economically from an abundant and affordable raw material such as water will be the remedy for the future energy crisis. Water splitting is an uphill reaction and attaining overall photocatalytic water splitting is very tough as the reaction possesses a positive Gibbs free energy (+237 $KJmol^{-1}$). The discovery of photolytic cleavage of water into hydrogen and oxygen is attributed to Honda and Fujishima in 1972 using titania and a Pt electrode. Afterwards, extensive attempts have been carried out to develop semiconductors to produce hydrogen from water.

A suitable photocatalytic material should possess sufficiently small band gap for utilizing more abundant visible light region inthe solar spectrum. Also the valence band and conduction band positions with respect to the reduction and oxidation potentials of water should be appropriate to drive overall water splitting. On irradiation with light of appropriate energy, electrons and holes are generated in the bulk of the semiconductor particles, and they travel to the surface, eventually getting utilized in the reduction and oxidation reactions of water, respectively, on catalytically active surface sites or external cocatalysts deployed on the surface. During these processes, there are many possible pathways for recombination of the electron hole pair leading to a wastage of energy, most common being grain boundaries, lattice defects, as well as surface sites, which can be addressed by improving the sample characteristics. However, another important parameter depends on the structural characteristics of the valence and conduction bands. The photogenerated electrons and holes are generally located in conduction and valence bands, respectively, and in most of the semiconductors with bulk 3D structures, they are structurally close to each other enhancing the chances of recombination. Hence, structures with inherent separation of the photogenerated charges spatially, will be ideally placed for efficient photocatalysis.

Suppression of recombination of photogenerated charge carriers can be achieved by introducing layered system in which inherent charge or catalytic site separation exists. Hence, layered semiconductors have garnered attention as photocatalysts for hydrogen generation. Noted among them is the layered catalyst $K_4Nb_6O_{17}$ and its isomorphous compounds having general formula $A_4Ta_xNb_{6-x}O_{17}$ (A = Rb & K; x = 1- 4) introduced by Domen and co-workers which gives hydrogen evolution under UV irradiation. Other examples include 2D ordered perovskites like (110)-layered $La_2Ti_2O_7$, (100)-layered $La_2Ti_3O_9$, $Sr_2Ta_2O_7$ of Ruddlesden–Popper series and Dion-Jacobsen series layered perovskites $A'[A_{n-1}B_nO_{3n+1}]$ (A = K, Rb & Cs; B =Ca, Sr, Na & Pb; m = 2 – 4), all active under UV irradiation with NiO as cocatalyst.

Apart from these layered compounds, it is worthwhile to look at anisotropically structured compounds wherein inherent charge separation is possible by spatially separating charge generation sites and electron conducting pathways. A family of compounds has general formula $AMO_3(ZnO)_m$ (where A and M are trivalent metal ions of P block, m - integers) possessing significant spatial separation in charge generating and electron conducting sites. Kawazoe and co-workers suggested that layers formed by edge sharing MO_6 octahedra, where M is a p-block metal ion, may act as electron conducting pathways. Cobalt based compounds are well known for their oxygen evolution activity. Incorporation of an active hydrogen evolution site can be envisaged to be conducive for catalytic site separation within the compound. However photocatalytic water splitting studies of these types of materials are not investigated.

The thesis will be presented in five chapters, a brief summary of which is given below.

Chapter 1 presents a general introduction to photocatalytic water splitting reaction and a detailed literature survey of metal oxides used as photocatalysts. This chapter further discusses the principle behind the photocatalytic water splitting and the basic requirement of a material to act as a photocatalyst for water splitting. Detailed literature survey throws

light upon the role of various kinds of structured oxides in photocatalytic water splitting system. The structures and hydrogen evolution activities of many layered compounds including oxides and hydroxides are discussed. Finally the scope and objective of the thesis are stated.

Chapter 2 describes detailed structural studies and photocatalytic activities of layered oxides of the series $InGaO_3(ZnO)_m$ (m = 1–4) which are interesting due to their structural anisotropy. We have carried out synthesis of $InGaO_3(ZnO)_m$ (m – 1 to 4) and its bulk structural evaluation by various characterization methods such as ^{71}Ga MAS NMR, EXAFS at Ga and Zn K edge. The structure consists of sandwich layers of InO_6 edge shared octahedra leading to a stratified pattern. The outer strata consists of ZnO_4 tetrahedra and the inner strata has gallium oxide solubilized in ZnO. As m increases, concentration of tetrahedrally coordinated gallium and zinc also increases. The optical band gaps of $InGaO_3(ZnO)_m$ (m – 1 to 4) were determined using UV-vis spectroscopy and flat band potentials are calculated. These photocatalyst systems are found to be active for H_2 evolution from aqueous methanol solution even without a cocatalyst under UV irradiation. Incorporation of NiO cocatalyst enhanced the H_2 evolution activity by two fold. Incorporation of CuO acted as a sensitizer in which the accumulation of electrons in the conduction band of CuO made it a reduced species including Cu_2O phase which facilitated the interfacial electron transfer.

Chapter 3 describes photocatalytic activities of $InFeO_3(ZnO)_m$ series of oxides. The coordination geometries of Zn and Fe were analyzed using EXAFS. It is found that the oxygen coordination decreases as m increases and Fe is in pentacoordination for all the compounds. The optical band gaps were determined. The flat band potentials were calculated and it is found that there is a proper band alignment with the reduction potential of H^+/H_2. The hydrogen evolution activity was found to be enhanced from aqueous methanol.

Chapter 4 presents synthesis of nickel and zinc incorporation in layered $Co(OH)_2$. α and β-$Co(OH)_2$ are two polymorphs existing for layered $Co(OH)_2$, among this nickel doping is carried out in α-$Co(OH)_2$ due to its favourable structural features. The nickel doping in appropriate concentrations leads to higher photocatalytic hydrogen evolution activity from aqueous methanol under visible light irradiation. Two methods are followed for zinc incorporation, *viz*., post and *in situ* route. Simultaneous nickel and zinc incorporation through *in situ* route resulted in a mixed phase which could produce hydrogen in low yield from pure water under visible light irradiation. Zinc incorporation in nickel doped α-$Co(OH)_2$ is also found to be active in aqueous methanol under visible light.

Chapter 5 summarizes the results and conclusions based on the work reported in the thesis. This thesis reports the detailed structural characterizations and photocatalytic hydrogen activities of layered compounds having general formula $InMO_3(ZnO)_m$ (M - Ga & Fe, m - 1 to 4) which are reported to have spatial separation of photogenerated charge carriers due to the unique cationic environment. In addition, it also discusses the photocatalytic hydrogen evolution capability of cobalt based layered hydroxides having separate catalytic sites for H_2 and O_2 evolution.

List of Figures

List of Tables

List of Abbreviations

BET	Brunauer-Emmett-Teller
EJ	ExaJoule
EXAFS	Extended X-ray Absorption Fine Structure
FT	Fourier Transform
GC	Gas Chromatography
HER	Hydrogen Evolution Rate
ICP - AES	Inductively Coupled Plasma - Atomic Emission Spectroscopy
JCPDS	Joint Committee on Powder Diffraction Standards
LDH	Layered Double Hydroxide
MAS	Magic Angle Spinning
NMR	Nuclear Magnetic Resonance
OER	Oxygen Evolution Reaction
PXRD	Powder X-ray Diffraction
SEM	Scanning Electron Microscopy
TBP	Trigonal bipyramid
XPS	X-Ray Photoelectron Spectroscopy

Chapter 1

Introduction and Literature Survey

1.1. Introduction

Large scale consumption of fossil fuels in the last century consequent to industrial development has resulted in their drastic depletion, whereas their combustion causes serious environmental problems [1]. In this alarming situation the modern world is in search of a new form of energy that is clean, green, renewable and economical and hydrogen is considered the greenest fuel for the planet in the future, if produced from renewable sources, since its combustion product is water [2-6]. Currently, the major sources of hydrogen are based on non-renewable fossil fuels like natural gas or coal through thermochemical or catalytic pathways like steam reforming [7]. Other strategies are being developed to produce hydrogen from a more benign source like biomass; however, these processes also emit polluting gaseous products like CO and CO_2 [8].

In this scenario, generating hydrogen economically from an abundant and affordable raw material such as water using solar energy will be the most sustainable and environmentally friendly step towards achieving hydrogen economy [9]. Harnessing the abundant sunlight falling on earth has been a constant challenge to mankind. The average amount of the sun's radiation that penetrates the atmosphere and reaches earth is 51% of the total incoming energy. The rest are reflected back into space as well as absorbed by the atmosphere and clouds. The total solar energy absorbed by earth's atmosphere, oceans and land masses is approximately 3,850,000 EJ (EJ-exajoule, 10^{18} J) per year. The energy use by mankind is only ~ 500 EJ per year. This is about 0.01% of the total yearly energy coming from the sun. Putting this in another way, the earth absorbs more energy in one hour than the world uses in one year [10]. A good portion of the sun's radiation is in the visible range (46%) with 5% in ultra violet region and the rest exists as infrared radiation which is experienced as heat energy. Hence a proper utilization of the visible light spectrum of the solar irradiance, especially to produce hydrogen will be the ultimate convergence of sustainable energy solutions.

The conversion of solar energy into hydrogen via the water splitting process, assisted by photo-semiconductor catalysts, is one of the most promising technologies because large quantities of hydrogen can potentially be generated in a clean and

sustainable manner [11-15]. The process adapts two different schemes: (i) photoelectrochemical cells and (ii) photocatalytic systems. The photoelectrochemical cell for water decomposition involves two electrodes immersed in an aqueous electrolyte. One of the electrodes is a photocatalyst which is exposed to light and it is used as a semiconductor photoelectrode [16]. The term "photocatalysis" has been generally applied to the scheme in which powdered semiconductor is suspended in aqueous solution. The process can occur when solar radiation and semiconductor are used at ambient conditions. Here each particle of the suspended photocatalyst acts as an individual micro photoelectrode so that it can perform redox reactions of water on its surface [17]. Handling of powder photocatalyst system is simple and economical making it advantageous over photoelectrochemical cells. Moreover, in electrochemical cells, separation of the products formed during the reaction is a bottle neck and there is a possibility of reverse reaction also.

Photocatalytic reactions are of two types (Figure 1.1), one which is accompanied by positive Gibbs free energy and the other with negative free energy [18]. Water splitting into H_2 and O_2 possesses a Gibbs free energy of +237 KJ/mol, i.e., it is an uphill reaction, hence attaining overall photocatalytic water splitting is very tough. Here the process is similar to photosynthesis where solar (photon) energy is converted into chemical energy through certain chemical reactions. Therefore, this reaction is termed as "artificial photosynthesis" [4, 19]. On the other hand, photocatalytic reactions having negative Gibbs free energy are downhill reactions. Reactions involving photo oxidation of organic compounds mostly fall into this category and are usually irreversible [20].

The discovery of photolytic cleavage of water into hydrogen and oxygen, attributed to Honda and Fujishima in 1972 using titania and a Pt electrode, is considered a milestone on heterogeneous photocatalysis [21]. Afterwards extensive attempts have been done to develop semiconductors to produce hydrogen from water [22-24]. Large scale hydrogen production using suspended powder photocatalysts is considered to be beneficial over intricate multilayer or tandem structural devices.

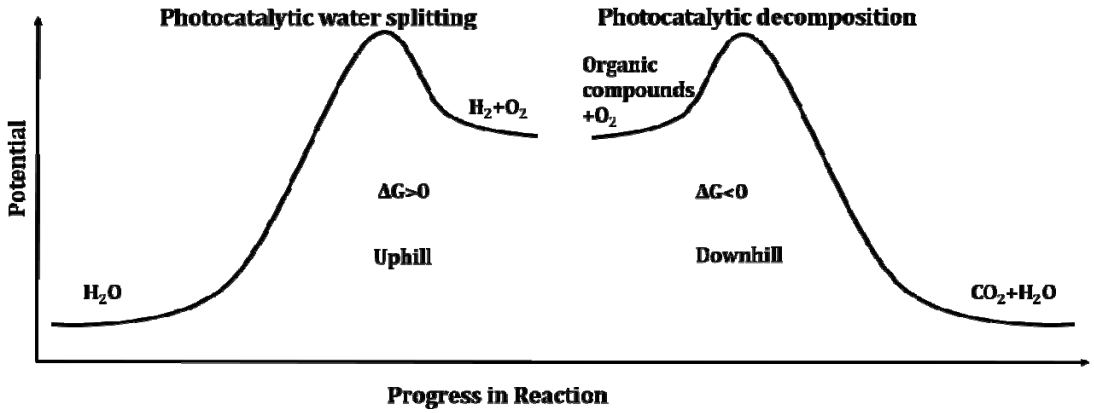

Figure 1.1. Energy profiles of photocatalytic water splitting and photocatalytic decomposition reactions. (Adapted from ref. [18]).

1.1.1. General Mechanism of Photocatalytic water splitting.

The general mechanism of photocatalytic water splitting using semiconductors is schematically represented in Figure 1.2.

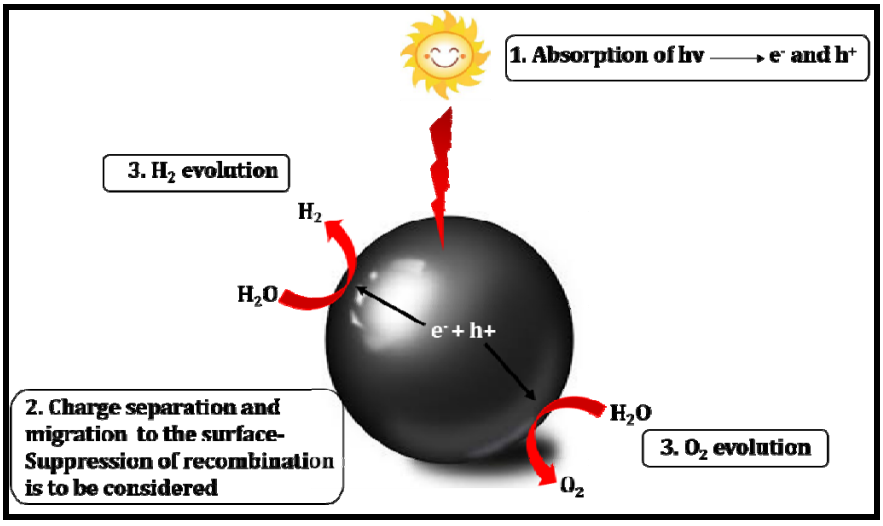

Figure 1.2. Schematic representation of various processes involved in photocatalytic water splitting reaction over a semiconductor material. (Adapted from ref. [25])

In the initial step, semiconductor photocatalyst on absorption of photon, generates electron-hole pairs known as excitons and the process can be considered as band gap excitation. When a photocatalyst is illuminated under radiation with energy equal to or

greater than the band gap energy, the valence band electrons can move on to the conduction band, leaving a positive hole in the valence band.

$$Photocatalyst \xrightarrow{h\nu} e_{CB}^{-} + h_{VB}^{+} \qquad (1.1)$$

To carry out the water splitting reaction, the electronic band structure of the semiconductor has to meet certain requirements. First of all, for photoreduction of water, the conduction band minimum of the semiconductor must be more negative than the reduction potential of H^+/H_2. In that case, the photogenerated electrons will transit from the conduction band minimum of semiconductor to H^+ and reduce it to H_2. Secondly, the valence band maximum of semiconductor must be more positive than the O_2/H_2O reduction potential. Then the hole left behind in the valence band will transit to water, which will get oxidized and produce O_2. To achieve better overall water splitting, the bottom of the conduction band must be located at a more negative potential than the reduction potential of H^+ to H_2 (0 V at pH 0), while the top of the valence band must be positioned more positive than the oxidation potential of H_2O to O_2 (1.23 V). Therefore, the minimum photon energy required thermodynamically to drive the reaction is 1.23 eV (Figure 1.3) [26].

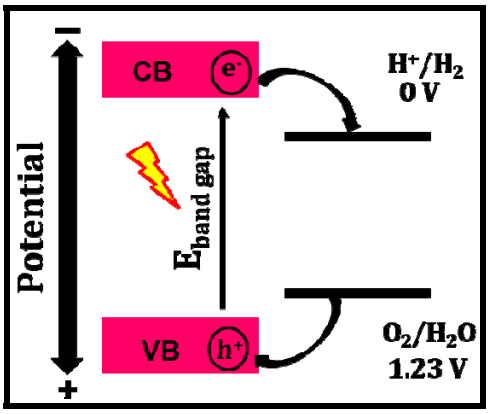

Figure 1.3. Schematic representation of the requirement of band alignment for photocatalytic water splitting (Adapted from ref. [26])

Photocatalytic oxygen evolution reaction (OER) is sluggish and requires large over potentials, because oxygen evolution from water is a four-electron reaction, while photon

capture is a single electron process [27]. The slow kinetics leads to the recombination of photogenerated charge carriers, which is one of the major bottlenecks for photocatalytic water splitting [28]. Even though semiconductors possess suitable band structure for photocatalytic water splitting, a lot among them undergo photocorrosion due to this phenomenon [29]. For example, ZnO upon band gap excitation follows the reaction:

$$ZnO + 2h^{+} \rightarrow Zn^{2+} + 1/2O_2 \qquad (1.2)$$

Here ZnO undergoes photocorrosion by photogenerated holes accompanied by the formation of Zn^{2+}. In such cases, sacrificial reagents (electron donors or hole scavengers) can be used to improve the H_2 evolution. As the accomplishment of overall water splitting is very difficult, sacrificial reagents are frequently availed to assess the photocatalytic activity for water splitting [30]. When the photocatalytic reaction is carried out in an aqueous solution along with a reducing reagent, photogenerated holes irreversibly oxidize the reducing reagent instead of water. It enriches photogenerated electrons in the conduction band of a photocatalyst, thereby enhancing H_2 evolution reaction [31]. Organic compounds, such as alcohols (methanol, ethanol, isopropanol, etc.), acids (formic acid, acetic acid, etc.), and aldehydes (formaldehyde, acetaldehyde, etc.), have been used as electron donors for photocatalytic hydrogen generation. Among them, methanol is the most widely used and studied sacrificial agent for the hydrogen generation process [32]. The suggested mechanistic routes are as follow [33].

$$h^{+} + H_2O \rightarrow \dot{O}H + H^{+} \qquad (1.3)$$

$$CH_3OH + \dot{O}H \rightarrow \dot{C}H_2OH + H_2O \qquad (1.4)$$

$$\dot{C}H_2OH \rightarrow HCHO + H^{+} + e^{-} \qquad (1.5)$$

$$2H_2O + e^{-} \rightarrow H_2 + 2OH^{-} \qquad (1.6)$$

Overall reaction $$CH_3OH \xrightarrow{Photocatalyst/h\nu} HCHO + H_2 \qquad (1.7)$$

Further HCHO reacts with water in the presence of the photocatalyst and light to give two more moles of hydrogen.

$$HCHO + H_2O \xrightarrow{Photocatalyst/h\nu} HCOOH + H_2 \qquad (1.8)$$

$$HCOOH \xrightarrow{Photocatalyst/h\nu} CO_2 + H_2 \qquad (1.9)$$

Valence band edge of most of the semiconductors is situated more positive to the reduction potential for the generation of hydroxyl radical. This can be observed in the case of photo-oxidation of alcohols where reductive hydroxyl radicals are formed. During methanol oxidation, α-hydroxymethyl radical (E_0 ($^{\cdot}CH_2OH/ CH_2O$) = −0.95 v NHE) is formed [34]. While using methanol as sacrificial agent, the same phenomenon can be expected whereby the radical formed in turn injects an additional electron into the conduction band of the photocatalyst (equation 1.4). Here a single photon can generate two photoelectrons, one from band gap excitation and another from electron injection by hydroxyl radical. This phenomenon is called current doubling effect [35]. It is expected that many photocatalysts which would otherwise undergo photocorrosion can be employed for hydrogen generation from water if a sacrificial reagent is present in the reaction system.

The second step in the semiconductor photocatalytic water splitting involves the charge separation of the photogenerated charge carriers in bulk and their migration to the surface of the semiconductor. The photogenerated charge carriers can also be trapped at defect sites which constitute grain boundaries, structural defects like ion vacancies as well as interstitial defects [36]. This is strongly affected by the crystal structure, crystallinity and particle size. If a photocatalyst possesses poor crystalline quality, there will be higher number of defects, resulting in increased recombination. There is decrease in recombination probability of photogenerated charge carriers in the case of photocatalysts with small particle sizes due to the shortened reaction path for the electrons and holes to the surface [37]. However, nano sized particles may have the disadvantage of decreased

crystallinity as well as increased surface trap sites. Hence an ideal material will show an interplay of all these parameters.

The final step involves the surface chemical reactions and it depends on the surface character and quantity. The holes and electrons which are migrated to the surface can oxidize and reduce surface adsorbed molecules, respectively, through interfacial charge transfer. These reactions are the basic mechanistic steps for the photocatalytic water splitting to produce hydrogen [38]. The overall reactions involved in photocatalytic water splitting are,

$$4h^+ + H_2O \rightarrow O2 + 4H^+ \quad (1.10)$$ (water oxidation half reaction)

$$2e^- + 2H^+ \rightarrow H_2 \quad (1.11)$$ (water reduction half reaction)

$$H_2O \rightarrow H_2 + 1/2O_2 \quad (1.12)$$

Another essential requirement for photocatalytic water splitting is the presence of active sites for redox reactions on the surface of the catalyst. The unavailability of active sites leads to recombination even if the photogenerated holes and electrons possess thermodynamically ample potentials for water splitting [39]. Usually, this problem can be solved by loading the photocatalyst with co-catalysts of noble metals, such as Pt, Pd, Au and Ag and metal oxides such as, NiO and RuO_2, having a low over potential for hydrogen evolution [40]. That is, conduction band levels of most of the oxide photocatalysts are not high enough to reduce water to give H_2. However, these co-catalysts can create active sites on the surface of the photocatalysts, thereby generating hydrogen [41].

1.1.2. Strategies to utilize visible light by a photocatalyst.

Even though enormous number of metal oxides are identified as potential photocatalysts for water splitting, most of the reported catalysts work under UV irradiation [45]. Various methods are suggested to achieve visible light activity in these oxides such as doping, using sensitizers etc. Band engineering plays a pivotal role in making a

photocatalyst visible light active (Figure 1.4) [42]. The conduction band level of oxide semiconductors are composed of empty metal orbitals. The valence band is usually associated with the filled O 2p orbitals. Band energy can be tailored to utilize visible light wavelengths by introducing a new donor level near to the valence band consisting usually of filled O 2p orbitals. The newly formed valence band should be accompanied by sufficient thermodynamic potential and kinetic consideration for oxidation of water into oxygen [43]. Since the dopants may contribute to recombination centres due to the charge imbalance, co-dopants can be added as they can even off the problem. For example, $SrTiO_3$ co-doped with Cr^{3+}/Ta^{5+} is an active photocatalyst for H_2 evolution. Here Cr^{3+} dopant forms electron donor levels in the band gap of the $SrTiO_3$ host materials, resulting in visible light response. When Ti^{4+} is replaced with Cr^{3+}, the charge becomes unbalanced. This may result in the formation of recombination centres. Co-doped metal cation Ta^{5+} compensates the charge imbalance, resulting in the suppression of the formation of recombination centres and maintaining the property of visible light absorption [44]. The additional level formed after doping may face lack of kinetic ability to oxidise water due to the discreteness in the valence band level and thus migration of photogenerated holes is retarded. It is desirable to have the valance band levels associated with orbitals other than O 2p. It is understood that orbitals of 6s in Pb^{2+}, 6s in Bi^{3+}, 5s in Sn^{2+} and 4d in Ag^{+} can form valence bands above O 2p making the band gap narrower [45].

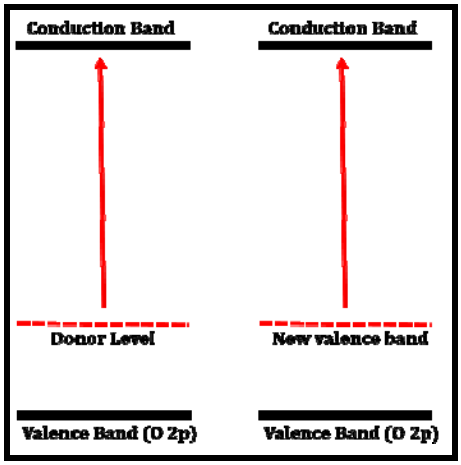

Figure 1.4. Strategies of tuning the band structure for the design of visible light driven photocatalysts. The electron donor level is created above the valence band by doping some elements into conventional photocatalysts with wide band gaps. (Adapted from ref. [42])

Anion doping is also a well-accepted way to introduce visible light activity. Energy states of doped anions (non-metal ions) hybridize well with the valence band states of the semiconductor oxide material, and either shift the valence band upward or broaden, resulting in the reduction of the overall band gap. Anion doping with N^{3-}, C^{4-} or S^{2-} is expected to make a photocatalyst absorb in the visible light regime [46]. Among these, nitrogen doping can be expected to give promising materials because of the ample overlapping of O 2p and N 2p states which reduces the effective band gap [47]. Doping with sulphur will also lead to the same effect but the large ionic radius of sulphur will hinder the proper incorporation of it into the oxygen lattice. However, C and P doping is found to lead to recombination centres [48]. Making solid solution is one of the methods for band engineering. This will reduce the effective band gap by introducing new electronic levels. CdS-ZnS solid solution is active for visible light hydrogen production and it is worth to note that ZnS and CdS possess the same crystal structure [49]. Another strategy to make visible light driven photocatalysts is to incorporate sensitizers capable of absorbing visible light. It is already reported that various metal complexes and dyes loaded with wide band gap semiconductors such as TiO_2 and $K_4Nb_6O_{17}$ can split water under visible light [50-51].

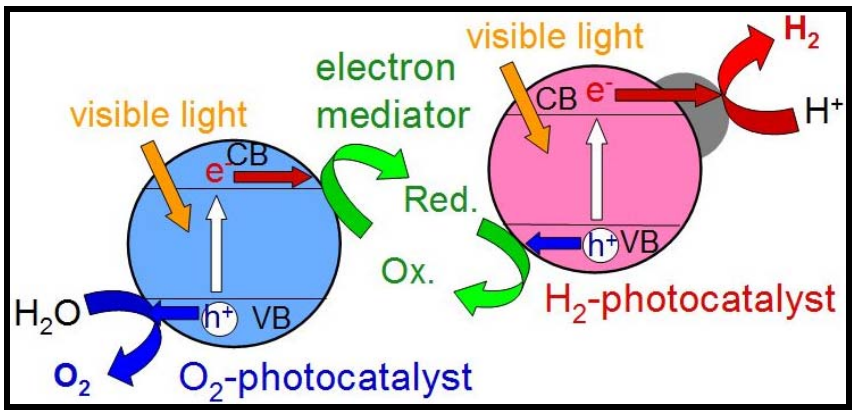

Figure 1.5. Z scheme for photocatalytic water splitting which uses photocatalytic water splitting through two-step photoexcitation using two different semiconductors and a reversible electron mediator (Reproduced from ref. [52]).

Visible light irradiation can be efficiently utilized in the Z scheme water splitting which was originally introduced by Prof. A. J. Bard [53]. The natural photosynthesis follows Z scheme in which photosystem I and photosystem II play major roles. Similarly in the so

called Z scheme photocatalysis (Figure 1.5), two different kinds of photocatalysts are jointly used as a redox mediator. Here the systems must have two excitation centres. Usually the first system produces hydrogen and an oxidizing agent which is used up by the second system to produce oxygen [54].

1.1.3. Metal oxides as photocatalysts for H_2 evolution

From this discussion it is clear that the semiconductor systems for photocatalytic water splitting should possess optimized band gap so as to make maximum utilization of solar radiation, along with sufficient chemical stability against photocorrosion. Many types of semiconductors comprising oxides, nitrides, oxynitrides, sulphides, carbides, phosphides, solid solutions and perovskite type materials, inorganic complexes, etc. have been reported to be impressive candidates as photocatalysts for hydrogen evolution via water splitting [55-57]. Of these, oxides starting from simple ones like, ZnO, TiO_2, ZrO_2, SnO_2 etc. to complex oxides like perovskites and related materials are reported to be active in photocatalytic hydrogen evolution. Among the simple oxides, titania becomes prominent because of its favourable band gap, high chemical and photochemical stability, biological inertness, low cost, ease of method of preparation, etc.

Titania (TiO_2) was the first material identified as a photochemical water splitting catalyst. It crystallizes in three different structures, rutile (band gap=3.0 eV), anatase (band gap=3.15 eV) and brookite. All these crystal types contain interconnected TiO_6 octahedra. Fujishima and Honda reported oxygen evolution and a current flow in n-type TiO_2 (rutile) anode and a Pt black cathode respectively, in a photo-electrochemical cell. They used UV light irradiation from a 500 W Xe lamp [58]. Afterwards Wrighton *et al.* found photoelectrochemical water splitting for the generation of H_2 and O_2 under similar conditions [59]. Schrauzer *et al.* first reported the powder photocatalytic water splitting using TiO_2 [60]. Conversely, Van Damme and Hall reported that the photolysis of water occurs due to the decomposition of hydroxyl groups on the TiO_2 surface [61]. Kawai *et al.* showed that D_2 was generated when TiO_2 powder was irradiated in the presence of D_2O vapour [62]. Initial attempts of titania modifications were suggested by Nozik *et al.* They proposed the concept of photochemical diodes, either p-n type fused semiconductors or

Shottky type devices such as n-CdS/Pt. The higher efficiency of these materials compared to normal catalysts is attributed to the formation of space charge layer at the interface which in turn leads to more electron-hole separation [63]. The use of Pt as cocatalyst in TiO_2 for photocatalytic water splitting system was first tried by Sato *et al.* The presence of noble metals on titania surface leads to the formation of a Schottky barrier at the metal/semiconductor interface which in turn decreases electron-hole recombination rate. They added Pt on TiO_2 by photodecomposition of hexachloroplatinate and confirmed O_2 evolution by isotopic labelling. Pt can also catalyse the reverse reaction which limits the yields of hydrogen at high H_2 partial pressure [64]. Following earlier work on molecular dyes, Prof. Michael Grätzel pioneered in developing multicomponent systems and subsequent utility of visible light. Doped TiO_2 along with Pt cocatalyst and RuO_2 evolved stoichiometric amounts of H_2 and O_2 under UV irradiation. In this system photogenerated electrons and holes from TiO_2 are transferred to Pt and RuO_2 respectively and proceed for subsequent redox reactions [65]. They found that sensitizer $[Ru(bpy)_3]^{2+}$ can make TiO_2 a visible active catalyst. The photo generated electrons on the $[Ru(bpy)_3]^{2+}$complex are transferred to TiO_2, which acts as an electron acceptor. In a further step, Pt takes up the electrons and oxidizes water [66]. Incorporation of Na_2CO_3 in the reaction medium can enhance the oxygen evolution by TiO_2 and it can be assumed that the peroxycarbonate species releases oxygen [67-68]. Recent reports on TiO_2 catalysts include tandem systems with isolated reduction and oxidation sites [69]. Another important attempt on TiO_2 based photocatalytic water splitting is the band gap engineering through cation and anion doping [70]. Especially, anion doping has its own advantages on visible light response which is attributed to the conduction band positions contributed by the anion *p* orbitals. C, N and S doping are reported in literature of which N-doped TiO_2 has attracted most attention for photocatalytic water splitting under visible light irradiation [71].

ZrO_2 is also an active photocatalyst for total water splitting under UV irradiation. ZrO_2 crystallizes in the rutile structure type and it possesses a band gap of 5.0–5.7 eV [72]. An interesting feature of ZrO_2 is that it can split water even without a cocatalyst and the activity decreases in the presence of cocatalysts, such as Pt, Cu, and Au. This is attributed to

the wide band gap and the alignment of conduction and valence band with the redox potential of water.

Ta_2O_5 possesses a band gap of 4 eV and it can produce H_2 from pure water under UV irradiation. When modified with cocatalyst such as Pt, NiO or RuO_2 it gives 190 μmol/g/h with stoichiometric O_2 yield. Also it can produce 115μmol/h/g and 530 μmol/h/g H_2 and O_2 respectively under irradiation from a combination of 400–450W Hg lamp in a quartz cell [73-74].

In the presence of appropriate redox agents, oxides of Ga, In, Sb, Sn and Ge are found to be active for water splitting. In_2O_3 possesses a band gap energy of ~3 eV. The quantity of hydrogen evolved when dispersing 0.5 g of Pt modified In_2O_3 mixed with Cr doped In_2O_3 into an aqueous solution of methanol is 0.36 μmol/h under UV irradiation. Suitable modification with NiO leads to hydrogen evolution from pure water [75]. Cuprous oxide, Cu_2O with a band gap of 2 eV evolves small but stoichiometric rates of H_2/O_2 under visible light irradiation from pure water [76]. Apart from the above mentioned simple metal oxides, complex oxides of Ti, Ta, In etc. are also found to be active for photocatalytic water splitting reactions.

These include interesting structured oxides like perovskite $SrTiO_3$ (Figure 1.6), a series of layered perovskites and other complex oxides. $SrTiO_3$ adopts a complex structure of corner shared TiO_6 octahedra with Sr occupying the cuboctahedral cavity and has a band gap of 3.2 eV which is comparable with that of TiO_2 [77]. Domen *et al.* reported hydrogen production from water vapour while irradiating UV radiation onto NiO-modified $SrTiO_3$ [78]. In another report, an interesting design with Cr/Ta doped $SrTiO_3$ modified with Pt cocatalyst followed Z–scheme mechanism by coupling with Pt-WO_3, produced hydrogen under visible light. They used an iodide/iodate redox couple as redox mediator between the two catalysts [79]. Kim *et al.* found that doping Pb^{2+} in $Sr_3Ti_2O_7$ results in $PbTiO_3$ having perovskite structure and band gap of 2.8 eV. It can produce H_2 from aqueous methanol and $AgNO_3$ after modifying with Pt cocatalyst under visible light irradiation [80].

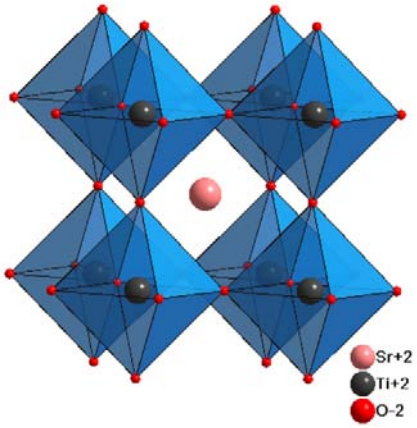

Figure 1.6. Crystal structure of perovskite $SrTiO_3$ consists of corner shared TiO_6 octahedra with Sr in cuboctahedral cavity.

In late 1990s, $MTaO_3$ (M - Li, Na, K) compounds which crystallize in perovskite structure, were reported to be very effective photocatalysts for water splitting under UV irradiation. The band gaps of $LiTaO_3$, $NaTaO_3$ and $KTaO_3$ are 4.7 eV, 4.0 eV, and 3.7 eV respectively which indicate that the band gap energy depends on the M site cations [81]. $NaTaO_3$ modified with NiO cocatalyst is the best catalyst among the three and it can produce 2.18 mmol/h with a quantum yield of 20% [82]. In 2003, Kato *et al.* showed that NiO modified 0.2 wt% La doped $NaTaO_3$ prepared by solid state method could produce hydrogen from pure water under UV irradiation with a quantum yield of 56% (19.8 mmol/h), which is the highest quantum efficiency ever reported. The higher quantum efficiency is related to the La doping and consequent reduction in particle size which leads to formation of nanosteps on the photocatalyst surface. As shown in Figure 1.7, hydrogen formation is on NiO cocatalyst and O_2 is evolved in the grooves of the nanosteps [83].

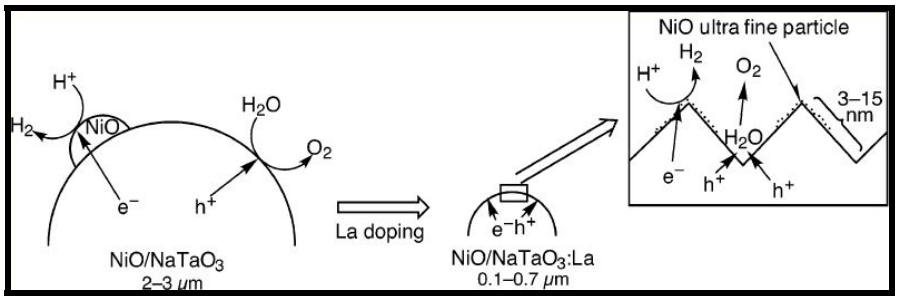

Figure 1.7. Mechanism involved in the hydrogen production from pure water by NiO modified 0.2 wt% La doped $NaTaO_3$. (Reproduced from ref. [83])

Doping different transition metals such as Ti, Zr and Hf in $KTaO_3$ enhances water splitting activity of $KTaO_3$, but it is not comparable with La doped $NaTaO_3$. Ti doped $KTaO_3$ is found to be fairly active because of the reduced octahedral distortion thereby creating effective pathway for electron migration which is related to the cationic radius [84]. Ishihara and co-workers found that Zr doped $KTaO_3$ crystals coupled with tetraphenylporphyrinatochromium(III) and Pt particles are active water splitting catalysts under UV irradiation (QE ~ 12.8%). Here, the photogenerated electron is efficiently transported over porphyrin complex to the Pt particle on the surface of the Zr:$KTaO_3$ [85]. In 2006, Lin *et al.* reported that $NaTaO_3$ produced by a sol–gel method possesses a slightly higher band gap of 4.1 eV and can split water with higher efficiency. This is attributed to a large surface area and the phase transition from orthorhombic to monoclinic [90]. Kato *et al.* reported the photocatalytic water splitting activities of $SrTa_2O_6$ (Eg=4.5 eV), which consists of TaO_6 edge shared octahedra [86]. Orthorhombic $BaTa_2O_6$ possesses a band gap energy of 4.1 eV and was found to be active under UV irradiation [87]. Another noted material is $NiTa_2O_6$ which can produce hydrogen even without a cocatalyst. The presence of edge shared octahedra is desirable for effective migration of photogenerated electrons [74]. Apart from these, pyrochlore type oxides are also capable of catalyzing water splitting under solar light. One such kind of material is $Ca_2Ta_2O_7$ which consists of 3D network of corner shared octahedra. Ikeda *et al.* found that NiO modified $Ca_2Ta_2O_7$ shows fairly good activity towards overall water splitting under UV irradiation from pure water [88]. $Bi_2MTa_2O_7$ (M – La and Y) also crystallize in pyrochlore structure and are slightly active under visible light irradiation [89].

$Ba_2In_2O_5$ crystallizes in the brownmillerite structure type and under visible light irradiation, Pt-modified $Ba_2In_2O_5$ generates small amounts of H_2/O_2 from aqueous solutions of methanol and $AgNO_3$, while NiO-modified $Ba_2In_2O_5$ evolves H_2 from pure water. Cr doped $Ba_2In_2O_5$ coupled with Cr doped In_2O_3 produces 29.3 μmol/h/0.5 g from pure water [90]. RuO_2 modified $CaIn_2O_4$, $SrIn_2O_4$ and $LaInO_3$ possess a network of edge shared octahedra and are found to be active for photocatalytic water splitting under UV radiation [91]. A mixture of Zn doped Lu_2O_3 and β-Ga_2O_3 engenders hydrogen with a quantum efficiency of 6.8% at 320 nm from aqueous methanol with suitable modification with NiO while the

individual oxides are not active. The structure of β-Ga_2O_3 consists of corner and edge shared GaO_6 octahedra and GaO_4 tetrahedra and it has a band gap of 4.6 eV whereas Lu_2O_3 crystallizes in a defect fluorite structure with ¼ of the oxygen site vacant [92]. $ZnGa_2O_4$ consisting of edge shared GaO_6 octahedra and ZnO_4 corner shared tetrahedra is capable of splitting pure water under UV irradiation [93]. Sato *et al.* found that weberite class of compounds, $Ca_2Sb_2O_7$ and $Sr_2Sb_2O_7$ are active under UV irradiation with RuO_2 loading [94]. They further reported that $NaSbO_3$ having ilmenite crystal structure can evolve hydrogen with RuO_2 cocatalyst. $NaSbO_3$ consists of layers of corner shared SbO_6 octahedra separated by Na^+ cations [95]. Willemite structured Zn_2GeO_4 consisting of 3D network of corner shared tetrahedra of the different cations, works as a UV active catalyst with RuO_2 modification [96].

Other than the above mentioned transition metal oxides, Cr and W based oxides with suitable electron donors or acceptors can also catalyse photocatalytic water splitting. Abe *et al.* showed that Pt-modified WO_3 coupled with Cr/Ta-doped Pt-$SrTiO_3$ forms a visible light active catalyst for overall water splitting [97]. The scheelite structured Mo based photocatalysts, $PbMoO_4$ and Cr/$PbMoO_4$, have the ability to split water. Both contain MoO_4 tetrahedra with Pb ions in between. The Cr content makes the photocatalyst visible light active [98-99].

In all these systems, solar energy is converted into chemical energy for which absorption of solar energy is expected to produce electron and hole pairs. The conduction and valence bands of most of the bulk 3D structures are structurally close to each other which renders the recombination of photogenerated charge carriers easier [100]. Hence layered compounds with well separated catalytic sites for hydrogen and oxygen generation within the photocatalyst instead of complex tandem systems, started generating interest among the scientific community. Further, researchers also looked into compounds having layered structure with well defined electron conduction pathways away from charge generation sites minimising recombination losses.

1.1.4. Layered compounds as photocatalysts for H_2 evolution

Layered compounds for photocatalytic water splitting can be considered to be of two types. The widely used photocatalytic systems possess separate catalytic sites either inherently or with the aid of other materials. The ideal and rarely studied class of layered photocatalysts are those having an inherent spatial separation of photogenerated charge carriers within the compounds. Figure 1.8 clearly shows the classification among the photocatalysts.

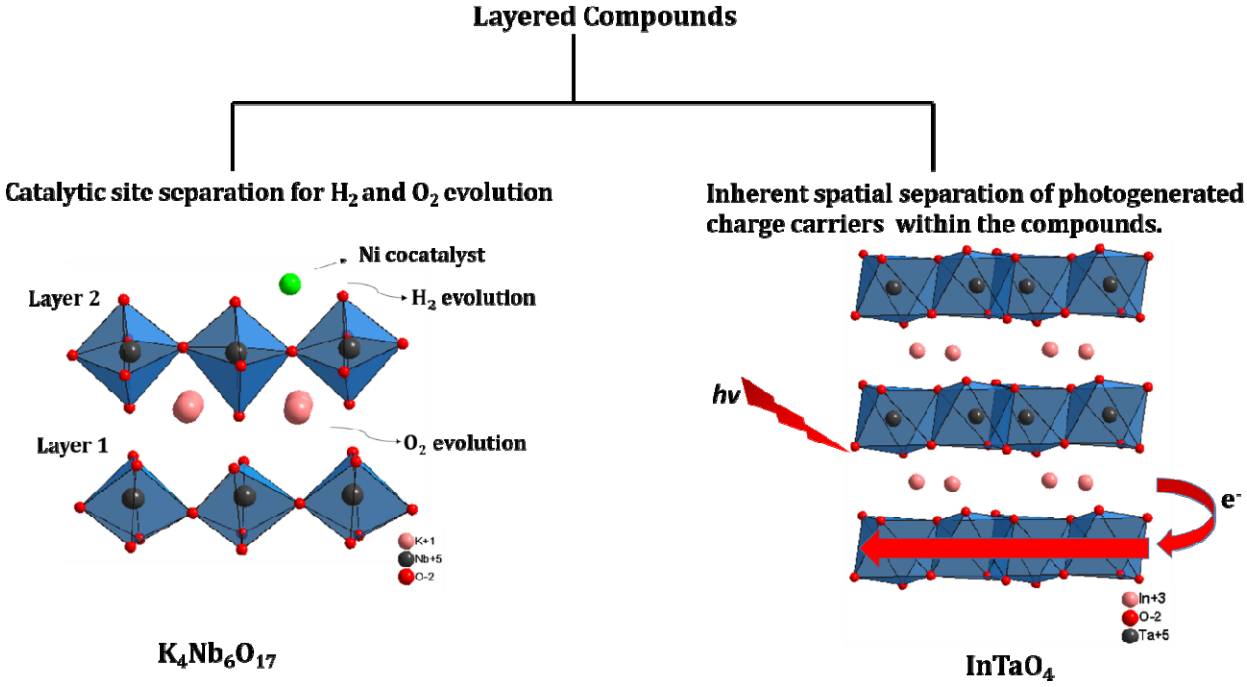

Figure 1.8. Two types of layered materials considered for photocatalytic water splitting. Left: Photocatalyst possesses interlayers which are capable of ion exchange and cation intercalation leading to catalytic site separation. Right: Photocatalyst with inherent spatial separation of electrons and holes due to the separation in charge generation as well as conduction pathways.

1.1.4.1. Catalytic site separation in photocatalysts

A wide variety of layered oxides with catalytic site separation are found to be potential candidates for photocatalytic hydrogen generation in the past several years. The

interlayers in these kinds of materials play a distinct and significant role in the reaction mechanism. Layered perovskites are a broad class of materials among them. The (110)-layered perovskite $La_2Ti_2O_7$ consists of TiO_6 corner shared octahedral slabs which are separated by layers of La^{3+} ions. It requires UV irradiation for catalytic activity as it possesses a band gap of 3.8 eV [101]. $La_2Ti_3O_9$ is a (100)-layered perovskite capable of absorbing UV radiation and after suitable modification with NiO, $La_2Ti_3O_9$ splits water at a low rate [102]. $Sr_3Ti_2O_7$ is a (100)-layered perovskite of the Ruddlesden–Popper series having band gap energy of 3.2 eV which is capable of catalysing hydrogen evolution under UV irradiation [103]. $CaBi_4Ti_4O_{15}$ belongs to Aurivillius-type layered perovskites, and consists of layers of TiO_6 octahedral sheets separated by layers of $[Bi_2O_2]^{2+}$ as shown in Figure 1.9a. Substitution of Ca^{2+} with Pb^{2+} enables the catalyst to work in the visible light [104].

The layered tantalates having the general formula $A_4Ta_xNb_{6-x}O_{17}$ (A = Rb, K; x = 1-4) were studied for their water splitting activity by Domen and co-workers [105]. These compounds are isomorphous with $K_4Nb_6O_{17}$. The band gaps in this series increase with the Ta content. All materials split water under UV irradiation with suitable modification with NiO. The renowned layered catalyst $K_4Nb_6O_{17}$, introduced by Domen and coworkers, gives non-stoichiometric hydrogen evolution without a cocalyst. The material has a band gap of 3.3 eV. Further modification with NiO increases its activity. $K_4Nb_6O_{17}$ photocatalyst possesses two kinds of interlayers in which ion-exchangeable potassium cations exist as shown in Figure 1.9b. H_2 evolution proceeds in one interlayer with a nickel co-catalyst while O_2 evolution occurs in another interlayer. Here separation of the catalytic sites is achieved in which H_2 evolution and O_2 evolution reactions are separated by a photoactive niobate sheet. The greatest achievement regarding this material is that it is active for water splitting even without a cocatalyst from an aqueous methanol solution [106].

$Sr_2Ta_2O_7$ (Figure 1.10) belonging to Ruddlesden–Popper layered perovskite is a good catalyst for the overall splitting of water with NiO as the cocatalyst [113]. Upon UV irradiation, the compounds of the type $M_2La_{2/3}Ta_2O_7$ (M = H, K) and $H_2SrTa_2O_7$ split water into H_2/O_2 after modification with NiO. Here the TaO_6 layers are separated by layers of K^+

or H^+ ions [107]. Surface modifications of $Sr_4Ta_2O_9$ and (111)-layered perovskite $M_5Ta_4O_{15}$ (M = Sr, Ba) when loaded with NiO produce hydrogen from pure water. Their band gaps lie in UV region [108-109]. Under UV irradiation and with cocatalyst NiO, modified layered perovskites of the Dion-Jacobsen series $RbLnTa_2O_7$ (Ln = La, Pr, Nd, Sm) show fairly good activity for photocatalytic water splitting [110]. The water-splitting activity of other Dion-Jacobsen series of layered perovskite $A'[A_{n-1}BnO_{3n+1}]$ (A = K, Rb, Cs; B =Ca, Sr, Na, Pb; m = 2–4) were studied with Pt modification in methanol water mixture under UV irradiation. These materials consist of corner-shared BO_6 octahedra with A ions located in the metal oxide layers and A' ions between them. The catalytic activity considerably increases on the exchange of Ca^{2+} and Sr^{2+} ions with H^+ [111]. $HCa_2Nb_3O_{10}$ produces 5.9 mmol/h/g H_2, and when it is modified with Pt, the rate increases to almost 5 times [112].

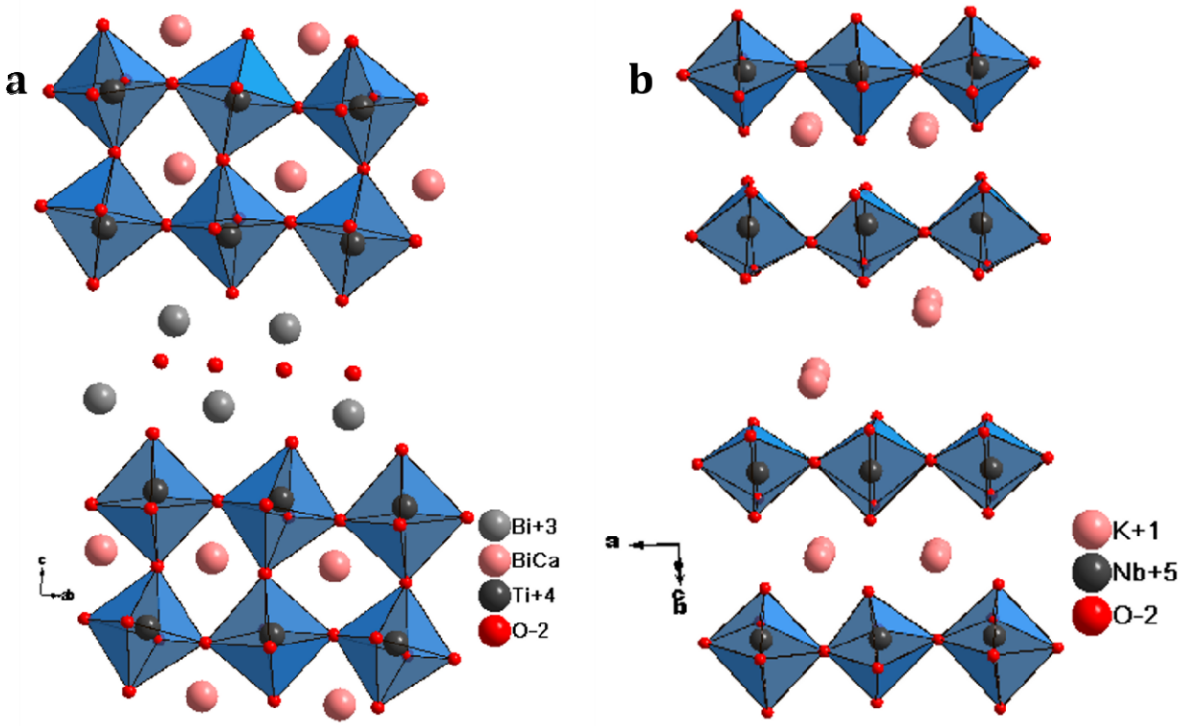

Figure 1.9. Crystal structures of (a) $CaBi_4Ti_4O_{15}$ and (b) $K_4Nb_6O_{17}$, clearly show the possibility of ion exchange which promotes the water intercalation and further water splitting.

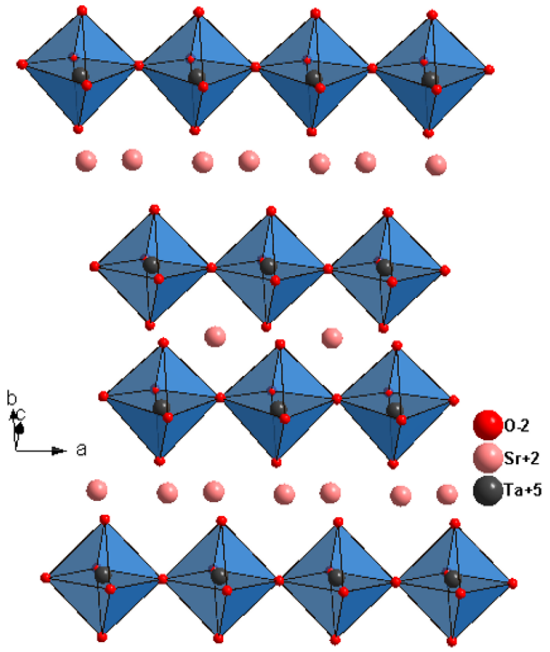

Figure 1.10. Crystal structure of $Sr_2Ta_2O_7$. The layered structure enhances the photocatalytic hydrogen evolution by separating the catalytic sites on Ta and oxygen.

The Aurivillius-type layered perovskites, $PbBi_2Nb_2O_9$ is visible light active with a band gap of 2.88 eV and it can produce hydrogen from aqueous methanol [113]. Another member of this family is Bi_3TiNbO_9, which generates H_2 under UV irradiation [114]. $Na_2W_4O_{13}$ possesses structurally separated layers which contribute to hydrogen production [115]. Typically, most of these structures consist of sheets of transition metal oxides separated by alkali or alkaline earth metal ions, giving rise to anisotropy to a certain extent, restricting movement of charges through interlayer spaces. However, in these layered compounds, attempt is made to introduce catalytic sites within the interlayer spaces, thereby achieving partial space separation of the charges or spatially separate H_2 and O_2 evolution sites reducing the backward reaction. In all these compounds, focus is on the incorporation of water into the interlayer and consequent separation of catalytic sites. It is suggested that water incorporation raises the interfacial area and reduces the essential distance for charge transfer [23].

In the current discussion of layered compounds, it is imperative to mention layered hydroxides, as this family of compounds possess interesting ion exchange properties. A

vast variety of layered hydroxides are associated with divalent cations which have been extensively studied for their electrochemical and other catalytic applications [116-118]. These types of compounds are well known for their capability of ion exchange in the interlayer region. These include α-hydroxides of nickel and cobalt and layered hydroxy double salts such as $Zn_5(OH)_8(NO_3)_2{\cdot}2H_2O$ and $Ni_{1-x}Zn_{2x}(OH)_2(CH_3CO_2)_{2x}{\cdot}nH_2O$ [118-120]. The simple layered hydroxide structure contains a close packed array of octahedra generated by a divalent metal ion and six hydroxyl oxygen atoms to form a layering pattern similar to that of brucite. These two dimensional metal-hydroxyl sheets stack via hydrogen bonding to form a three-dimensional structure (Figure 1.11) [121].

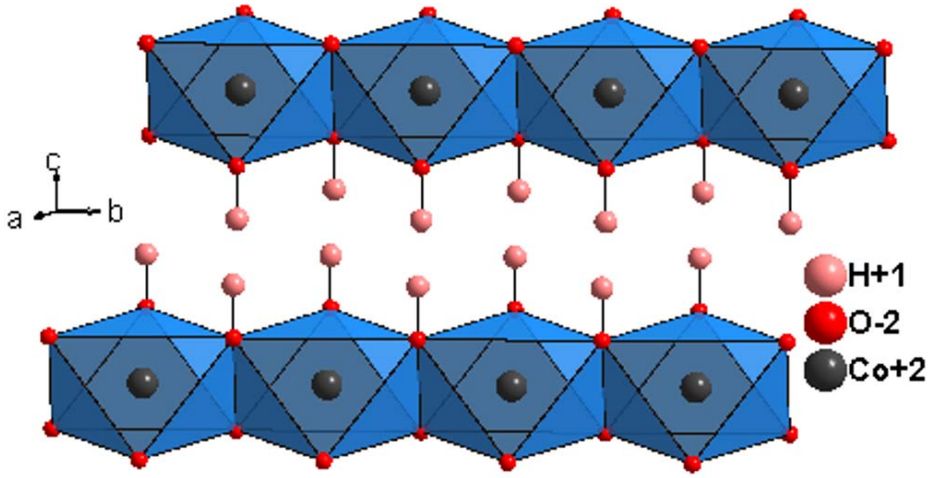

Figure 1.11. Crystal structure of brucite phase which has edge shared octahedra of Co^{2+} ions with hydroxyl oxygens and interlayer H^+ ions.

Most well-known examples of simple layered hydroxides are those of Co and Ni. Nickel forms two kinds of hydroxides, *viz*, α and β-$Ni(OH)_2$. The pure α-$Ni(OH)_2$ is very unstable in water and alkali and quickly transforms to the β-phase which has a brucite structure. The water molecules in the interlayers of α-$Ni(OH)_2$ do not occupy any fixed lattice points making it turbostatic. Doping with Al, Fe, Co etc. can make α-$Ni(OH)_2$ a stable material [122]. Different metal doped α-$Ni(OH)_2$ are found to be active positive electrode materials. Al substituted α-$Ni(OH)_2$ and Al and Co codoped α-$Ni(OH)_2$ are extensively studied electrode materials for their stability and improved applicability [123-125].

Similarly, cobalt hydroxide also is known to crystallize in two polymorphs, α and β-$Co(OH)_2$. The β form is a stoichiometric phase of the composition $Co(OH)_2$ with brucite structure and consists of a hexagonal packing of hydroxyl ions with Co^{2+} occupying alternate rows of octahedral sites, while the α-hydroxides are reported to be isostructural with hydrotalcite-like compounds that consist of positively charged $Co(OH)_{2-x}$ layers which has a connectivity exactly like brucite structure and charge balancing anions (e.g., NO_3^-, CO_3^{2-}, Cl^-, etc.) in the interlayer gallery [121,126]. The α-hydroxides thus have a larger interlayer spacing (usually >7 Å, dependent on intercalated anions) than that of the β-form with an interlayer spacing of 4.6 Å (Figure 1.12) [127].

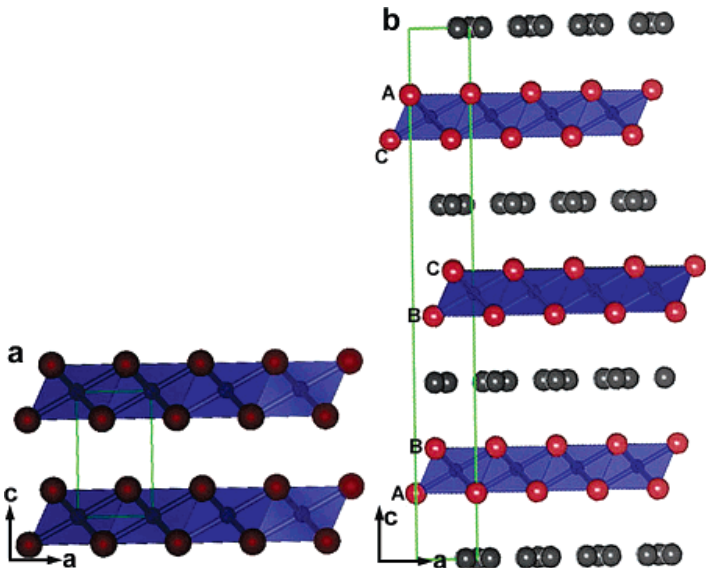

Figure 1.12. Crystal structures of a) β-$Co(OH)_2$and b) α-$Co(OH)_2$ (Reproduced from ref. [126]).

Cobalt hydroxides have recently received increasing attention due to their many important technological applications. β-$Co(OH)_2$ is used as precursors of heterogeneous catalysts for highly textured thermoelectric cobaltite ceramics such as $NaCo_2O_4$ and Ca_xCoO_2, because its hexagonal layered structure has lattice matching with cobaltite materials [128]. β-$Co(OH)_2$/zeolite nanocomposite is an important material as electrochemical super capacitors as it possesses very high capacitance [129]. On the other hand, α-phase compounds are theoretically expected to exhibit superior electrochemical

activity compared to the β-form. In this respect, the α-hydroxides can be more promising electrode materials and their possible ion exchange capability can be utilized in various fields in catalysis [130].

Even if a variety of layered hydroxides are known, photocatalytic properties of these materials are not studied widely. C. G. silva *et al.* firstly reported the high photocatalytic activity of ZnCr-layered double hydroxide (LDH) for O_2 generation [131]. Further, it was found that NiTi-layered double hydroxide and modified ZnCr-layered double hydroxide/graphene are efficient photocatalysts for O_2 evolution [132-134]. However, there are only a few reports about photocatalytic water splitting for H_2 evolution. In 2011, K. Parida and co-workers reported that Zn/Cr LDH and Zn/Cr-CO_3 LDH can produce H_2 from aqueous methanol under visible light irradiation without a cocatalyst. Here the intercalation of carbonate ion enhances hydrogen evolution as it gets oxidised to produce carbonate radical which in turn separates photogenerated holes and electrons efficiently [135].

1.1.4.2. Spatial separation of charge carriers in photocatalysts

Compared to the large number of catalytic site separated photocatalysts reported, only a few compounds which possess suitable band structure as well as spatial separation for photocatalytic water splitting are found in literature [136]. These are anisotropically structured compounds wherein inherent charge separation is possible by spatially separating charge generation sites and electron conducting pathways. In this class of compounds, recombination can be prevented if photogenerated electrons and holes are well separated from each other spatially, i.e. photogeneration sites as well as conduction pathways are physically separated in space within the structure of the semiconductor. Consequently, catalytic activity, which depends on the availability of the photogenerated electrons, can be enhanced if such spatial separation is achieved. For example, Ni doped $InTaO_4$ along with RuO_2 or NiO cocatalyst is a visible light active photocatalyst. $InTaO_4$ consists of TaO_6 edge shared octahedra and Ni^{2+} ions displace In^{3+} from its lattice sites leading to lattice contraction. Intrinsic band gap energy of $InTaO_4$ is 2.6 eV, which will reduce to 2.3 eV after doping with Ni, making it visible light active photocatalyst [137-138].

Another compound of this class is $SnNb_2O_6$, which forms double layers of edge shared NbO_6 octahedra separated by layers of Sn^{2+} ions (Figure 1.13) and can produce hydrogen under visible light with suitable modification with Pt from aqueous methanol solution. Here the photogenerated electrons from the valence band composed of Sn^{2+} are conducted through the edge shared octahedra of NbO_6 and hence spatial separation is achieved [139].

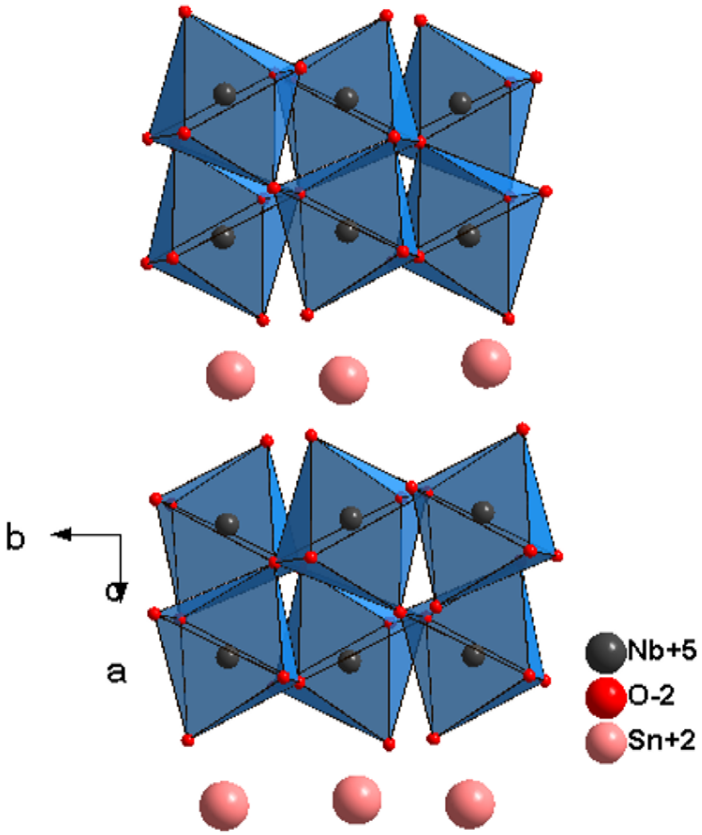

Figure 1.13. Crystal structure of $SnNb_2O_6$, which possesses spatial separation of charge carriers. On irradiation electrons transferred from valence band (composed of Sn^{2+}) are conducted through NbO_6 octahedra.

1.5. Scope and objective of the thesis

From the discussions in the previous sections, it is clear that layered compounds, showing either catalytic site separation or spatial separation through inherent structural characteristics, are more advantageous as photocatalysts. Such structural properties are suggested to minimise recombination and with appropriate band gap engineering and

incorporation of catalytic sites, these compounds can be fine-tuned to give enhanced catalytic activity in solar energy based water splitting. Primary focus of the present work has been to identify novel layered oxides with the right attributes in terms of structure and electronic properties. In 1985, N. Kimizuka *et al.* reported the synthesis and possible structure of a series of compounds of the general formula $AMO_3(BO)_m$ (A ; In, Sc, Yb and Lu, M ; Ga, Al and Fe, B ; Zn, Cu, Mg and Fe and m- integer) [140]. Two decades later, Orita *et al.* had found out that $InGaO_3(ZnO)_1$, the first member of $AMO_3(ZnO)_m$ (where A, M are trivalent metal ions and m – integers) type layered series of compounds, possessed significant spatial separation between charge generating and electron conducting sites. This was attributed to the unique structural properties of the series of compounds [141]. Initial studies in these kinds of systems such as $MgIn_2O_4$, $ZnGa_2O_4$ and $Y_2Sb_2O_7$ were carried out by Kawazoe *et al.* [142-144], and they suggested that layers formed by edge sharing MO_6 octahedra, where M is a p-block metal ion, might act as electron conducting pathways. The enhanced conductivity in these compounds is suggested to be due to a spatial separation of the carrier donors located in insulating layers and conducting layers which transfer the carriers effectively. The spatial separation in $InGaO_3(ZnO)_m$ is found to be much higher compared to normal semiconductors. Interestingly, this is manifested in the anisotropic nature of the electrical conductivity. Measurements on thin films and single crystals reveal higher conductivity along the a–b plane [141].

It is also worthwhile to explore the catalytic site separation and its utility in photocatalysis of layered compounds other than metal oxides. One such family of compounds is layered hydroxides. Prof. D. G. Nocera and his group has explored the oxygen evolution activities of cobalt based cubane systems [145]. It will be interesting to study the incorporation of hydrogen evolution site in a layered hydroxide system with similar structural motifs, where cobalt is in an octahedral coordination with oxygen. If the layered cobalt hydroxide can incorporate cations such as Zn^{2+} and Ni^{2+}, it can be expected to advantageously affect the optical characteristics and contribute to hydrogen production from water. It will be ideal if the spatial separation and catalytic site separation can be achieved within the structure with proper fine tuning of cation incorporation.

Based on these concepts, the following specific works were selected for the present thesis.

1. Synthesis and bulk structural characterization of $InGaO_3(ZnO)_m$ (m-1 to 4) series.
2. The study of the photocatalytic hydrogen evolution activity of bare, NiO loaded and CuO loaded $InGaO_3(ZnO)_m$ (m-1 to 4) under various conditions.
3. Synthesis and bulk structural characterization of $InFeO_3(ZnO)_m$ (m-1 to 4) series.
4. An attempt to understand the photocatalytic hydrogen evolution activity of $InFeO_3(ZnO)_m$ (m-1 to 4) series.
5. Synthesis and characterization of α and β-$Co(OH)_2$ and to study the structural effect of incorporating Zn and Ni.
6. The study of the photocatalytic hydrogen evolution activity of α and β-$Co(OH)_2$ and Zn and Ni incorporated α and β- $Co(OH)_2$.

References

1. Dresselhaus, M. S.; Thomas, I. L. *Nature* **2001**, *414*, 332.
2. Lewis, N. S; Nocera, D. G. *Proc. Natl. Acad. Sci. U. S. A*. **2006**, *103*, 15729.
3. Bockris, J. O'M. *Int. J. Hydrogen Energy* **2002**, *27*, 731.
4. Bard, A. J.; Fox, M. A. *Acc. Chem. Res.* **1995**, *28*, 141.
5. Kawai, T.; Sakata, T. *Nature* **1980,** *286*, 474.
6. Nowotny, J.; Sorrell, C. C.; Sheppard, L. R.; Bak, T. *Int. J. Hydrogen Energy* **2005**, *30*, 521.
7. Chu, S.; Majumdar, A. *Nature* **2012,** *488*, 295.
8. Florin, N.; Harris, A. *Environmentalist* **2007**, *27*, 207.
9. Maeda, K.; Domen, K. *J. Phys. Chem. Lett.* **2010**, 1 (18), 2655.
10. http://solarcellcentral.com/solar_page.htmlAa
11. Lee, J. S. *Catal. Surv. Asia* **2005**, *9*, 217.
12. Abe, R. *Bull. Chem. Soc. Japan* **2011**, *84*, 1000.
13. Maeda, K. *J. Photochem. Photobiol*. C **2011**, *12*, 237.
14. Hao, X. H.; Guo, L. J.; Mao, X.; Zhang, X. M.; Chen, X. J. *Int. J. Hydrogen Energy* **2003**, *28*, 55.
15. Ashokkumar, M. *Int. J. Hydrogen Energy* **1998**, *23*, 427.
16. Fujishima, A.; Rao, T. N.; Tryk, D. A. *J. Photoch. Photobio. C* **2000**, 1, 1.

17. Rufino M. N. Y.; Consuelo lvarez Galvn M.; Del Valle F.; Jos A. V.; JosL. G. F*., Chem. Sus. Chem.* **2009**, *2*, 471
18. Kudo, A. *Catal. Surv. Asia* **2003**, *7*, 1.
19. Tachibana, Y.; Vayssieres, L.; Durrant, J. R. *Nat. Photonics* **2012**, *6*, 511.
20. Fujishima, A.; Honda, K. *Nature* **1972**, *238,* 37.
21. Maeda, K.; Domen, K. *J. Phys. Chem. C* **2007**, *111*, 7851.
22. Kudo, A.; *Int. J. of Hydrogen Energy* **2007**, *32*, 2673.
23. Osterloh, F. E. *Chem. Mater.* **2008**, *20*, 35.
24. Chen, X.; Shen, S.; Guo, L.; Mao, S. S. *Chem. Rev.* **2010**, *110*, 6503.
25. Kudo, A.; Miseki, Y. *Chem. Soc. Rev.* **2009**, *38*, 253.
26. Yuzun F.; Dongmei L. I.; Minghui D.; Yanhong L.; Qingbo M. *Front. Chem. China* **2009**, *4*, 343.
27. Tang, J.; Durrant, J. R.; Klug, D. R. *J. Am. Chem. Soc.* **2008**, *130*, 13885.
28. Walter, M. G.; Warren, E. L.; McKone, J. R.; Boettcher, S. W.; Mi, Q.; Santori, E. A.; Lewis, N. S. *Chem. Rev.* **2010**, *110*, 6446.
29. Seabold, J. A.; Kyoung-Shin, C. *Chem. Mater.* **2011**, *23*, 1105.
30. Ni, M.; Leung, M. K. H.; Leung, D. Y. C.; Sumathy, K. *Renew. Sust. Energ. Reviews* **2007**, *11*, 401.
31. Maitra, U.; Lingampalli, S. R.; Rao, C. N. R. *Curr. Scie. India* **2014**, *106*, 25.
32. Zieliñska, B.; Borowiak-Palen, E.; Kalenczuk, R. J. *Int. J. of Hydrogen Energy* **2008**, *33*, 1797.
33. Schneider, J.; Bahnemann, D. W. *J. Phys. Chem. Lett.* **2013**, *4*, 3479.
34. Teoh, W. Y.; Scott, J. A.; Amal, R.; *J. Phys. Chem. Lett.* **2012**, *3*, 629.
35. Hykaway, N.; Sears, W. M.; Morisaki, H.; Morrison, S. R. *J. Phys. Chem.* **1986**, *90*, 6663.
36. Kayaci, F.; Vempati, S.; Donmez, I.; Biyikliab, N.; Uyar, T. *Nanoscale* **2014**, *6*, 10224.
37. Sabio, E. M.; Chamousis, R. L.; Browning, N. D.; Osterloh, F. E. *J. Phys. Chem. C* **2012**, *116*, 3161.
38. Maeda, K.; Teramura, K.; Lu, D.; Saito, N.; Inoue, Y.; Domen, K.; *Angew. Chemie.* **2006**, *118*, 7970.
39. Dennis Y. C. L.; Xianliang, F.; Cuifang, W.; Meng, N.; Michael, K. H. L.; Xuxu, W.; Xianzhi, F. *Chem. Sus. Chem.* **2010**, *3*, 681.

40. Min, S.; Lu, G. *J. Phys. Chem. C,* **2012**, *116*, 25415.
41. Iwase, A.; Kato, H.; Kudo, A. *Catal. Lett.* **2006**, *108*, 7.
42. Kudo, A. *Int. J. of Hydrogen Energy* **2007**, *32*, 2673.
43. Zhu, J.; Zäch, M. *Curr. Opin. Colloid. In.* **2009**, *14*, 260.
44. Ishii, T.; Kato, H.; Kudo, A. *J. Photochem. Photobiol. A* **2004**, *163*, 181.
45. Kim, H. G.; Hwang, D. W.; Lee, J. S. *J. Am. Chem. Soc*. **2004**, *126*, 8912.
46. Chen, X.; Shen, S.; Guo, L.; Mao, S. S. *Chem. Rev.* **2010**, *110,* 6503.
47. Zhang, J.; Dang, W.; Ao, Z.; Cushing, S. K.; Wu, N. *Phys. Chem. Chem. Phys.* **2015**, *17*, 8994.
48. Asahi, R.; Morikawa, T.; Ohwaki, T.; Aoki, K.; Taga, Y. *Science* **2001,** *293*, 269.
49. Kakuta, N.; Park, K. K.; Finlayson, M. F.; Ueno, A.; Bard, A. J.; Campion, A.; Fox, M. A.; Webber, S. E.; White, J. M. *J. Phys.Chem.* **1985**, *89*, 732.
50. Zhang, M.; Chen, C.; Ma, W.; Zhao, J. *Angew. Chem.* **2008**, *120*, 9876.
51. Tong, Z.; Takagi, S.; Tachibana, H.; Takagi, K.; Inoue, H. *J. Phys. Chem. B* **2005**, *109*, 21612.
52. http://www.rs.kagu.tus.ac.jp/kudolab/naiyou.html
53. Bard, A. J. *J. Photochem.* **1979**, *10*, 59.
54. Maeda, K. *ACS Catal.* **2013**, *3*, 1486.
55. Abe, R.; Sayama, K.; Arakawa, H. *Chem. Phys. Lett*. **2003**, *379*, 230.
56. Yamasita, D.; Takata, T.; Hara, M., Kondo, J. N., Domen, K. *Solid State Ionics* **2004**, *172*, 591.
57. Ishikawa, A.; Yamada, Y.; Takata, T.; Kondo, J. N.; Hara, M.; Kobayashi, H.; Domen, K. *Chem. Mater.* **2003**, *15*, 4442.
58. Fujishima, A.; Honda, K. B. *Chem. Soc. Japan* **1971**, *44*, 1148.
59. Wrighton, M. S.; Ginley, D. S.; Wolczanski, P. T.; Ellis, A. B.; Morse,D. L.; Linz, A. *Proc. Natl. Acad. Sci. U.S.A.* **1975**, *72*, 1518.
60. Schrauzer, G. N.; Guth, T. D. *J. Am. Chem. Soc.* **1977**, *99*, 7189.
61. Van Damme, H.; Hall, W. K. *J. Am. Chem. Soc.* **1979**, *101*, 4373.
62. Kawai, T.; Sakata, T. *Chem. Phys. Lett.* **1980**, *72*, 87.
63. Nozik, A. *J. Appl. Phys. Lett.* **1977**, *30* (11), 567.
64. Sato, S.; White, J. M. *Chem. Phys. Lett.* **1980**, *72*, 83.
65. Kalyanasundaram, K.; Gratzel, M. *Angew. Chem*. **1979**, *18*, 701.

66. Borgarello, E.; Kiwi, J.; Pelizzetti, E.; Visca, M.; Gratzel, M. *Nature* **1981**, *289*, 158.
67. Arakawa, H. *In Photocatalysis Science and Technology*; Kaneko, M., Okura, I., Eds.; Springer: New York, 2002; pp 235–248.
68. Sayama, K.; Arakawa, H. *J. Chem. Soc. Chem. Commun*. **1992**, *2*, 150.
69. Abe, R.; Sayama, K.; Domen, K.; Arakawa, H. *Chem. Phys. Lett*. **2001**, *344*, 339.
70. Liao, C-H.; Huang, C. H., Wu, J. C. S. *Catalysts* **2012**, *2*, 490.
71. Ohno, T.; Mitsui, T.; Matsumura, M. *Chem. Lett.* **2003**, *32*, 364.
72. Sayama, K.; Arakawa, H. *J. Phys. Chem.* **1993**, *97*, 531.
73. Sayama, K.; Arakawa, H. *J. Photochem. Photobiol. A* **1994**, *77*, 243.
74. Kato, H.; Kudo, A. *Chem. Phys. Lett.* **1998**, *295*, 487.
75. Wang, D. F.; Zou, Z. G.; Ye, J. H. *Chem. Mater*. **2005**, *17*, 3255.
76. Hara, M.; Kondo, T.; Komoda, M.; Ikeda, S.; Shinohara, K.; Tanaka, A.; Kondo, J. N.; Domen, K. *Chem. Commun.* **1998**, *3*, 357.
77. Mavroides, J. G.; Kafalas, J. A., Kolesar, D. F. *Appl. Phys. Lett.* **1976**, *28*, 241.
78. Domen, K.; Naito, S.; Onishi, T.; Tamaru, K. *Chem. Phys. Lett.* **1982**, *92*, 433.
79. Sayama, K.; Mukasa, K.; Abe, R.; Abe, Y.; Arakawa, H. *Chem. Commun*. **2001**, *23*, 2416.
80. Kim, H. G.; Becker, O. S.; Jang, J. S.; Ji, S. M.; Borse, P. H.; Lee, J. S. *J. Solid State Chem.* **2006**, *179*, 1214.
81. Kato, H.; Kudo, A. *Catal. Lett.* **1999**, *58*, 153.
82. Kato, H.; Kudo, A. *J. Phys. Chem. B* **2001**, *105*, 4285.
83. Kato, H.; Asakura, K.; Kudo, A. *J. Am. Chem. Soc*. **2003**, *125*, 3082.
84. Mitsui, C.; Nishiguchi, H.; Fukamachi, K.; Ishihara, T.; Takita, Y. *Chem. Lett.* **1999**, *12*, 1327.
85. Hagiwara, H.; Ono, N.; Inoue, T.; Matsumoto, H.; Ishihara, T. *Angew.Chem*. **2006**, *45*, 1420.
86. Lin, W. H.; Cheng, C.; Hu, C. C.; Teng, H. S. *Appl. Phys. Lett*. **2006**, *89*, 211904.
87. Kato, H.; Kudo, A. *Chem. Lett*. **1999**, *11*, 1207.
88. Ikeda, S.; Fubuki, M.; Takahara, Y. K.; Matsumura, M. *Appl. Catal. A* **2006**, *300*, 186.
89. Luan, J. F.; Hao, X. P.; Zheng, S. R.; Luan, G. Y.; Wu, X. S. *J. Mater. Sci.* **2006**, 41, 8001.
90. Wang, D. F.; Zou, Z. G.; Ye, J. H. *Chem. Mater*. **2005**, *17*, 3255.
91. Sato, J.; Saito, N.; Nishiyama, H.; Inoue, Y. *J. Phys. Chem. B* **2003**, *107*, 7965.

92. Wang, D. F.; Zou, Z. G.; Ye, J. H. *Chem. Phys. Lett*. **2004**, *384*, 139.

93. Ikarashi, K.; Sato, J.; Kobayashi, H.; Saito, N.; Nishiyama, H.; Inoue, Y.J. *Phys. Chem. B* **2002**, *106*, 9048.

94. Sato, J.; Saito, N.; Nishiyama, H.; Inoue, Y. J. *Photochem. Photobiol. A* **2002**, *148*, 85.

95. Sato, J.; Saito, N.; Nishiyama, H.; Inoue, Y. *J. Phys. Chem. B* **2001**, *105*, 6061.

96. Sato, J.; Kobayashi, H.; Ikarashi, K.; Saito, N.; Nishiyama, H.; Inoue, Y. *J. Phys. Chem. B* **2004**, *108*, 4369.

97. Abe, R.; Takata, T.; Sugihara, H.; Domen, K. *Chem. Commun.* **2005**, *30*, 3829.

98. Kudo, A.; Steinberg, M.; Bard, A. J.; Campion, A.; Fox, M. A.; Mallouk,. E.; Webber, S. E.; White, J. M. *Catal. Lett.* **1990**, *5*, 61.

99. Shimodaira, Y.; Kato, H.; Kobayashi, H.; Kudo, A. *J. Chem. Soc. Japan* **2007**, *80*, 885.

100. Murray, B.; Kagan, C. R.; Bawendi, M. G. *Annu. Rev. Mater. Sci.* **2000**, *30*, 545.

101. Abe, R.; Higashi, M.; Sayama, K.; Abe, Y.; Sugihara, H. *J. Phys. Chem. B* **2006**, *110*, 2219.

102. Kim, J.; Hwang, D. W.; Kim, H. G.; Bae, S. W.; Lee, J. S.; Li, W.; Oh,S. H. *Top. Catal.* **2005**, *35*, 295.

103. Jeong, H.; Kim, T.; Kim, D.; Kim, K. Int. *J. Hydrogen Energy* **2006**, *31*, 1142.

104. Kim, H. G.; Becker, O. S.; Jang, J. S.; Ji, S. M.; Borse, P. H.; Lee, J. S. *J. Solid State Chem.* **2006**, *179*, 1214.

105. Sayama, K.; Arakawa, H.; Domen, K. *Catal. Today* **1996**, *28*, 175.

106. Kudo, A.; Tanaka, A.; Domen, A.; Mayura, K.; Aika, K.; Onishi,T. *J. Catal.* **1988**, *111*, 67.

107. Yoshioka, K.; Petrykin, V.; Kakihana, M.; Kato, H.; Kudo, A. *J. Catal*. **2005**, *232*, 102.

108. Shimizu, K.; Itoh, S.; Hatamachi, T.; Kodama, T.; Sato, M.; Toda, K. *Chem. Mater.* **2005**, *17*, 5161.

109. Yoshioka, K.; Petrykin, V.; Kakihana, M.; Kato, H.; Kudo, A. *J. Catal.* **2005**, *232*, 102.

110. Otsuka, H.; Kim, K. Y.; Kouzu, A.; Takimoto, I.; Fujimori, H.; Sakata,Y.; Imamura, H.; Matsumoto, T.; Toda, K. *Chem. Lett.* **2005**, *34*, 822.

111. Machida, M.; Yabunaka, J.; Kijima, T. *Chem. Mater.* **2000,** *12*, 812.

112. Domen, K.; Yoshimura, J.; Sekine, T.; Tanaka, A.; Onishi, T. *Catal. Lett.* **1990**, *4*, 339.

113. Ebina, Y.; Sasaki, T.; Harada, M.; Watanabe, M. *Chem. Mater.* **2002**, *14*, 4390.

114. Kim, H. G.; Hwang, D. W.; Lee, J. S. *J. Am. Chem. Soc***. 2004**, *126*, 8912.

115. Kudo, A.; Hijii, S. *Chem. Lett.* **1999**, *10*, 1103.

116. Kudo, A.; Kato, H. *Chem. Lett.* **1997**, *5*, 421.
117. Wang, W.; O'Hare, D. *Chem. Rev.* **2012**, *112*, 4124.
118. Rogez, G.; Massobrio, C.; Rabu, P.; Drillon, M. *Chem. Soc. Rev*. **2011**, *40*, 1031.
119. Chen, H.; Hu, L.; Chen, M.; Yan, Y.; Wu, L. *Adv. Funct. Mater.* **2014**, *24*, 934.
120. Li, P.; Xu, Z. P.; Hampton, M. A.; Vu, D. T.; Huang, L.; Rudolph, V.; Nguyen, A. V. *J. Phys. Chem. C* **2012**, *116*, 10325.
121. Choya, J-H.; Kwona, Y. M.; Hana, K. S.; Songa, S. W.; Chang, S. H. *Mater. Lett.* **1998**, *34*, 356.
122. Xu, X. U.; Zeng, H. C. *Chem. Mater.* **1999**, *11*, 67.
123. Hall, D. S.; Lockwood, D. J.; Bock, C.; MacDougall, B. R. *Proc. R. Soc. A* **2015**, *471*, 20140792.
124. Armstrong, R. D.; Charles, E. A. *J. Power Sources* **1989**, 25, 89.
125. Wu, H. Y.; Xie, Y. L.; Hu, Z. A. *Int. J. Electrochem. Sci.* **2013**, 8, 1839.
126. Liu, Z.; Ma, R.; Osada, M.; Takada, K.; Sasaki, T. *J. Am. Chem. Soc.* **2005**, *127*, 13869.
127. Hu, Z. A.; Xie, Y. L.; Wang, Y. X.; Xie, L. J.; Fu, G. R.; Jin, X. Q.; Zhang, Z. Y.; Yang, Y. Y.; Wu, H. Y. *J. Phys. Chem. C* **2009**, *113*, 12502.
128. Itahara, H.; Seo, W.-S.; Lee, S.; Nozaki, H.; Tani, T.;Koumoto, K. *J. Am. Chem. Soc*. **2005**, *127*, 6367.
129. Cao, L.; Xu, F.; Liang, Y. Y.; Li, H. L. *Adv. Mater.* **2004**, *16*, 1853.
130. Oliva, P.; Leonardi, J.; Laurent, J. F.; Delmas, C.; Braconnier, J. J.; Figlarz, M.; Fievet, F. J. *Power Sources* **1982**, *8*, 229.
131. Silva, C. G.; Bouizi, Y.; Forne´s, V.; Garcı´a, H. *J. Am. Chem. Soc.* **2009**, *131*, 13833.
132. Zhao, Y.; Chen, P.; Zhang, B.; Su, D. S.; Zhang, S.; Tian, L.; Lu, J.; Li, .; Cao, X.; Wang, B.; Wei, M.; Evans, D. G.; Duan, X. *Chem. Eur. J.* **2012**, *18*, 11949.
133. Yao, L.; Wei, D.; Yan, D.; Hu, C. *Chem Asian J.* **2015**, *10,* 630.
134. Roussel, H.; Briois, V.; Elkaim, E.; Roy, A. D.; Besse, J. P.; Jolivet, J. P. *Chem. Mater.* **2001**, *13*, 329.
135. Parida, K.; Mohapatra, L. *Dalton Trans.* **2012**, *41,* 1173.
136. Orita, M.; Tanji, H.; Mizuno, M.; Adachi, H.; Tanaka, I. *Phys. Rev. B* **2000**, *61*, 1811.
137. Zou, Z. G.; Arakawa, H. J. *Photochem. Photobiol. A* **2003**, *158*, 145.
138. Zou, Z. G.; Ye, J. H.; Sayama, K.; Arakawa, H. *Nature* **2001**, *414*, 625.

139. Hosogi, Y.; Tanabe, K.; Kato, H.; Kobayashi, H.; Kudo, A. *Chem. Lett*. **2004**, *33*, 28.
140. Kimizuka, N.; Mohri, T. *J. Solid State Chemistry* **1985,** *60*, 382.
141. Orita, M.; Tanji, H.; Mizuno, M.; Adachi, H.; Tanaka, I. *Phys. Rev. B* **2000**, *61*, 1811.
142. Un'no, H.; Hikuma, N.; Omata, T.; Ueda, N.; Hashimoto, T.; Kawazoe, H. *Japan. J. Appl. Phys.* **1993**, *32*, L1260.
143. Omata, T.; Ueda, N.; Ueda, K.; Kawazoe, H. *Appl. Phys. Lett.* **1994**, *64*, 1077.
144. Yanagawa, K.; Ohki, Y.; Omata, T.; Hosono, H.; Ueda, N.; Kawazoe, H. *Appl. Phys. Lett.* **1994**, *64*, 2071.
145. Symes, M. D.; Lutterman, D. A.; Teets, T. S.; Anderson, B. L.; Breen, J. J.; Nocera, D. G. *ChemSusChem* **2013**, *6*, 65.

Chapter 2

Exploration of coordination geometries of Ga and Zn in $InGaO_3(ZnO)_m$ (m = 1–4) and studies on their photocatalytic H_2 evolution activity: Making $InGaO_3(ZnO)_m$ (m = 1–4) into visible light active

2. 1. Introduction

Semiconductor oxides are widely used in the area of photocatalysis due to their unique electronic structures facilitating the formation of electron-hole pairs on irradiation with light of appropriate energy, which can be utilized in electron transfer processes. Electrons and holes which are generated in the bulk of the semiconductor particles travel to the surface, eventually getting utilized in the reduction and oxidation reactions of water, respectively, in case of water splitting [1-3]. During these processes, there are many possible pathways for recombination of the electron hole pair leading to a wastage of energy, most common being grain boundaries, lattice defects as well as surface sites, which can be addressed by improving the sample characteristics [4]. However, another important parameter depends on the structural characteristics of the valence and conduction bands. The photogenerated electrons and holes are generally located in conduction and valence bands, respectively, and in most of the semiconductors with bulk 3D structures, they are structurally close to each other enhancing the chances of recombination [5]. Hence, structures with inherent separation of the photogenerated charges spatially, will be ideally placed for efficient photocatalysis. Spatial separation aims at the separation of carrier generation and carrier movement spatially in a lattice [6]. In this context, $InGaO_3(ZnO)_m$ series of compounds are found to be highly advantageous with much higher spatial separation compared to other contemporary semiconductors [7]. Most of the current information on the structural aspects of this interesting family of compounds is derived from single crystal XRD studies [8-10]. The structure is complicated with slabs of InO_6 octahedra separated by blocks of Ga/ZnO_n polyhedra [11-13]. Interestingly, the layered structure is manifested in the anisotropic nature of the electrical conductivity [14]. Measurements on thin films and single crystals reveal higher conductivity along the a-b plane [6]. Kawazoe and co-workers suggested that layers formed by edge sharing MO_6 octahedra, where M is a trivalent metal ion, may act as electron conducting pathways away from charge generating Ga/ZnO_n layers, facilitating anisotropic electrical conductivity [15-16]. The conduction band in this series of compounds consists of In 5s states which delocalize in the InO_2 layer. Valence band is composed of O 2p and Zn 3d partial bands [6].

Here the spatial separation of photogenerated charge carriers is possible due to the exact separation of the charge generation site and conducting pathways.

The extent of anisotropy and hence spatial separation clearly depends on the connectivity of InO_6 slabs and Ga/ZnO blocks as well as their local structures. However, theoretical studies and electron microscopy studies are sometimes contradictory in explaining the geometries of Ga and Zn, especially across the series. At this juncture, it is worthwhile to get further insights into the structure of the series, focusing on Zn and Ga coordination geometries. Moreover, most of the reported studies of this series are on thin films or single crystal and it may be advantageous to throw more light upon bulk structure in powder form. Since device fabrication is easier with powder samples, such information will be more representative of materials which can be used in practical applications.

The work described in this chapter focuses on understanding the complex structure of the series of compounds in powder form in terms of variations due to increase in ZnO layers. The work extends to exploiting the spatial separation and utilizing these materials for photocatalytic water splitting activity with and without sensitizers as well as cocatalysts. Accordingly, this chapter is divided into two sections; (i) dealing with the synthesis and structural studies in powder form using sophisticated techniques like solid state NMR (Nuclear Magnetic Resonance) spectroscopy as well as EXAFS (Extended X-ray Absorption Fine Structure) and (ii) photocatalytic activity studies in water splitting using CuO sensitizer as well as NiO cocatalyst. A structure-property correlation is also attempted in explaining the catalytic activity.

2.2. Structural studies

2.2.1. Experimental section

2.2.1a. Synthesis of $InGaO_3(ZnO)_m$ (m = 1– 4)

The $InGaO_3(ZnO)_m$ (m = 1– 4) series was synthesized by a solid state reaction at 1350 °C using component individual oxides. In_2O_3 (Sigma Aldrich, 99.99%), Ga_2O_3 (Sigma Aldrich, 99.99%) and ZnO (Sigma Aldrich, 99.99%) in appropriate ratios were mixed in an agate mortar. The mixture was ground well with acetone and heated to 700, 900, and 1000 °C for

12 h in step. The powder samples were mixed with 5% polyvinyl alcohol (PVA) in water which acts as a binder and finally pressed into pellets. The pellets were heated to 1350 °C for 12 h twice with intermittent grinding. The resulting sintered pellets are found to be dense.

2.2.1b. Characterization

The principles of all the techniques used throughout the work are briefly discussed in the Appendix 1. Powder X-ray diffraction (PXRD) of all the samples was carried out in a PANalytical X'pert Pro dual goniometer diffractometer working under 40 kV and 30 mA at room temperature. The radiation used was Cu Kα (1.5418 Å) with a Ni filter and the data collection was carried out using a flat holder in Bragg–Brentano geometry with a 1° slit at the source sides. An X'celerator solid-state detector with a step size of 0.008° and time per step 43.18 s was employed. Structural characterization as well as quantitative phase analysis by Rietveld refinement method using GSAS EXPGUI software were also done.

^{71}Ga magic angle spinning (MAS) solid-state NMR spectra were recorded on a Bruker AV 600 spectrometer equipped with a superconducting magnet of 14.1 Tesla. The samples were packed in a 1.3 mm zirconia rotor and were spun at a speed of 60 kHz in a 1.3 mm Bruker MAS probe which was tuned to 183.02 MHz, which is the ^{71}Ga larmour frequency. A single pulse with a width of 0.29 μs was used to obtain quantitative spectra. Due to the low sensitivity of the ^{71}Ga nucleus, 163 840 scans were collected with a recycle delay of 0.5 s between the scans. A $Ga(NO_3)_3$ solution was used as the spectral reference. All the data were collected at room temperature.

EXAFS measurements were done to probe the local structure surrounding the Zn and Ga. Measurements were carried out at the dispersive EXAFS beamline (BL-8) in the transmission mode at the INDUS-2 Synchrotron Source (2.5 GeV, 100 mA) at the Raja Ramanna Centre for Advanced Technology (RRCAT), Indore, India. The set of EXAFS data analysis programmes available within the IFEFFIT software package have been used for the EXAFS data analysis. This includes background reduction and Fourier transform to derive the χ(R) versus R spectra from the absorption spectra (using ATHENA sub routine), the generation of the theoretical EXAFS spectra starting from an assumed crystallographic

structure and finally the fitting of the experimental data with the theoretical spectra using the ARTEMIS subroutine.

2.2.2. Results and discussion

Figure 2.1 shows the PXRD patterns of $InGaO_3(ZnO)_m$ (m = 1, 2, 3 and 4, referred hitherto as IGZ1 to 4) . The patterns match those of the reported compounds corresponding to JCPDS nos. 38-1104, 40-0252, 40-0253 and 40-0254 respectively. The series of compounds in which m is odd are reported to crystallize in a rhombohedral phase with space group *R-3m* and those where m is even crystallize in a hexagonal phase with space group $P6_3/mmc$ [17-18]. It is known that bulk preparations of these compounds contain negligible amounts of the (m − 1) phase [19]. We also observed peaks of the (m − 1) series in the PXRD patterns of the samples sintered at 1350 °C. Attempts at heating for longer durations and at higher temperatures led to an increase in the (m − 1) phases. Hence, the phases heated at 1350 °C were considered the best in the bulk preparations with the least amount of impurities and were selected for further studies.

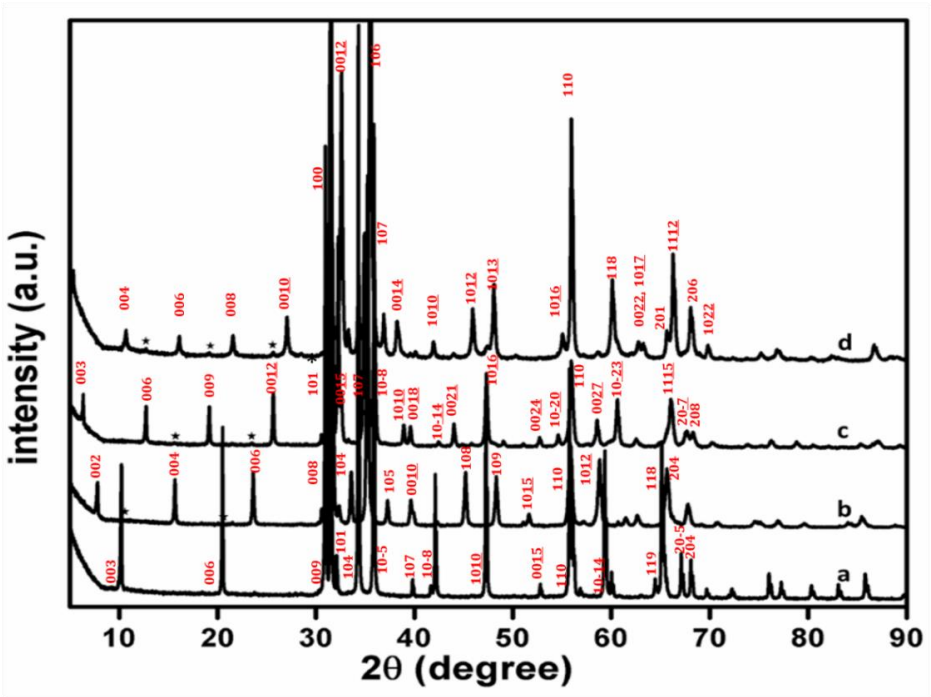

Figure 2.1. PXRD patterns of $InGaO_3(ZnO)_m$ [(a) m = 1, (b) 2, (c) 3 and (d) 4]. Peaks corresponding to impurity phases of (m − 1) compounds are indicated by *. hkl planes are indicated against the peaks.

In order to quantify the impurity phase a quantitative phase analysis was carried out by Rietveld refinement method using GSAS-EXPGUI software [20]. Table 2.1 indicates the presence of (m-1) impurity phases in these compounds in trace quantities. It was also observed that as ZnO amount increases, fraction of this (m-1) phase increases, as a structural consequence of introduction of ZnO layer.

Table 2.1. Impurity phase fractions of (m - 1) components in $InGaO_3(ZnO)_m$ (m = 1 - 4).

Compound	Impurity phase (m - 1) Weight fraction%
1	-
2	0.99
3	3.2
4	5.5

The refinement proceeded more or less smoothly with reasonable refinement parameters. Initially, cell parameters were refined with a few background terms and in a stepwise manner, atomic positions, occupancies and isothermal parameters were included. After that, profile functions were refined. Again cell parameters, atomic parameters and isothermal parameters were refined with increasing background terms. The structural and refinement parameters are tabulated in Table 2.2. The Rietveld refinement plots are given in Figure 2.2.

Polyhedral representations of the refined structures obtained, focusing on Zn and Ga geometries, are displayed in Figure 2.3. In IGZ1, 100% of both Zn and Ga are present in a TBP geometry. In IGZ3, only 33.3% Zn occupies TBP and 66.6% occupies tetrahedral geometry. In IGZ2 and 4, however, 100% Zn exists in tetrahedral and 100% Ga occupies TBP geometry.

The compounds with even and odd number of ZnO layers have different kinds of structures. The first member is isostructural with $YbFe_2O_4$ [21-22]. Most of the reports are

based on this compound. According to single crystal studies the structure of IGZ1consists of two layers of edge sharing Zn/GaO_5 trigonal bipyramids (TBP) sandwiched between single

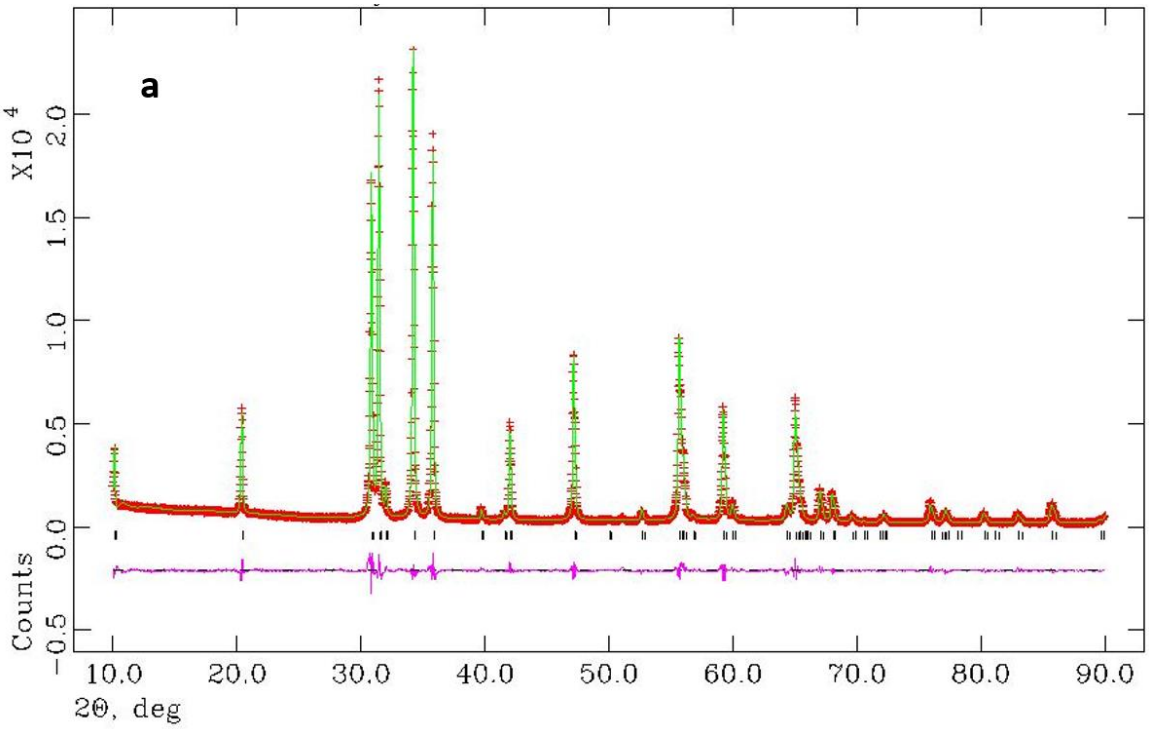

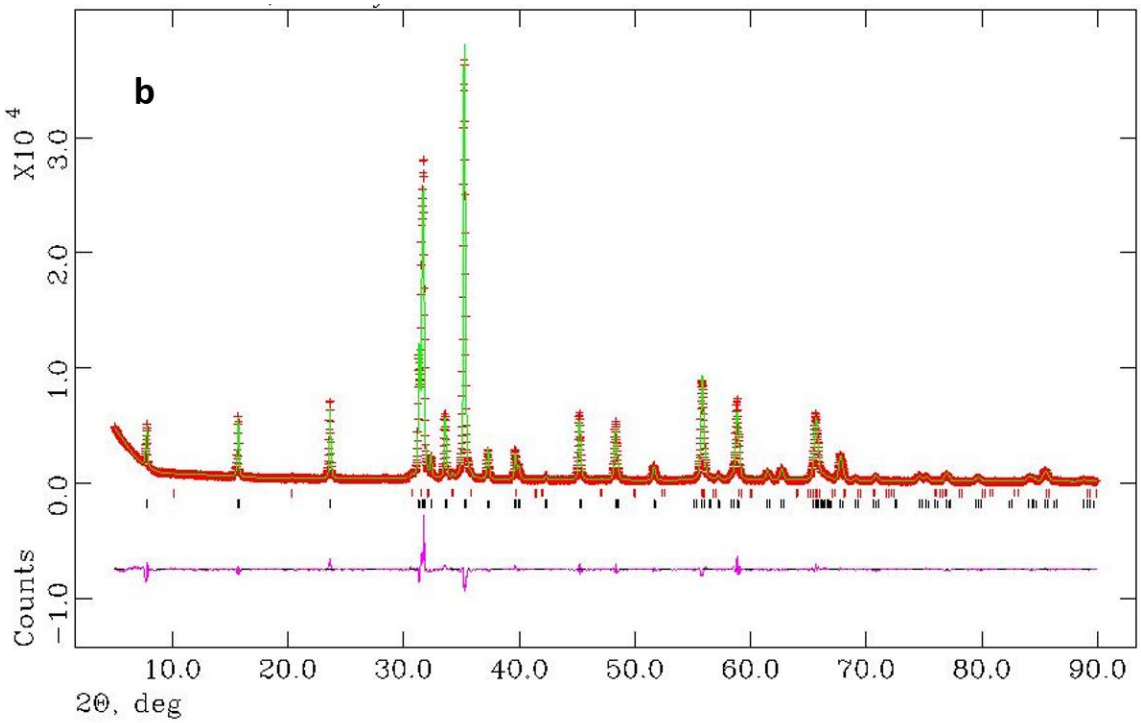

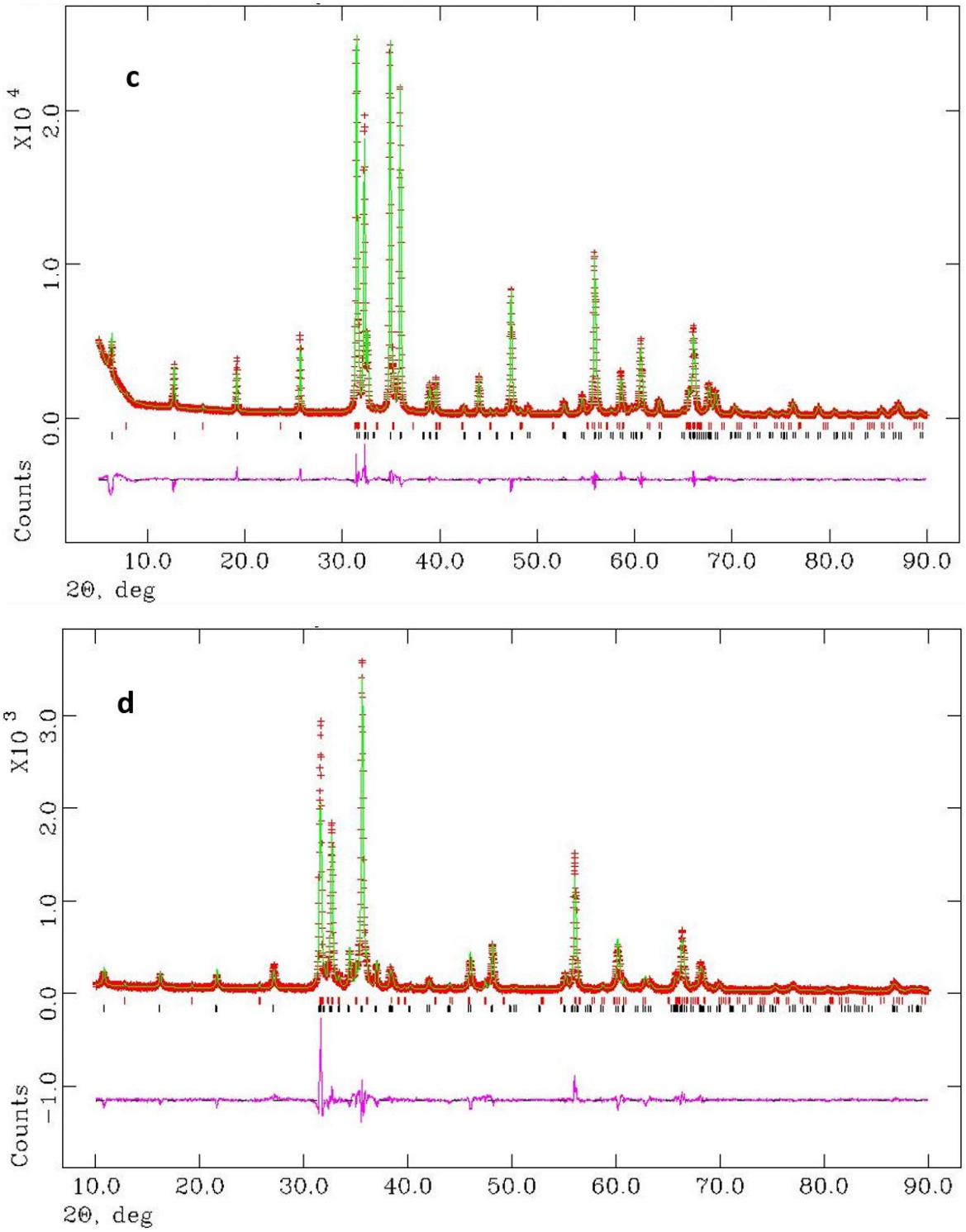

Figure 2.2. Rietveld refinement of the PXRD pattern of (a) IGZ1, (b) IGZ2, (c) IGZ3 and (d) IGZ4. Red line represents experimental data, green line is the Rietveld fit and pink line represents difference plot. Vertical lines (black) expected positions for the main phase. Vertical lines (red) expected positions for the impurity phase.

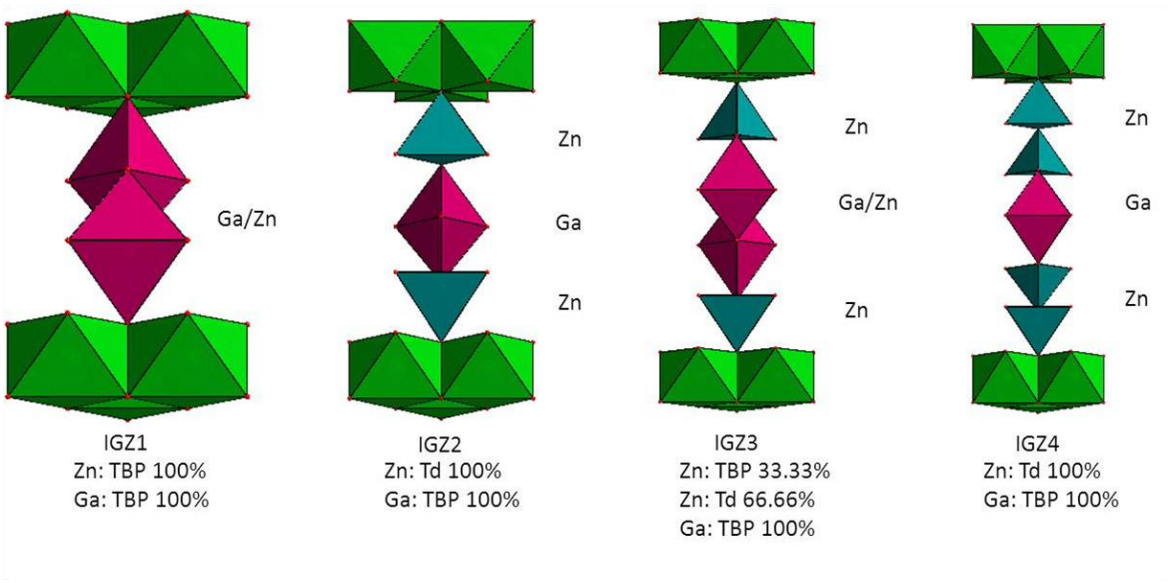

Figure 2.3. Polyhedral representations of IGZ1 to IGZ4 based on PXRD refinement parameters. In m = odd series, Ga and Zn are randomly placed in TBP, whereas in m = even series, Zn and Ga occupy exclusively tetrahedra and TBP respectively.

layers of edge sharing InO_6 octahedra. The connectivity between these two layers is through corner sharing of apical oxygens of TBPs and octahedral corner oxygen atoms. The TBPs are reported to be of type-I, with the cations closer to the basal plane and having a regular shape [9]. IGZ3 also has same kind of structure, except that the extra ZnO assumes a tetrahedral geometry which connects the Zn/GaO TBP layers and the InO_6 octahedral layers through corner sharing [23]. However, in IGZ2 and IGZ4, the Ga TBPs share corners with layers consisting exclusively of ZnO_4 tetrahedra, which are again corner shared with InO_6 octahedral layers [10-11]. These studies indicate that Zn and Ga are in TBP geometry for m = odd series. Zn and Ga have exclusively TBP and tetrahedra respectively in an m = even series. In the IGZ3 compound, Zn also exists in a tetrahedral geometry in addition to TBP (Figure 2.3). Some recent theoretical and microscopic studies have proposed alternate structures for IGZ1 and IGZ3, whereby Ga retains the TBP geometry but Zn assumes a tetrahedral geometry [10]. But in bulk powder it is very difficult to achieve the complete solution as the currently used techniques like PXRD, microscopic methods etc. cannot differentiate Zn and Ga and hence, local variations cannot be identified. Hence the system was studied by techniques which give more information about the Zn and Ga local environments separately.

Table 2.2. Refinement and structural parameters of $InGaO_3(ZnO)_m$ (m = 1 - 4).

Parameters		IGZ1	IGZ2	IGZ3	IGZ4
χ 2		3.318	5.326	5.598	3.402
wRp (%)		6.32	7.39	7.57	17.22
Rp (%)		4.68	5.68	5.555	13.23
a (Å)		3.2940(0)	3.2899(0)	3.2851(0)	3.2868(0)
c (Å)		26.0102(2)	22.5318(3)	41.5549(4)	32.9593(8)
Ga	x	0	0	0	0.6667
	y	0	0	0	0.3333
	z	0.2167	0.25	0.1353	0.2500
U_{iso}		0.00867	0.0202	0.0146	0.0250
Zn1	x	0	0.6667	0	0.6667
	y	0	0.3333	0	0.3333
	z	0.2169	0.3641	0.7399	0.0914
U_{iso}		0.0177	0.0158	0.0177	0.0154
O1	x	0	0.6667	0	0.6667
	y	0	0.3333	0	0.3333
	z	0.12712	0.4500	0.3063	0.0381
U_{iso}		0.01651	0.0236	0.0236	0.0250
O2	x	0	0	0	0
	y	0	0	0	0
	z	0.2911	0.3437	0.0837	0.1106
U_{iso}		0.02023	0.0118	0.0061	0.0250
O3	x		0.6667	0	0.6667
	y		0.3333	0	0.3333
	z		0.2500	0.8082	0.1786
U_{iso}			0.0051	0.0208	0.0250

In (0,0,0) for all the four compounds and U_{iso} in IGZ1 is 0.0178, IGZ2 is 0.0216, IGZ3 is 0.01823 and IGZ4 is 0.0301; O4 in IGZ4 (0,0,0.25) and U_{iso} is 0.0250; Zn2 in IGZ3 (0,0,0.1354) and U_{iso} is 0.019429 and in IGZ4 (0,0,0.1702) and U_{iso} is 0.01383

In order to understand local structure environment of Ga, ^{71}Ga MAS NMR studies were carried out. It is a powerful tool to understand the local environments of magnetically active nuclei. Here three geometries can be expected for gallium *viz* octahedral, trigonal bipyamidal and tetrahedral. β-Ga_2O_3 was selected as the reference as it contains Ga both in octahedral and tetrahedral coordinations [24]. NMR spectrum of β-Ga_2O_3 shows two peaks at 201 ppm and 41 ppm corresponding to tetrahedral and octahedral coordinations respectively as shown in the Figure 2.4.

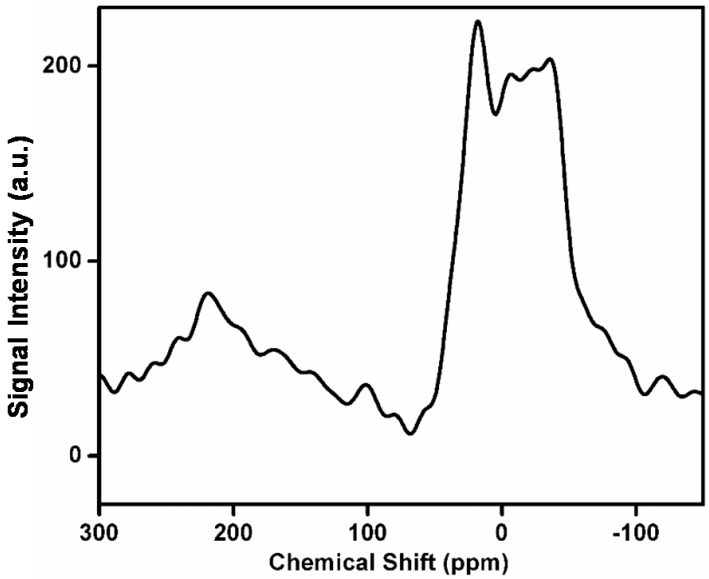

Figure 2.4. ^{71}Ga Solid state NMR spectrum of β-Ga_2O_3 shows two distinct signals for tetrahedral coordination at 220 ppm and octahedral coordination at 41 ppm.

The Figure 2.5 indicates the ^{71}Ga MAS NMR of the series of compounds. The spectra showed broad features ranging from 0 to 200 ppm. This indicates the presence of multiple coordination sites. The compounds IGZ1, IGZ2 and IGZ3 have a peak which comes in between the octahedral and tetrahedral geometry. It is possible to assume that the peak corresponding to trigonal bipyramidal or any pentacoordinated geometry will have a value between those of octahedral and tetrahedral coordinations. It is possible to identify and quantify various coordination geometries by deconvoluting the broad peaks and DMFIT program was used for this [25]. The NMR parameters were iterated by the DMFIT program to obtain a very good fit with the experimental spectra. The extend of occupancy of each coordination was obtained from the area under the curve. The details of all the parameters

obtained from the deconvolution are tabulated in the Table 2.3. From the table it is clear that all the four compounds have substantial amount of Ga in octahedral environment. The peak corresponding to octahedral environment is situated in between 20 and 70 ppm. IGZ1 has gallium in highest occupancy of octahedral environment at 21%. The rest of the compounds have an average of 10% Ga occupying octahedral coordination. This can be substantiated in accordance with the observations made in In_2O_3–Ga_2O_3 solid solutions. It is known that in In_2O_3–Ga_2O_3 solid solutions, Ga dissolves into the In–O network [26]. Such a phenomenon cannot be ruled out with Ga partly exchanging with In octahedral sites within the InO_2 layers. The observation that the concentration of Ga in octahedral sites is more in IGZ1 when compared to the rest of the compounds may point to a proximity of Ga and In in this compound.

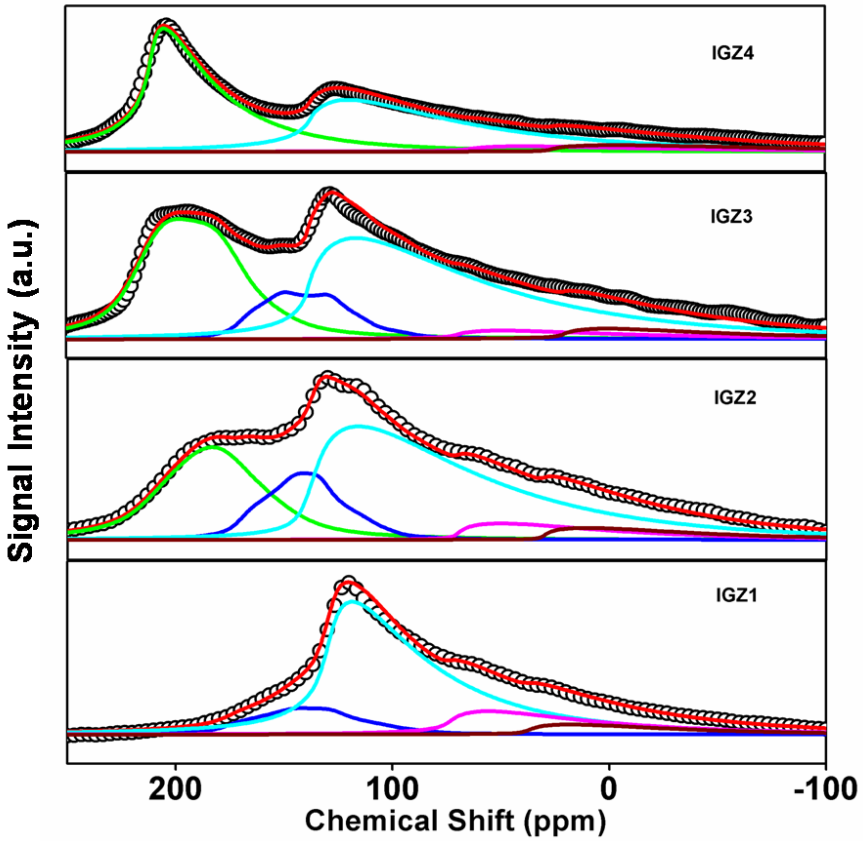

Figure 2.5. Fitted ^{71}Ga MAS NMR spectra of compounds $InGaO_3(ZnO)_m$, (m = 1– 4); black hollow circles: experimental spectra, red line: fitted curve, green line: tetracoordinated gallium, blue line: intermediate phase, cyan line: pentacoordinated gallium, pink line and brown lines: octahedral gallium respectively.

Table 2.3. The NMR fitting parameters for $InGaO_3(ZnO)_m$ (m = 1, 2, 3 and 4).

Compounds	Geometry	Model (DMFIT)	Position (ppm)	Chemical Shift (ppm)	C_Q (KHz)	%
IGZ1	Td	-	-	-	-	-
	Intermediate	Q mas 1/2	176.86	-	6950.12	11.56
	TBP	CzSimple	128.52	6.00	6500.00	67.89
	Oct 1	CzSimple	75.94	4.00	8025.36	15.97
	Oct 2	CzSimple	35.94	4.00	8211.66	4.58
IGZ2	Td	Q mas 1/2	214.58	-	6084.53	26.41
	Intermediate	Q mas ½	171.56	-	6058.06	13.83
	TBP	CzSimple	139.00	8.00	9000.00	49.41
	Oct 1	CzSimple	69.00	3.00	8181.86	5.90
	Oct 2	CzSimple	29.35	3.00	8314.07	4.45
IGZ3	Td	Q mas ½	223.00	-	6350.00	32.75
	Intermediate	Q mas ½	173.80	-	6599.58	11.07
	TBP	CzSimple	139.00	1.00	8900.00	48.20
	Oct 1	CzSimple	70.76	3.00	8653.14	3.78
	Oct 2	CzSimple	21.42	3.00	8403.67	4.21
IGZ4	Td	CzSimple	211.00	5.00	5120.06	48.86
	Intermediate	-	-	-	-	-
	TBP	CzSimple	137.81	2.00	8009.21	38.94
	Oct 1	CzSimple	69.00	1.00	8983.16	6.56
	Oct 2	CzSimple	24.00	2.00	8405.60	5.64

It is clear from the NMR spectra that the concentrations of Ga vary in different geometries. The exact fraction of occupancy in different coordination geometries is indicated in Table 2.4. The spectra of IGZ1 has a peak at 128.8 ppm which corresponds to a pentacoordination. This has a marginal occupancy of 68%. It is also observed that there is no peak corresponding to tetrahedral coordination which usually situated around 200 ppm. It can be inferred that IGZ1has Ga in a pentacoordination, which is in accordance with the single crystal studies. In IGZ2, Ga is present in both tetrahedral and pentacoordination. A peak at 214.58 ppm (26.41%) indicates gallium in tetrahedral coordination. This tetrahedral Ga exists along with 49.41% of pentacoordinated Ga. It is observed that there is a 10 ppm increase in the chemical shift of the peak corresponding to pentacoordinated Ga. In NMR, as the number of coordinating ligands attached to the magnetically active nucleus decreases, it experiences more deshielding. This leads to an increase in the chemical shift. Hence, it is commonly accepted that an increase in the chemical shift indicates a coordination sphere with a lower number of effective oxygens.

In IGZ3, the fraction of tetrahedral gallium slightly increases to 32.75%. But the concentration of pentacoordinated Ga fraction is still comparable with IGZ2 (48.2%). Here also an increase in chemical shift of 10 ppm is observed for tetrahedral position. Again this indicates a possible coordination sphere with an effectively lower number of oxygens. In the case of IGZ4, 49% of the Ga exists in Td geometry whereas the concentration in TBP geometry is now reduced to 39%. However, the chemical shifts are 137 and 211 ppm for penta and tetracoordinated respectively. This points to the presence of more effective oxygens within the coordination sphere when compared to IGZ3. These results show an increase in tetrahedral coordination as we go from m = 1 to 4 in the series with drastic enhancements occurring in IGZ1–2 and IGZ3–4 transitions. Moreover, Ga in IGZ3 is shown to coordinate with the least number of ligand oxygen atoms with the highest chemical shifts for both penta and tetracoordinations (Table 2.4).

Table 2.4. NMR peak positions and area under the peaks of IGZ1 to IGZ4 in percentage.

Compound	Peak Position	Percentage
IGZ1	35.9 (oct 2) 75.9 (oct 1)	20.5
	128.5 (penta)	68
	176.8 (inter)	11.5
	~200 (td)	0
IGZ2	29.4 (oct 2) 69 (oct 1)	10.3
	139 (penta)	49.4
	171.6 (inter)	13.8
	214.6 (td)	26.4
IGZ3	21.4 (oct 1) 70.7 (oct 2)	7.9
	139 (penta)	48.2
	173.8 (inter)	11
	223	32.7
IGZ4	24.00 (octa 1) 69.00 (octa 2)	12.2
	137.8 (penta)	39
	~ 170 (inter)	0
	211	49

Oct: octahedral, penta: penta coordinated, inter: intermediate, td: tetrahedral. Percentages of the two octahedral geometries are combined for clarity.

Even though the percentage of tetracoordinated geometry is high in IGZ4, effective oxygen atoms may be more due to the decrease in the chemical shifts. This is in contradiction to the observation from the crystal studies whereby Ga is proposed to be present in TBP coordination exclusively in all the four compounds. This is in contradiction to the observation from the crystal studies whereby Ga is proposed to be present in TBP coordination exclusively in all the four compounds. It is noteworthy here that a peak at ~170 ppm can be seen in IGZ1–3 which points to a small percentage (~11%) of an intermediate geometry between tetra and pentacoordinations. This peak is absent in IGZ4, indicating a complete transition to tetracoordinated. To further understand these systems, Zn coordination details were studied using X-ray absorption technique, EXAFS.

EXAFS measurements were done to explore the Zn coordination and to compare the results obtained for Ga environment through ^{71}Ga MAS NMR in IGZ1 to IGZ4. Figure 2.6 shows the normalized EXAFS spectra for Zn and Ga K-edge for the $InGaO_3(ZnO)_m$ (m=1, 2, 3, 4) samples. Fitted Fourier transformed EXAFS spectra for Zn and Ga K-edge in R space are displayed in Figure 2.7 and Figure 2.8 respectively. The set of EXAFS data available within IFEFFIT software package have been used for data analysis. This includes background reduction and Fourier transform to derive the $\chi(R)$ versus R spectra from the absorption spectra (using ATHENA software), generation of the theoretical EXAFS spectra starting from an assumed crystallographic structure and finally fitting of experimental data with the theoretical spectra using ARTEMIS software. The theoretical fit is represented by a solid line overlaid on the experimental data. The bond distances, co-ordination numbers (including scattering amplitudes) and disorder (Debye-Waller) factors (σ^2), which give the mean square fluctuations in the distances, have been used as fitting parameters. The best fit results are summarized in Table 2.5 for Zn edge measurements which gives the local structure information surrounding the Zn sites and Table 2.6 for Ga edge measurements which gives the local structure information surrounding the Ga sites.

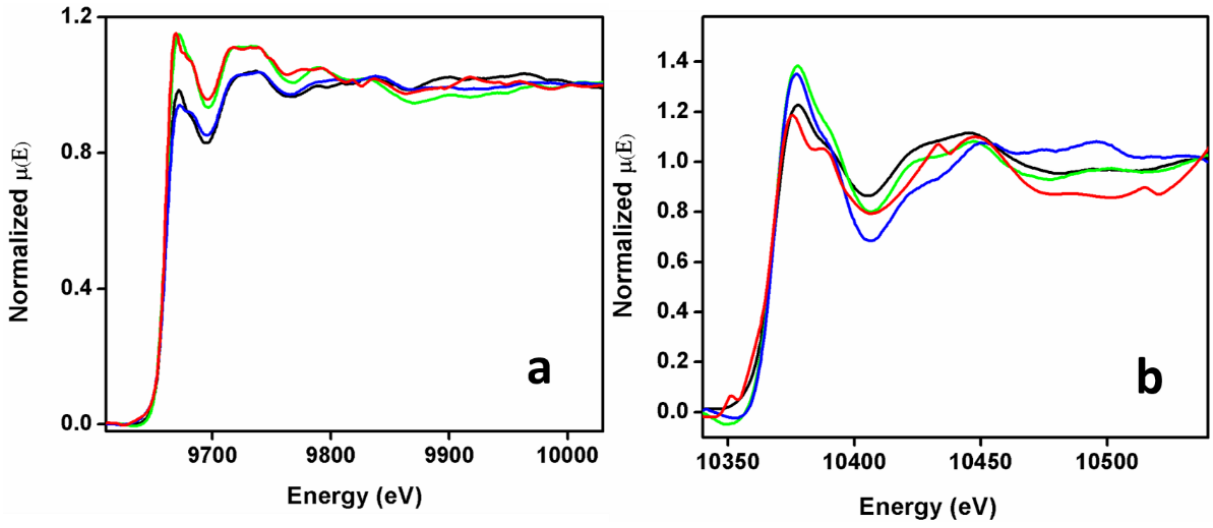

Figure 2.6. Normalized EXAFS spectra of $InGaO_3(ZnO)_m$ (m=1 - 4 a) at Zn K-edge and b) at Ga K-edge.

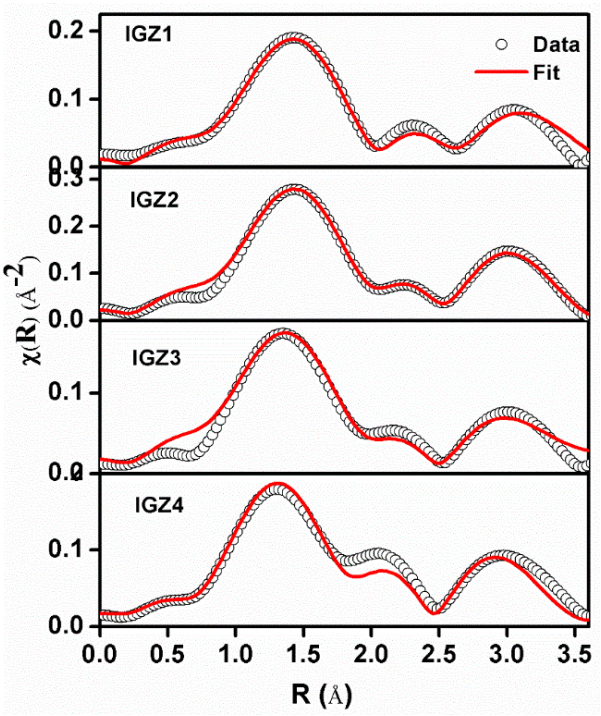

Figure 2.7. Fitted Fourier transformed EXAFS spectra of IGZ1 to IGZ4 at Zn K-edge (scatter points) and theoretical fit (solid line).

Table 2.5. Local structural parameters for IGZ1 to IGZ4 evaluated by EXAFS measurements at Zn K-edge.

Paths	Parameters	IGZ1	IGZ2	IGZ3	IGZ4
Zn-O	R (Å)	1.91	1.91	1.89	1.91
	N	3	3.78	2.85	3.0
	σ^2	0.006	0.006	0.006	0.007
Zn-O	R (Å)	2.34	2.38	2.24	2.21
	N	2	0.91	1.37	0.96
	σ^2	0.009	0.005	0.01	0.003
Zn-Ga	R (Å)	3.11 (Zn-Zn/Ga)	3.18	3.07	3.09
	N	3.17	3	3	3
	σ^2	0.003	0.009	0.008	0.003
Zn-Zn	R (Å)	3.29	3.18	3.24	3.26
	N	6	4.48	6	6
	σ^2	0.006	0.009	0.009	0.006
Zn-In	R (Å)	3.44	3.52	3.65	4.11
	N	2.68	2.21	2.4	3
	σ^2	0.009	0.008	0.01	0.015

The first peak in fitted Fourier transformed spectra (Figure 2.7) of Zn K-edge EXAFS is due to oxygen atoms surrounding the central Zn atom. In IGZ1, Zn atom is surrounded by five oxygen atoms, three at a distance of 1.91 Å and two at 2.34 Å. This can be considered as a coordination geometry of perfect TBP with three planar bonds and two apical bonds. Based on the crystallographic studies, the distance between the Zn in the tetrahedral layer and O of the GaO_5 polyhedra would be much longer than this, indicating the possibility of Ga existing in highly distorted geometries shortening the distance between the layers. It is

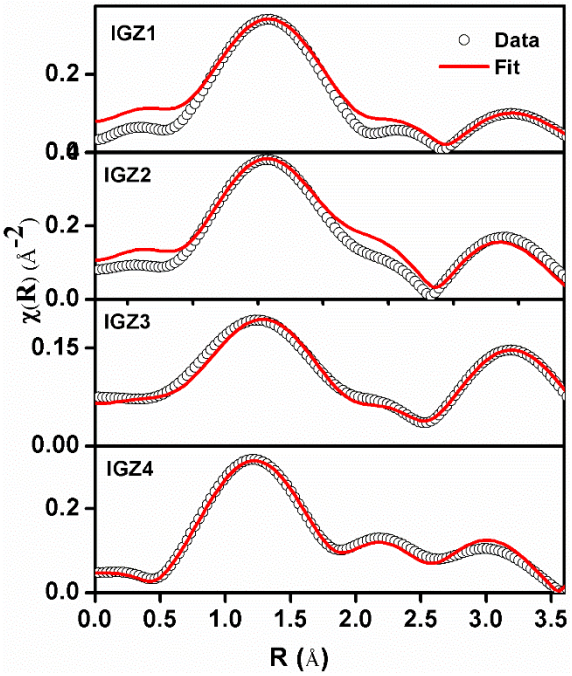

Figure 2.8. Fitted Fourier transformed EXAFS spectra of IGZ1 to IGZ4 at Ga K-edge (scatter points) and theoretical fit (solid line).

also shown by Nomura *et al*. that 4 Zn(Ga) and 5 Ga(Zn) atoms of bond lengths greater than 3 Å construct the second shell around the central Zn(Ga) atom. Here the second peak is fitted between 2.5-3.5 Å of the versus R spectra as shown in Figure. 2.7 for IGZ1, which is found to be due to the 3rd, 4th and 5th shells surrounding the Zn atom at a distance of 3.11 Å, 3.29 Å and 3.44 Å respectively. Though the 4th and 5th shell could be identified as due to Zn and In atoms respectively with coordination numbers of ~ 6 and 3, the 3rd shell could be due to either Ga or Zn atoms which could not be unambiguously identified due to the facts that Ga and Zn are randomly distributed in the bi-pyramidal $GaZnO_2$ block and Ga and

Zn are isoelectronic in nature. For the Ga edge measurements also, as shown in Figure 2.8, the peak between 2.5-3.7 Å of the χ versus R spectra was fitted and it is found to be a mixed shell of Ga and Zn at ~3.2 Å and an In shell at ~3.47 Å. The Zn-Zn, Zn-In, Ga-Ga and Ga-In bond lengths and coordination numbers as shown in Table 2.5 and Table 2.6 are in good agreement with that reported by Nomura *et al*. on single crystalline $InGaZnO_4$ films prepared by reactive solid state epitaxy.

Table 2.6. Local structural parameters for IGZ1 to IGZ4 evaluated by EXAFS measurements at Ga K-edge.

Paths	Parameters	IGZ1	IGZ2	IGZ3	IGZ4
Ga-O	R (Å)	1.86	1.85	1.84	1.85
	N	3.2	3.3	3.28	3.27
	σ^2	0.002	0.002	0.012	0.002
Ga-O	R (Å)	2.23	2.24	2.14	2.20
	N	1.85	0.94	0.8	1.42
	σ^2	0.002	0.002	0.002	0.002
Ga-Zn	R (Å)		3.01	3.02	3.18
	N		6	3	6
	σ^2		0.008	0.005	0.003
Ga-Ga	R (Å)	3.19 (Ga-Ga/Zn)	3.18	3.20	3.28
	N	7.20	6	9	5.7
	σ^2	0.017	0.003	0.009	0.002
Ga-In	R (Å)	3.47			
	N	2.27			
	σ^2	0.009			
Ga-O	R (Å)		3.88	4.16	4.05
	N		3	8.04	11.1
	σ^2		0.002	0.003	0.001
Ga-O	R (Å)		4.02	4.19	4.44
	N		12	3	12
	σ^2		0.003	0.006	0.002

In IGZ2, first peak in Figure 2.7 is due to the oxygen shells around the Zn, with four oxygen atoms at 1.91 Å and one oxygen atom at 2.38 Å. Similarly the Ga atom is surrounded by 3 oxygen atoms with Ga-O bond length 1.85 Å and one oxygen atom at 2.24 Å making it more inclined to tetracoordination. Referring to Table 2.5, it is clear that in IGZ3, the central Zn atom is surrounded by ~4 oxygen atoms with 2.85 oxygen atoms at a bond length of 1.89 Å and 1.37 oxygen atoms at a distance of 2.24 Å. This geometry can be considered more as a trigonal base plane with an elongated axial bond. It can be assumed that this originated from a highly distorted trigonal bipyramidal geometry with one axial bond too elongated. The total number of oxygen atoms surrounding central Zn is now 4.22 which indicates a tetracoordination. The Ga atom is surrounded by ~4 (4.43) oxygen atoms with three oxygen atoms at a distance of 1.84 Å and one oxygen atom at distance of 2.14 Å. In IGZ4, Zn has three oxygen atoms at a distance of 1.91 Å and one at 2.21 Å with the total oxygen atoms being 3.96. There seems to be a gradient in the total number of oxygen atoms bonded to Zn across the series. From this data, we can clearly see that there is a random mixing of Zn and Ga sites in the layer sandwiched between the In–O layers and both have similar coordination geometries. This is even more evident from the Zn–Ga distances, which are ~3 Å, corresponding to the distance between any two adjacent polyhedra. Again while comparing the Zn/In coordination across the series, there is a slight increase in the coordination number which indicates some kind of stretching of the sandwich layer. The Ga–In coordination sphere exists only in the case of IGZ1, which shows that the Ga presence is restricted to the inner layers of the sandwich and any possible random mixing of Ga and Zn sites occurs in these layers. This may also give credence to the ^{71}Ga MAS NMR observation that more Ga occupies octahedral coordination in IGZ1. As in the case of Ga, there is a clear but gradual shift from TBP to tetracoordinated geometry. This is also evident from the appearance of a pre-edge peak in the Ga K-edge EXAFS spectra (Figure 2.9) for IGZ4, which is a typical characteristic of tetrahedral coordination [27-29].

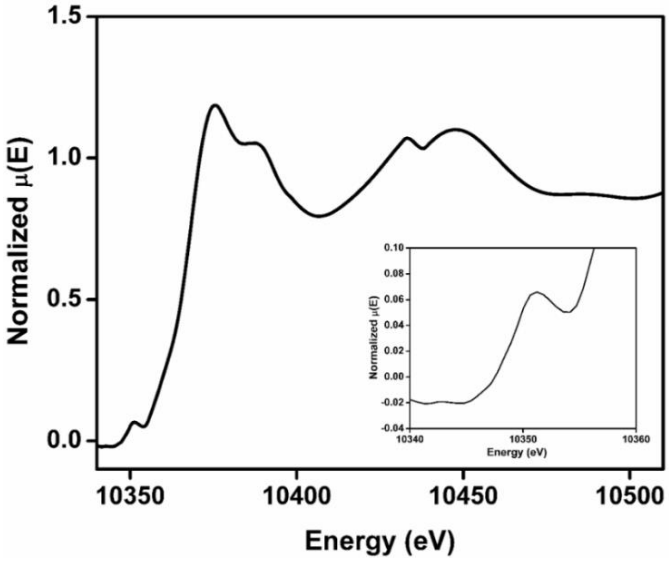

Figure 2.9. Pre-edge peak in the Ga K-edge EXAFS spectra for IGZ4.

The bonding characteristics point towards distorted polyhedra with basal bonds of distances of ~1.85 Å but with highly elongated axial bonds, effectively reducing the coordination number to four (Table 2.6). A gradual transition from pentacoordinated and an intermediate geometry to tetracoordinated geometries could be observed across the series for both Ga and Zn.

2.3. Photocatalytic activity studies on bare, CuO and NiO loaded IGZ1-4

2.3.1. Experimental

2.3.1a. Synthesis of NiO and CuO loaded IGZ1-4

IGZ1-4 series of oxides were synthesized by the method discussed in section 2.2.1. The series of compounds were loaded with CuO and NiO for studying the effect of loading on photocatalytic hydrogen generation. Various amounts (1 wt%, 2 wt%, 4 wt% and 10 wt%) of CuO and NiO were loaded on IGZ series by wet impregnation followed by calcination [30]. Typically, appropriate amounts of copper (II) nitrate trihydrate (Merck, 99%) was weighed and dissolved in minimum amount of deionized water. The solution was then mixed thoroughly with the parent IGZ compound and dried in an oven. The mixture was then calcined at 350 °C in air for 5 h. Similarly NiO was also loaded using nickel(II) nitrate hexahydrate (Sigma Aldrich,) by wet impregnation followed by

calcination at 370 °C in air for 1 h followed by calcination at 500 °C in hydrogen for 2 h and finally at 200 °C under air for 1 h.

2.3.1b. Characterization

Powder X-ray diffraction (XRD) of all the samples was carried out in a PANalytical X'pert Pro dual goniometer diffractometer as described in section 2.2.1b. The diffuse reflectance UV–visible spectra were recorded on a Cary series UV–vis–NIR spectrometer, in the wavelength range of 200–800 nm. Powder samples were firmly packed into the sample holder and baseline correction is done with Teflon pellet. Reflections of the sample with respect to varying wavelengths were recorded and the values were plotted as Kubelka-Munk (K M) function against wavelength. The tangent plotted to the x intercept is taken as the band gap. The specific surface areas of the samples were determined from N_2 adsorption by the B.E.T. method using NOVA 1200 Quanta Chrome equipment.

2.3.1c. Catalytic Testing

The catalysts were studied for their photocatalytic activity by reactions that were carried out in a gas-closed system of 70 mL capacity. The photocatalyst powder (30 mg) was dispersed in aqueous methanol solution (25 mL) by a magnetic stirrer in an irradiation cell made of quartz. Typically, 20 mL of pure water and 5 mL of methanol were employed as reactant solutions for water splitting. Here methanol was taken as sacrificial reagent that gets oxidized by the resulting photogenerated holes. The light source was high and low pressure 400 W Hg lamp for UV and visible irradiation. The amount of H_2 evolved was determined using gas chromatography (Agilent 7890 GC with Carbosphere column and N_2 as carrier gas) with thermal conductivity detector. The program used in GC for all the analysis involved the detector temperature of 200 °C and oven temperature of 80 °C at the time of injection. The reactions were repeated using $NaNO_2$ filter to rule out the presence of UV irradiation. The photograph and scheme of the reactor set up is shown in Figure 2.10 and Figure 2.11 respectively. The same setup and reaction conditions are used for the work presented in all the chapters.

Figure 2.10. Reactor set up for photocatalytic water splitting which consists of a quartz cell having 70 ml capacity and it is gas closed by means of rubber septum. The light sources are inside the quartz jackets where cold water circulates continuously.

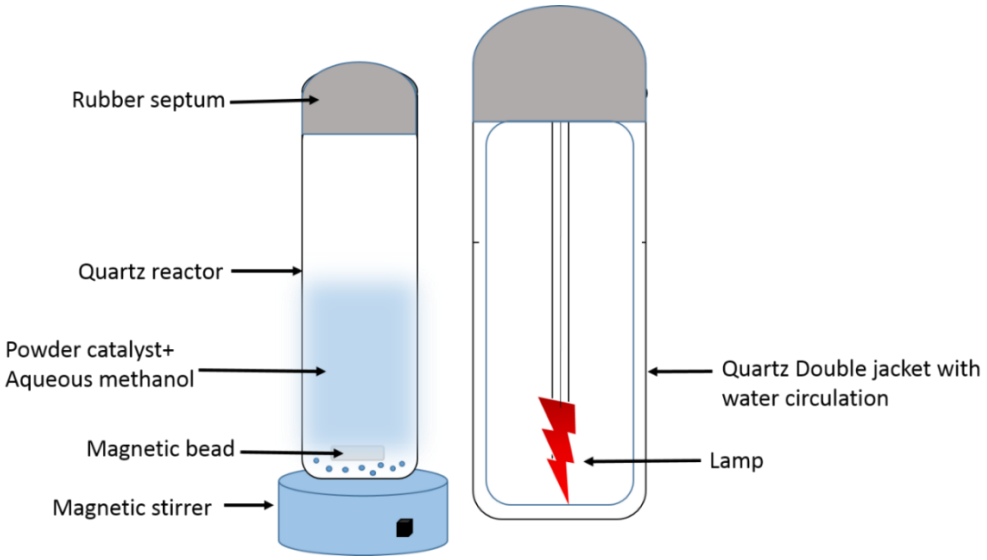

Figure 2.11. Scheme of the reactor set up**.**

2.3.2. Results and Discussion

The PXRD patterns of 2 wt% CuO and NiO loaded compounds are given in Figure 2.12. It is observed that there are no characteristic peaks corresponding to nickel and copper oxides due to fine dispersion of quantum sized particles.

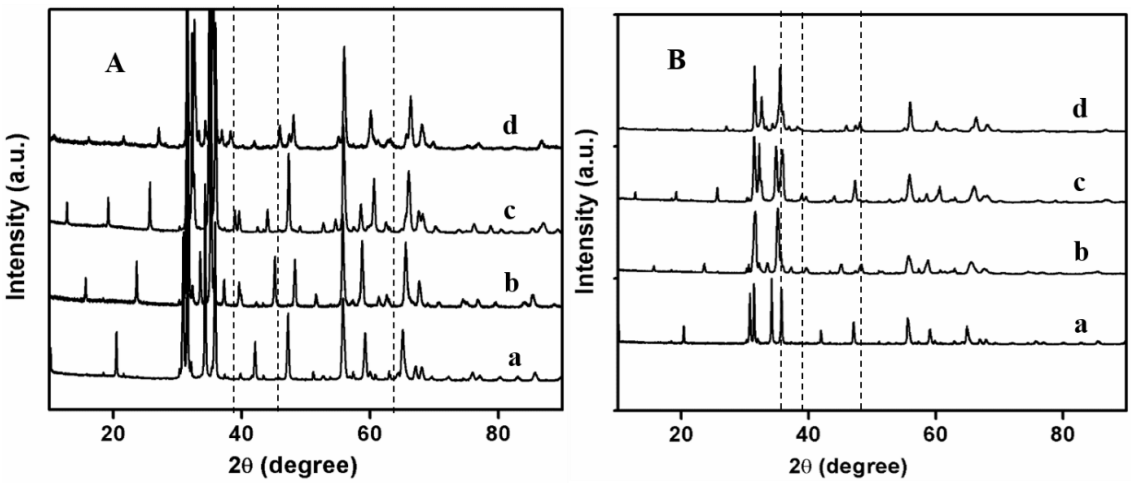

Figure 2.12. PXRD patterns of (A) 2 wt% NiO and (B) 2 wt% CuO loaded (a) IGZ1, (b) IGZ2, (c) IGZ3 and (d) IGZ4. The dotted lines indicate the expected peak positions of NiO in (A) and CuO in (B).

The surface areas of bare, 2 wt% NiO loaded and 2 wt% CuO loaded IGZ1 – 4 are tabulated in Table 2.7. The values are very low for any meaningful comparison which is expected since the compounds are synthesized at very high temperatures. However, low surface area is not a deterrent for photocatalytic activity, if accompanied by high crystallinity, since this can minimize grain boundaries and other recombination sites within the bulk.

Table 2.7. BET surface area of bare, 2 wt% NiO and 2 wt% CuO loaded IGZ1 to IGZ4

Compound (bare)	Surface area (m^2/g)	Compound (2 wt% NiO)	Surface area (m^2/g)	Compound (2 wt% CuO)	Surface area (m^2/g)
IGZ1	1.804	IGZ1	2.891	IGZ1	2.461
IGZ2	2.69	IGZ2	3.170	IGZ2	4.861
IGZ3	7.899	IGZ3	3.505	IGZ3	2.880
IGZ4	7.783	IGZ4	2.475	IGZ4	2.352

UV–vis absorbance spectra of IGZ1-4 show UV light absorption. A relation of reflectance to Kubelka–Munk factor, $F(R) = (1- R)^2/2R$ [31], was used to calculate the band gap energies. The Kubelka–Munk model forms the basis for measurements of the band gap of bulk powder samples through the construction of Tauc plot, specifically, a plot of

$(F(R)h\nu)^{1/2}$ versus $h\nu$. The band gap energies are estimated in this way to be 3.7, 3.6, 3.9, and 4.0 eV for m = 1−4 compounds, respectively (Figure 2.13). The band gap energies of all compounds correspond to UV range in the solar spectrum. Using the experimentally obtained band gap energy, an attempt was made to calculate flat band potentials based on Mulliken electronegativity [32]. The details of the calculations are given in appendix 2.1. This method has been routinely used in calculating band characteristics of simple oxides. Even though structural contributions are not taken into consideration, this method is suggested to give a good understanding even in complex oxides. The band positions can be calculated using the equation,

$$E_{vfb} = EA - E_{ref} + (1/2\ E_g) \qquad (2.1)$$

where EA is the electron affinity of the individual atoms. It can be obtained from the geometrical mean of the electronegativity of the each element. The electronegativity was taken on the basis of Mulliken's calculations. E_{ref} is the energy of free electrons on the hydrogen scale. The band positions thus obtained are represented in relation with standard hydrogen electrode in Figure 2.14.

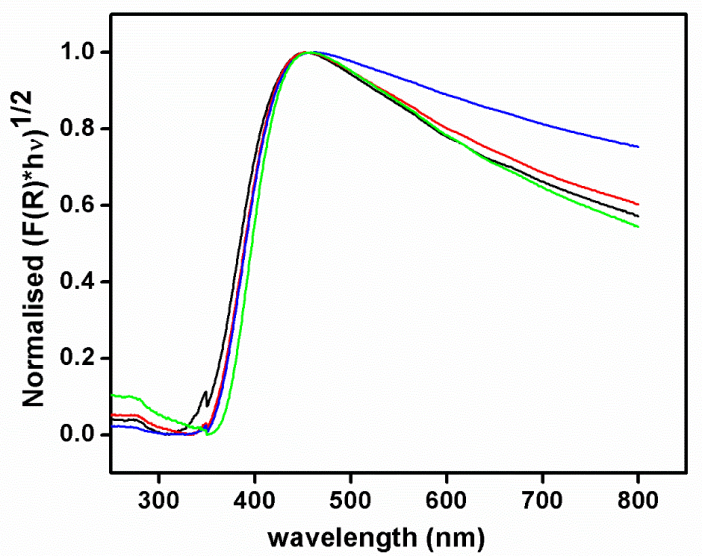

Figure 2.13. UV - visible diffused reflectance spectra of IGZ1 to IGZ4, (black) IGZ1, (red) IGZ2, (blue) IGZ3, and (green) IGZ4.

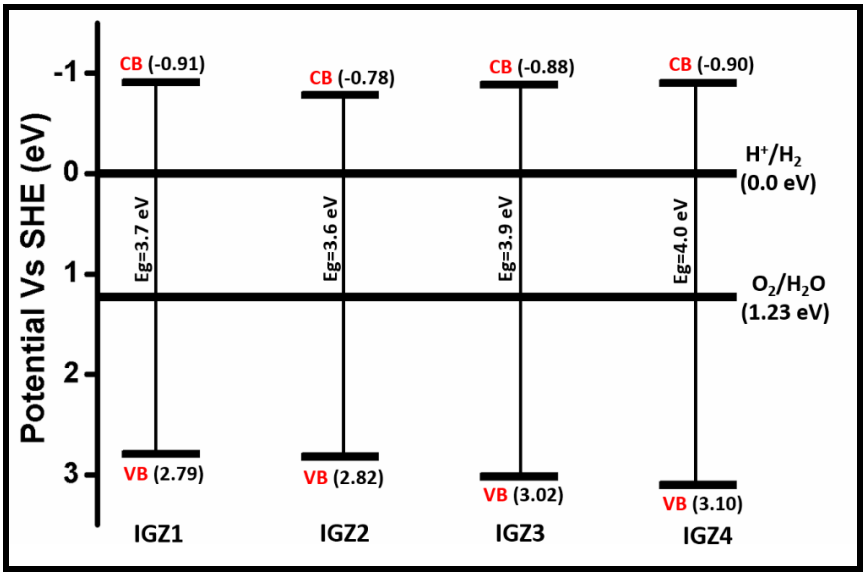

Figure 2.14. Valence band and conduction band positions of $InGaO_3(ZnO)_m$ (m = 1–4).

This was validated by Impedance spectroscopy also. For this, a representative sample of IGZ1 was chosen and impedance was calculated using aqueous solution of 7×10^{-4} M $K_3[Fe(CN)_6]$ in 1 M KCl as the electrolyte. Using the impedance value obtained, capacitance was calculated correlating it to flat band potential employing Mott-Schottky plot [33] (details are given in appendix 2.2). The value obtained, viz., -0.82 eV is highly comparable to that obtained from Mulliken electronegativities (Figure 2.15).

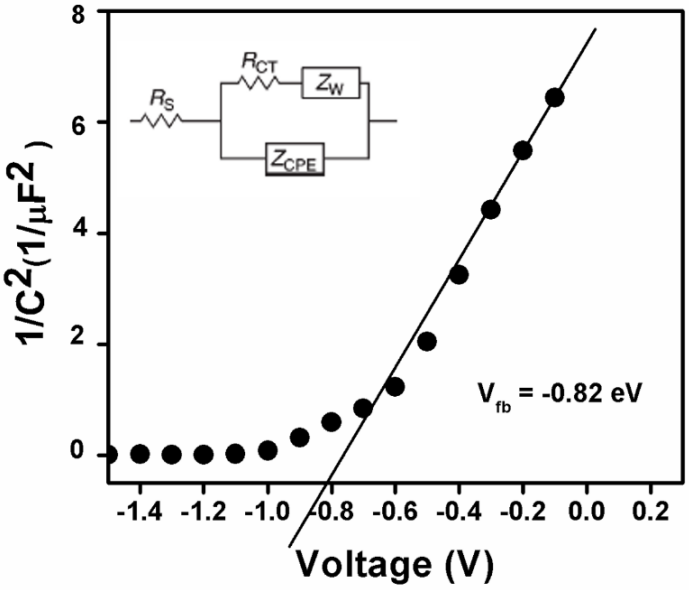

Figure 2.15. Mott-Schottky plot for IGZ1 in 7×10^{-4} M $K_3Fe(CN)_6]$ in 1 M KCl. The Randles circuit used is also shown.

Since the conduction bands of these compounds lie at a higher potential than H^+/H_2O reduction potential, an electron transfer facilitating the reduction can be envisaged. Bare IGZ compounds were evaluated for their activity for hydrogen generation from water–methanol mixtures under UV light irradiation (Figure 2.16). The catalysts displayed reasonable activity resulting in H_2 evolution of ~ 5 mmol/g.

Here two drawbacks could be anticipated (i) poor catalytic activity of IGZ surface sites and (ii) large band gap affecting visible light activity. These problems can be addressed by using a proper electron acceptor or cocatalyst and a suitable sensitizer respectively.

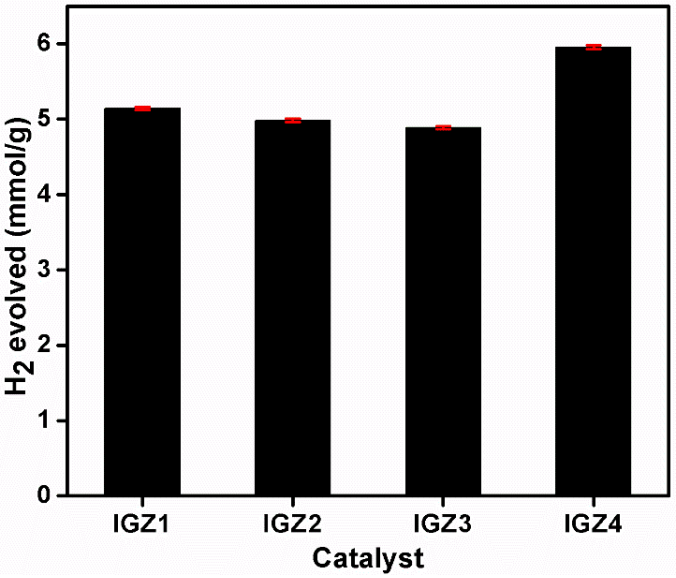

Figure 2.16. H_2 evolution of IGZ 1 to 4 from 20 v/v% methanol–water mixtures under UV irradiation for 4 h.

It is clear from Figure 2.14 that the conduction bands of IGZ compounds are situated at a much more negative potential (-0.78 to -0.9 eV) compared to H^+/H_2 reduction potential (0 eV) which affects the kinetics of electron transfer to the electrolyte detrimentally. So it is advisable to incorporate a good electron acceptor with appropriately placed band positions mediating electron transfer from IGZ conduction bands to the electrolyte, more or less acting like an electron shuttle.

NiO is a wide band gap semiconductor with band gap of 3.6 eV shifting its absorption to high energy UV region. This is also evident from the lack of any absorption

features in the visible region in UV-vis spectra of the NiO loaded catalysts (Figure 2.17). However, it is known to provide catalytically active sites on semiconductors of appropriate band structures [34-35]. Band positions of NiO, computed based on Mulliken's electronegativity (Figure 2.18), locates its conduction band at -0.54 eV which is ~0.3 eV positive to CB of IGZ and ~0.54 eV negative to the reduction potential of H^+/H_2. Hence it can be hypothesized that NiO will aid in an effective electron transfer from IGZ compounds to the electrolyte enhancing photocatalytic activity in UV region. However, on loading 2 wt% NiO, the activity of the IGZ compounds in UV irradiation was found to enhance by two-fold (Figure 2.19). This can be due to the appropriate conduction band placement of the photocatalysts and NiO with respect to the redox potential of water as explained earlier. The conduction band edge of NiO is found to be closer to the reduction potential of H^+/H_2O compared to the parent photocatalysts. In the presence of NiO, the photogenerated electron from the parent photocatalysts migrate to conduction band of NiO which facilitates the hydrogen evolution by acting as catalytic site. However, all the four compounds are inert under visible irradiation for photocatalytic water splitting activity confirming that photoexcitation occurs in IGZ compounds.

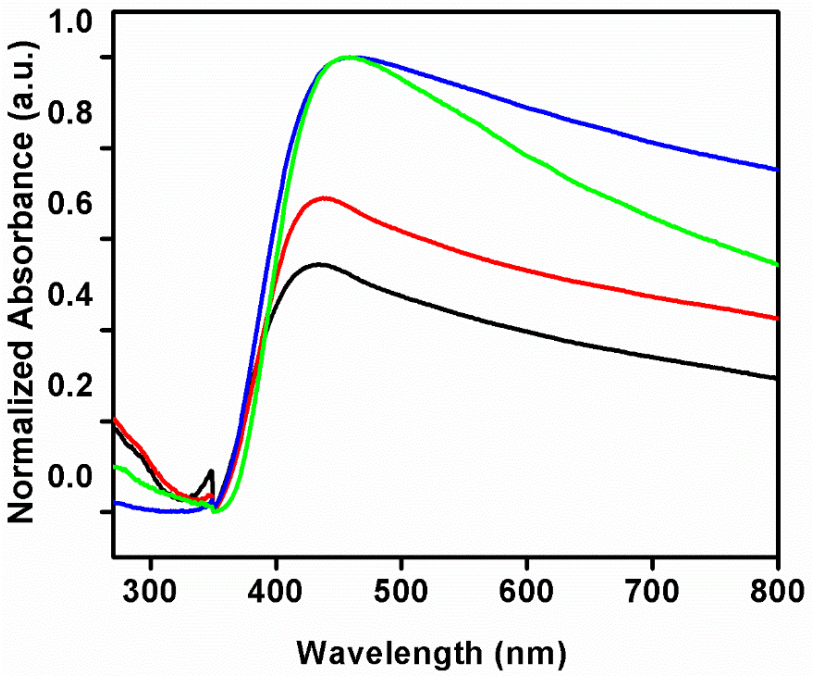

Figure 2.17. Diffused reflectance spectra of 2 wt% NiO impregnated (black) IGZ1, (red) IGZ2, (blue) IGZ3, (green) IGZ4.

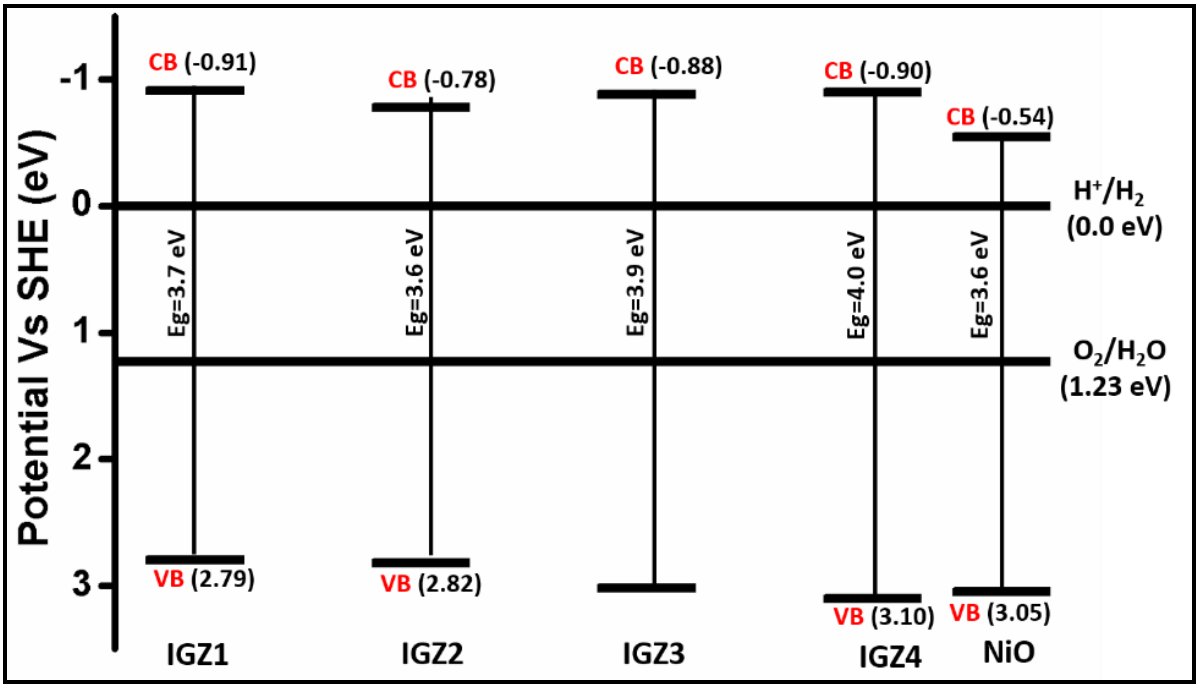

Figure 2.18. Valence band and conduction band positions of IGZ1 to IGZ4 and NiO.

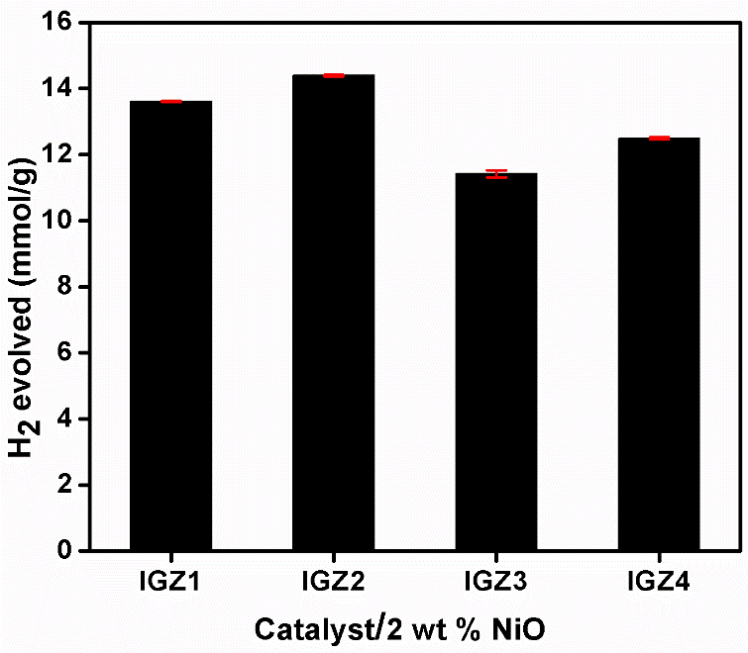

Figure 2.19. H_2 evolution of 2 wt% NiO loaded IGZ 1 to 4 from 20 v/v% methanol–water mixtures under UV irradiation for 4 h.

As mentioned earlier, employing sensitizers is one way of achieving visible light absorption and subsequent photocatalytic activity in visible light. CuO has been reported to facilitate visible light absorption due to its narrow band gap [36]. CuO is a p-type

semiconductor with a bulk direct band gap of 3.25 ± 0.05 eV. It also possesses a fundamental band gap of indirect nature and various reports estimate it to be in the range of 1.2 – 1.9 eV which is relevant to visible light absorption. Even though this allows excitation of electrons from valence band to conduction band under visible light irradiation, it also eases recombination of the excitons resulting in low catalytic activity of CuO [37].

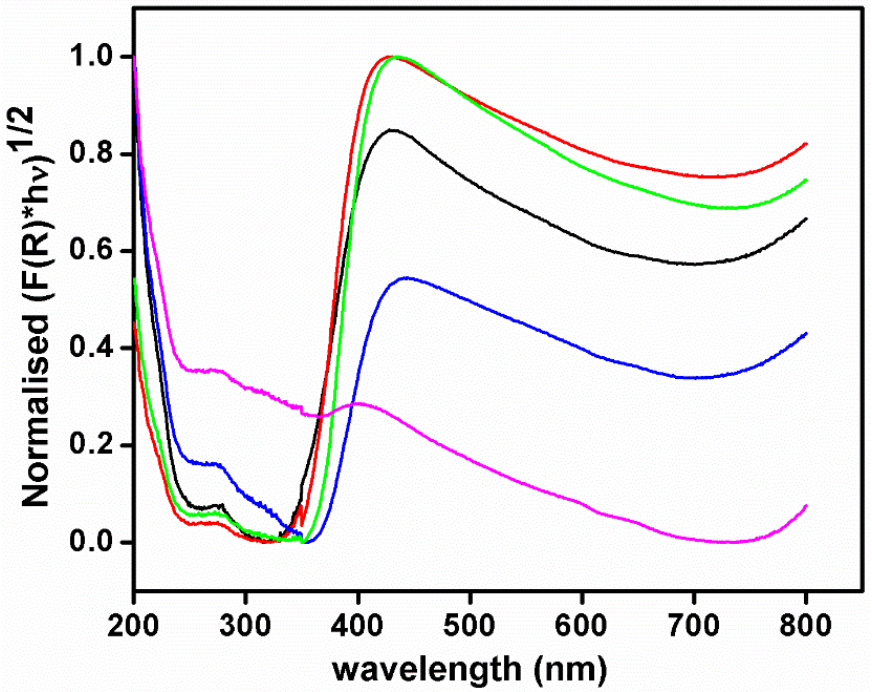

Figure 2.20. Diffused reflectance spectra of 2 wt% CuO impregnated (black) IGZ1, (red) IGZ2, (blue) IGZ3, (green) IGZ4 and (magenta) bulk CuO.

2 wt% CuO are loaded on $InGaO_3(ZnO)_m$ compounds and their absorption characteristics were studied. The absorption spectra of the CuO loaded compounds in comparison with that of bulk CuO (Thomas Baker, 99%) are given in Figure 2.20. Bulk CuO shows a broad visible light absorption band ~ 700 nm. In case of CuO loaded compounds, absorption edges indicating two different absorptions, in UV region (~360 nm) and in visible region (~640 nm) can be observed. UV absorption obviously originates from the parent compounds and broad absorption features extending to the visible light region points to the presence of visible light absorption capability as contributed by CuO. In other words, the visible light absorption feature of CuO is present in the CuO/IGZ composite also.

So it can be anticipated that CuO will act as a sensitizer for IGZ oxides if proper band alignment can be achieved. This was further probed by hydrogen evolution studies carried out for varying amounts of CuO (1, 2, 4 and 10 wt%) loaded in IGZ1. The results indicate an optimum activity for 2 wt% CuO loading for all the compounds (Figure 2.21).

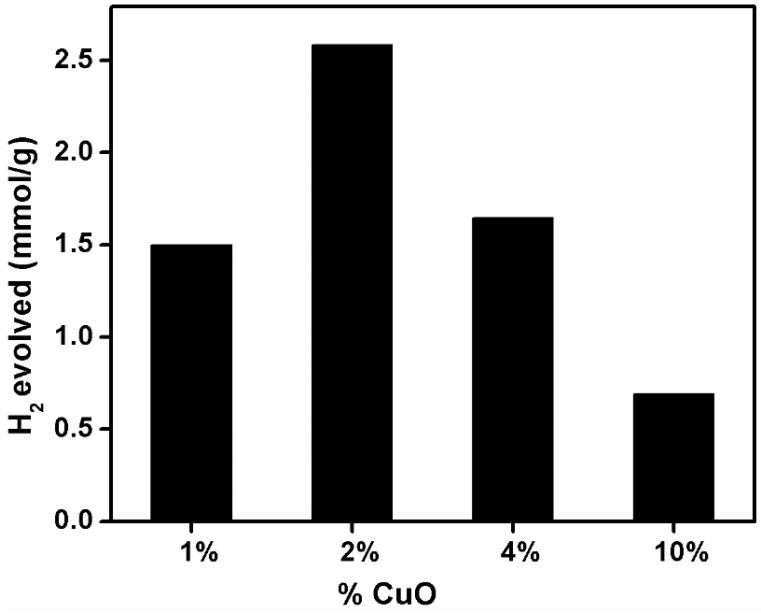

Figure 2.21. H_2 evolution studies carried out for varying amounts of CuO (1, 2, 4 and 10 wt%) loaded in IGZ1 under visible light irradiation of 2 h in 20 v/v% of methanol-water mixture.

The hydrogen evolution obtained for 2 wt% CuO loaded catalysts at different durations are shown in Figure 2.22. It is clear that there is a proportional increase in hydrogen evolution with time demonstrating advantageous kinetics as well as stability of the catalysts. The amount of hydrogen evolved under visible light irradiation of modified photocatalysts is comparable with that for the bare catalysts under UV irradiation. This indicates that electron transfer from IGZ to CuO is not possible as seen in the case of NiO and also the kinetics of the reaction is limited by the activity of IGZ surface sites. On the other hand, an electron transfer to IGZ from the copper oxide can be envisaged based on the broad visible band absorption observed for 2 wt% CuO loaded IGZ series (Figure 2.20). Here CuO is probably acting as a photosensitizer by transferring electrons to the empty conduction bands of IGZ compounds. This was again proved by the negligible H_2 evolution by CuO/SiO_2 catalyst. The photogenerated electrons get accumulated in the conduction

band of CuO and probably recombines since a facile electron acceptor is absent in case of SiO_2.

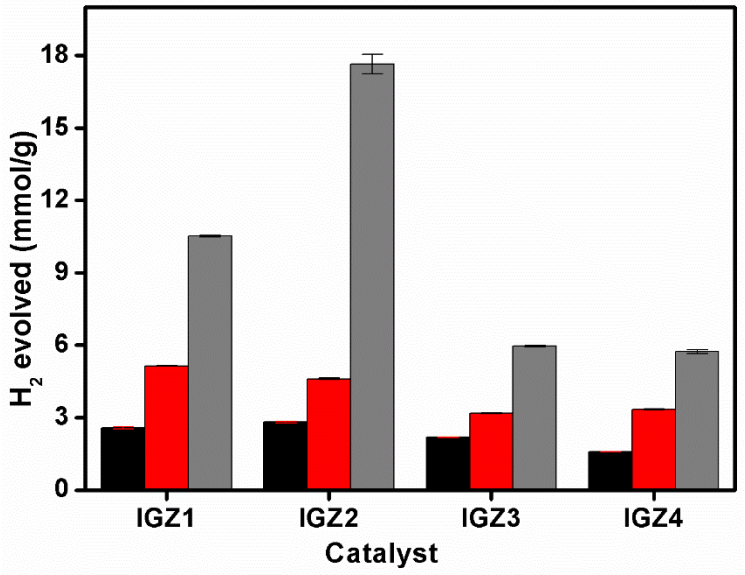

Figure 2.22. H_2 evolution of 2 wt% CuO loaded IGZ 1 to 4 from 20 v/v% methanol–water mixtures under visible light irradiation for (black) 2 h, (red) 4 hand (grey) 8 h.

However, band positions of CuO as observed from literature is not aligned with IGZ bands to facilitate a favorable electron transfer. Reports on the exact positions are conflicting, [38-41] but it can be gleaned that conduction band position of CuO is less negative than that of IGZ compounds. The activity of CuO loaded photocatalysts can then be explained on the basis of the conduction band positions of the parent catalyst and the Cu_2O or any reduced copper oxide species formed during the reaction. The loaded CuO is well dispersed in the IGZ series and the PXRD pattern shows that it is in the nano regime. It can be expected that the size dependent phenomenon can play a role in upward shifting of the conduction band edge of the CuO [42]. Also it is reported that accumulation of photogenerated excess electrons at conduction band of CuO leads to the formation of reduced copper oxide phases including Cu_2O and causes a negative shift in the Fermi level [43]. Presence of Cu_2O or reduced species of Cu in the spent catalyst was unambiguously proved by XPS studies.

In the literature it can be seen that the binding energy for Cu(I) corresponding to Cu $2p_{3/2}$ varies from 932.5 to 933.8 eV and Cu(II) has values ranging from 934 to 935 eV [44-

45]. XPS spectrum of 2 wt% CuO loaded IGZ1 after 4 h visible light irradiation shows two intense peaks at 933.5 eV and 953.52 eV corresponding to Cu $2p_{3/2}$ and Cu $2p_{1/2}$ respectively (Figure 2.23). This points to the presence of Cu(I) species in the reaction

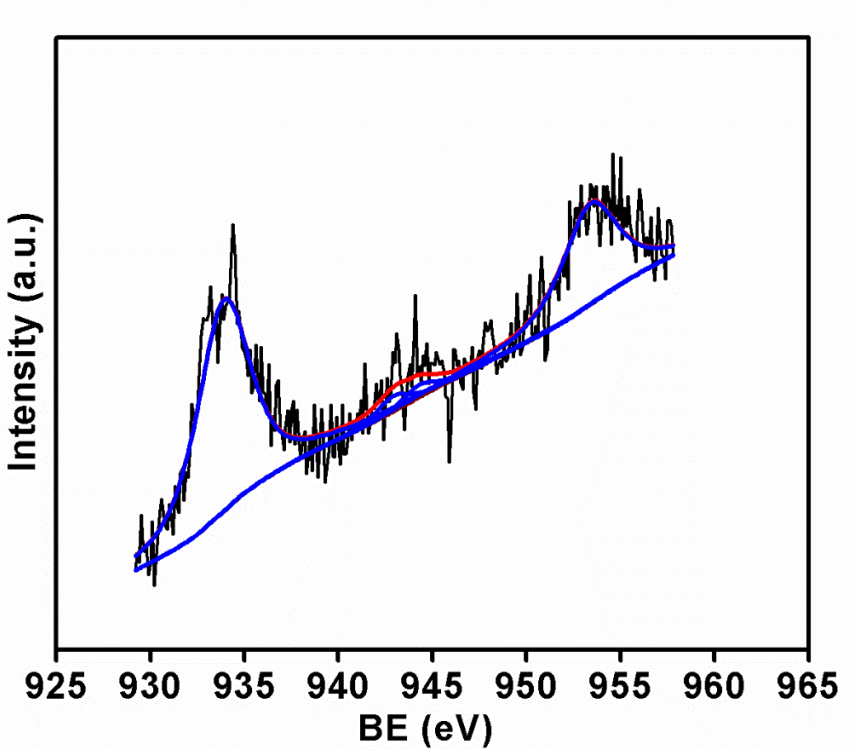

Figure 2.23. Deconvoluted XPS spectra of 2 wt% CuO loaded IGZ1 after 4 h visible light irradiation: (Blue) $Cu2p_{3/2}$ and $Cu2p_{1/2}$ (red) absence or very low intense satellite peak.

mixture after irradiation. This can be further proven by the absence of satellite peak in the XPS spectra. The satellite peak usually appears at a binding energy ~9 eV higher to the main peak in the XPS spectrum of CuO. CuO has a d^9 configuration in the ground state which leads to the satellite feature in the spectrum. On the other hand, the ground state of Cu_2O is full and hence the screening via the charge transfer into the d states is not possible, this results in the absence of a satellite peak in the Cu_2O spectra [46]. The intensity of satellite peak with respect to intensity of main peak ($2p_{3/2}$) in CuO bulk is calculated in literature to be 0.55 [47]. In our sample the value is much lesser than that indicating the absence of any CuO species. It is suggested that the conduction band edge of Cu_2O is placed more negative compared to CuO [48]. This may facilitate interfacial electron transfers from Cu_2O to parent catalysts resulting in water reduction.

The crystal structure of the samples remains the same even after the experiments, which is clear from the PXRD shown in Figure 2.24.

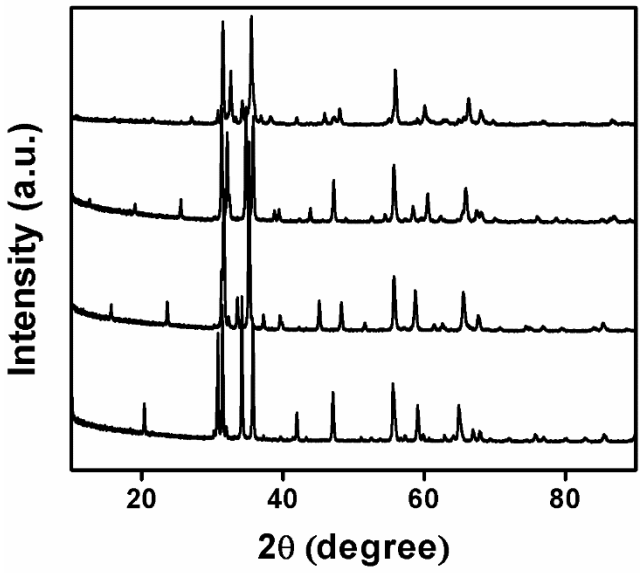

Figure 2.24. PXRD patterns of $InGaO_3(ZnO)_m$ (m = 1 – 4) after photocatalytic water splitting reaction for 2 h.

2.4. Conclusions

The structural characterization of local environments of Ga and Zn in the case of series of compounds $InGaO_3(ZnO)_m$ (m = 1– 4) was carried out by MAS NMR and EXAFS techniques. The MASNMR indicates a gradual shift in geometry from pentacoordinated to tetracoordinated for Ga. However, the EXAFS studies point to a gradual shift in coordination from penta to tetracoordination as we go across the series. Further probing evidences a stratification of the inner Zn/GaO_n layers with an outer layer of ZnO_n and an inner layer with random mixing of Ga and Zn in increasingly tetracoordinated geometry as we go across the series. This shows that the sandwich layer (between In–O layers) assumes the structure of ZnO with corner shared tetrahedra as the layer number increases, pointing to the possibility of gallium oxide solubilizing in this layer. This inner strata most probably has gallium oxide solubilized in ZnO, especially at high m values (due to high amounts of ZnO) and hence, has a wurtzite type structure with corner sharing tetrahedra. This series of compounds, $InGaO_3(ZnO)_m$ (m = 1– 4) are identified as UV active photocatalysts for H_2 evolution from aqueous methanol. The spatial separation within the compounds minimizes

recombination, thereby enhancing hydrogen generation. Here methanol acts as a sacrificial reagent. The UV-visible spectra of the compounds show that they absorb in UV region and the band edge positions estimated from Mulliken electronegativities indicate possible H_2 evolution under UV radiation which is indeed observed. The photocatalytic activity is enhanced two-fold by employing NiO as cocatalyst due to facile electron transfer from conduction bands of $InGaO_3(ZnO)_m$ to NiO which acts as the catalytic sites. A reversal of roles is observed on loading CuO which acts as a visible light sensitizer. In $CuO/InGaO_3(ZnO)_m$ composites, CuO absorbs in visible region due to its narrow band gap and transfers electrons to the semiconductor conduction bands. Appropriate band alignment to facilitate such an electron transfer is attained by rapid accumulation of electrons in the conduction band of CuO leading to the formation of Cu_2O and subsequent shift of Fermi level to more negative potentials. A size dependent phenomenon in the nano regime affecting a conduction band shifting also may add to the band alignment. Most importantly, H_2 evolution activity for parent $InGaO_3(ZnO)_m$ compounds under UV irradiation and their CuO composites under visible light irradiation are found to be similar. This indicates that the catalytic sites are present on $InGaO_3(ZnO)_m$ in both the cases and the rate may be influenced by electron transfer from their conduction bands to the electrolyte. Apparently, this electron transfer is more efficient in case of NiO resulting in an enhanced activity in case of $NiO/InGaO_3(ZnO)_m$ composites.

References

1. Linsebigler, A. L.; Lu, G.; Yates, J. T. *Chem. Rev*., **1995**, *95*, 735.
2. Zou, Z. G.; Ye, J. H.; Sayama, K, Arakawa, H. *Nature* **2001**, *414,* 625.
3. Kato, H.; Asakura, K.; Kudo, A. *J. Am. Chem. Soc*. **2003**, *125*, 3082.
4. Istratov, A. A.; Weber, E. R. *Appl. Phys. A: Mater. Sci. Process***1998**, *66*, 123.
5. Murray, B.; Kagan, C. R.; Bawendi, M. G. *Annu. Rev. Mater. Sci*. **2000,** *30*, 545.
6. Nocera, D. G. *Acc. Chem. Res*. **2012**, *45*, 767.
7. Orita, M.; Tanji, H.; Mizuno, M.; Adachi, H.; Tanaka, I. *Phys. Rev. B* **2000**, *61*, 1811.
8. Nespolo, M.; Sato, A.; Osawa, T.; Ohashi, H. *Cryst. Res. Technol*. **2000**, *35*, 151.
9. Keller, I.; Assenmacher, W.; Schnakenburg, G.; Mader, Z. *Anorg. Allg. Chem*. **2009**, *635*, 2065.

10. Keller, I.; Mader, W. Z. *Anorg. Allg. Chem*., **2010**, *636*, 1045.
11. Omura, H.; Kumomi, H.; Nomura, K.; Kamiya, T.; Hirano, M.; Hosono, H. *J. Appl. Phys*. **2009**, *105*, 093712.
12. Yan, Y.; Pennycook, S. J.; Dai, J.; Chang, R. P. H.; Wang, A.; Marks, T. *Appl. Phys. Lett*. **1998**, *73*, 2585.
13. Schinzer, C.; Heyd, F.; Matar, S. F. *J. Mater. Chem*. **1999**, *9,* 1569.
14. Medvedeva, J. E.; Hettiarachchi, C. L. *Phys. Rev. B: Condens. Matter Mater. Phys*. **2010**, *81*, 125116.
15. Omata, T.; Ueda, N.; Ueda, K.; Kawazoe, H. *Appl. Phys. Lett.* **1994**, *64*, 1077
16. Peng, H.; Song, J. H.; Hopper, E. M.; Zhu, Q.; Mason, T. O.; Freeman, A. J. *Chem. Mater*. **2012***, 24*, 106.
17. Isobe, M.; Kimizuka, N.; Nakamura, N.; Mohri, T. *Acta Crystallogr. Sect. C: Cryst. Struct. Commun*. **1994**, *50*,332.
18. Li, C.; Bando, Y.; Nakamura, M.; Onoda, M.; Kimizuka, N. *J. Solid State Chem*. **1998**, *139*, 347.
19. Nakamura, M.; Kimizuka, N., And, N.; Mohri, T. *J. Solid State Chem.* **1991**, *93*, 298.
20. Toby, B. *J. Appl. Crystallogr.* **2001**, *34*, 210.
21. Kato, K.; Kawada, I.; Kimizuka, N.; Katsura, T. *Z. Kristallogr.* **1975**, *141*, 314.
22. Kimizuka, N.; Mohri, T. *J. Solid State Chem.* **1985**, *60*, 382.
23. Yoshioka, S.; Toyoura, K.; Oba, F.; Kuwabara, A.; Matsunaga, K.; Tanaka, I. *J. Solid State Chem.* **2008**, *181*, 137.
24. Ash, J. S.; Grandinetti, P.J. *Magn. Reson. Chem.* **2006**, *44*, 823.
25. Massiot, D.; Fayon, F.; Capron, M.; King, I.; Calve, S. L.; Alonso, B.; Durand, J. O.; Bujoli, B.; Ganand, Z. H.; Hoatson, G. *Magn. Reson. Chem*. **2002**, *40*, 70.
26. Patzke, G.; Binnewies, M. *Solid State Sci*. **2000**, *2*, 689.
27. Groot, F. D.; Vanko, G.; Glatzel, P. *J. Phys.:Condens. Matter* **2009**, *21*, 104207.
28. Chandrasekaran, P.; Chantal, S.; Stieber, E.; Collins, T. J.; Que Jr., L.; Neese, F.; Beer, S. D. *Dalton Trans.* **2011**, *40*, 11070.
29. Lafuerza, S.; Subias, G.; Garcia, J.; Matteo, S. D.; Blasco, J.; Cuartero, V.; Natoli, C. R. *J. Phys.: Condens. Matter* **2011**, *23*, 325601.

30. Domen, K.; Kudo, A.; Onishi, T.; Kosugi, N.; Kuroda, H. *J. Phys. Chem*. **1986**, *90*, 292.
31. Murphy, A. B. *Sol. Energy Mater. Sol. Cells* **2007**, *91*, 1326.
32. Kim, Y. F.; Atherton, S. J.; Brigham, E. S.; Mallouk, T. E. *J. Phys. Chem.* **1993**, *97*, 11802.
33. Gelderman, K.; Lee, L.; Donne, S. W. *J. Chem. Educ*. **2007**, *8,* 685.
34. Hardee, K. L.; Bard, A. J. *J. Electrochem. Soc*. **1977**, *124*, 215.
35. . Li, G.; Dimitrijevic, N. M.; Chen, L.; Rajh, T.; Gray, K. A. *J. Phys. Chem. C*, **2008**, *112* , 19040.
36. Kudo, A.; Sayama, K.; Tanaka, A.; Asakura, K.; Domen, K.; Maruya, K.; Onishi, T. *J. Catal*. **1989**, *120*, 337.
37. Sayama, K., Yase, K.; Arakawa, H.; Asakura, K.; Tanaka, A.; Domen, K.; Onishi, T. *J. Photochem. Photobiol. A* **1998**, *114*, 125.
38. Koffyberg, F. P.; Benko, F. A. *J Appl. Phys.* **1982**, *53*, 1173.
39. Sukhorukov, Y. P.; Gizhevskii, B. A.; Mostovshchikova, E. V.; Yermakov, A. Y.; Tugushev, S. N.; Kozlov, E. A. *Tech. Phys. Lett.* **2006**, *32*, 132.
40. Wang, N.; He, H.; Han, L. *Appl. Surf. Sci*. **2010**, *256*, 7335.
41. Rehman, S.; Mumtaz, A.; Hasanain, K. *J Nanopart. Res.* **2011**, *13*, 2497.
42. Barreca, D.; Fornasiero, P.; Gasparotto, A.; Gombac, V.; Maccato, C.; Montini, T.; Tondello, E. *ChemSusChem*. **2009**, *2*, 230.
43. Bandara, J.; Udawatta, C. P. K.; Rajapakse, C. S. K. *Photochem. Photobiol. Sci*. **2005**, *4*, 857.
44. Parmigiani, F.; Pacchioni, G.; Illas, F.; Bagus, P. S. *J. Electron. Spectrosc. Relat. Phenom.* **1992**, *59*, 255.
45. Mclntyre, N. S.; Cook, M. G. *Anal. Chem.* **1975**, *47*, 2208.
46. Thuler, M. R.; Benbow, R. L.; Hurych, Z. *Phys. Rev. B* **1982**, *26*, 669.
47. J. Ghijsen, L. H. Tjeng, J. van Elp, H. Eskes, J. Westerink, G. A. Sawatzky and M. T. Czyzyk, *Phys. Rev. B*, 1988, **38**, 11322.
48. K. Rajeshwar, N. R. de Tacconi, G. Ghadimkhani, W. Chanmanee and C. Janaky, *ChemPhysChem*. **2013**, *14*, 2251.

Chapter 3

Studies on local coordination environments of Fe and Zn in $InFeO_3(ZnO)_m$ (m = 1– 4): Photocatalytic H_2 evolution activity of the compounds under visible light irradiation without a cocatalyst

3.1. Introduction

A suitable photocatalytic material should possess sufficiently small band gap for utilizing more abundant visible light region in the solar spectrum [1]. Also the valence band and conduction band positions with respect to the reduction and oxidation potentials of water should be appropriate to drive overall water splitting as discussed in chapter 1. The advantages of layered compounds, especially structurally anisotropic ones, in terms of spatially separating the carrier generation and carrier mobility sites is elaborated in chapters 1 and 2. Also, series of compounds $InGaO_3(ZnO)_m$ (m=1-4), with such anisotropically layered structures are shown to be good photocatalysts for water splitting in presence of cocatalysts. However, this series of compounds, along with numerous other reported semiconductor oxides have high band gap energies, limiting their usage to only UV light region. Most of the reported visible light active catalysts are metal sulphides, metal nitrides and metal oxynitrides etc. which are susceptible to recombination of the photogenerated charge carriers due to the close proximity of conduction and valence bands [2-6]. Doped metal oxides, solid solutions, incorporating sensitizer or using complex systems have their own limitations [6]. So an attempt is made to identify an efficient visible light driven water splitting catalyst with inherent charge separation possibility. As per the structural and photocatalytic activity studies on $InGaO_3(ZnO)_m$ (m = 1−4), it can be thought that the presence of a transition metal ion instead of gallium can contribute to the valence band positions of the series of compounds. Hence, isostructural compounds $InFeO_3(ZnO)_m$ (m = 1−4) are chosen whose applications in thermoelectric coatings are widely studied, but photocatalytic activities are least explored. As in the case of isostructural Ga compounds, here also spatial separation can play an important role in the catalytic activity. Also the contribution of Fe towards the band structure can have a major impact on the activity in the visible light. Usually iron oxides possess small band gaps which may lead to recombination of photogenerated charges. Various sources report that iron oxides coupled with other semiconductors in different ways act as excellent photocatalysts [7-10]. Hence, the focus of the work described in this chapter is on structural studies as well as water splitting activity under visible light irradiation of this structurally anisotropic series of compounds, $InFeO_3(ZnO)_m$ (m = 1−4). The unique electronic and band structure resulting from such a structural anisotropy makes this series potential

materials for addressing recombination issues associated with semiconductor photocatalysts with the added advantage of visible light activity.

3.2. Experimental section

3.2.1. Synthesis of $InFeO_3(ZnO)_m$ (m = 1– 4)

A series of compounds of $InFeO_3(ZnO)_m$ (m = 1 to 4) were prepared by means of solid-state synthesis using In_2O_3 (Sigma Aldrich,99.99%), Fe_2O_3 (Sigma Aldrich, 99.99%), and ZnO (Sigma Aldrich,99.99%) as starting materials [11-13]. The starting powders with appropriate molar ratios of the oxides corresponding to $InFeO_3(ZnO)_m$ (m = 1 to 4) were thoroughly ground and heated in a platinum crucible progressively to 700, 900, and 1000 °C and kept at each temperature for 12 h. The resulting powders were mixed with 2 wt% isopropyl alcohol and pressed into pellets and sintered finally at 1350 °C for 12 h with two intermittent grindings. The compounds are named as IFZ1, IFZ2, IFZ3 and IFZ4 for m=1, m=2, m=3 and m=4 respectively. $ZnFe_2O_4$ was synthesized through solid state method, Fe_2O_3 (Sigma Aldrich, 99.99%) and ZnO (Sigma Aldrich, 99.99%) were stoichiometrically mixed and heated at 1000 °C for 12 h.

3.2.2. Characterization

The details of the instruments and procedures used for PXRD, Rietveld refinement, surface area measurements and band gap determination are same as those described in chapter 2. EXAFS measurements on the samples were carried out at the Energy Scanning EXAFS beamline (BL-09) at INDUS-2 synchrotron source at RRCAT, Indore.

3.2.3. Catalytic testing

The photocatalytic setup is same as explained in section 2.3.1c in chapter 2. 50 mg of photocatalyst powder was dispersed in a reactant solution (25 mL). Various methanol– water ratios (v / v%- 4%, 8%, 12%, 16%, 20% and 24%) were tried. Experiments were repeated with glycerol as sacrificial agent.

3.3. Results and discussion

Powder XRD patterns of the synthesized materials are displayed in Figure 3.1, which shows highly crystalline diffraction peaks, clearly indicating the formation of required structures (JCPDS card Nos. 40– 0250, 40–0243, 40–0244, and 40–0245 for IFZ1, IFZ2, IFZ3, and IFZ4, respectively) [11]. Structural or electronic characterization of

the Fe analogues of the series, $InBO_3(ZnO)_m$ is rare. However, we can draw important inferences from isostructural compounds $InGaO_3(ZnO)_m$, which are structurally well characterized and discussed in detail in chapter 2. Members of the series in which m is odd are reported to crystallize in rhombohedral phase with space group R-3m, and those with m even crystallize in hexagonal phase with space group $P6_3/mmc$ [14-15]. It is observed from the PXRD patterns that $ZnFe_2O_4$ phase is present as impurity in very minor amount in all compounds except IFZ4. The PXRD pattern of synthesized $ZnFe_2O_4$ is given in appendix 2.3. In order to quantify $ZnFe_2O_4$ phase, quantitative phase analysis by Rietveld refinement method using GSAS-EXPGUI software was also done [16]. The impurity phase fractions are tabulated in Table 3.1.

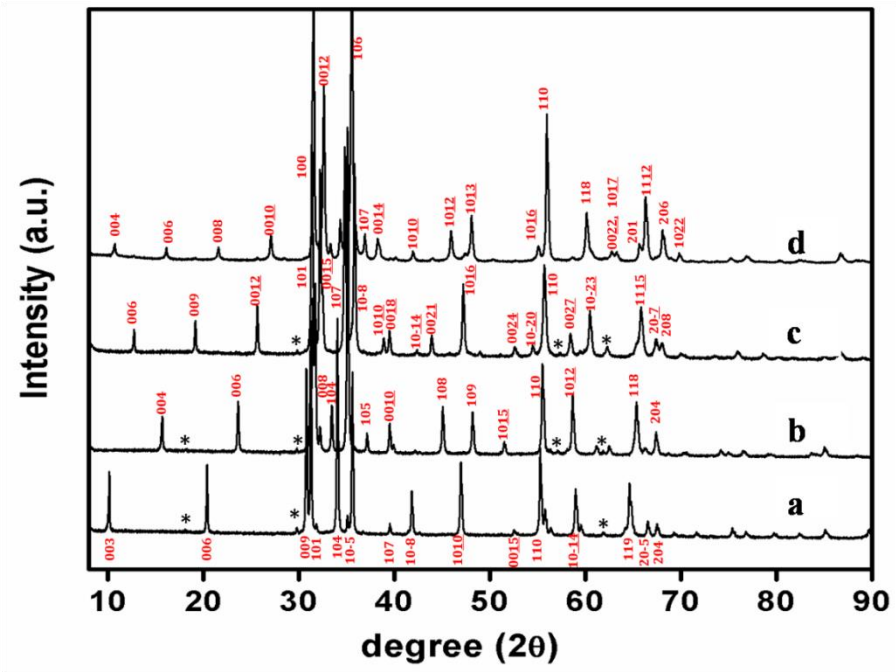

Figure 3.1. PXRD patterns of (a) IFZ1, (b) IFZ2, (c) IFZ3 and (d) IFZ4. The impurity phases ($ZnFe_2O_4$) are marked as *. hkl planes are indicated against the peaks.

Table 3.1. Impurity phase fractions ($ZnFe_2O_4$) in IFZ1 to IFZ4

Compound	Impurity Phase (weight fraction in %)
IFZ1	3.76
IFZ2	1
IFZ3	1.7
IFZ4	-

Table 3.2. Refinement and structural parameters of IFZ1 to IFZ4

Parameters		IFZ1	IFZ2	IFZ3	IFZ4
$\chi 2$		2.431	2.368	4.179	7.617
wRp (%)		5.29	5.19	6.21	9.12
Rp (%)		3.96	4.02	4.52	6.32
a (Å)		3.3205(0)	3.3105(0)	3.2977(0)	3.2928(0)
c (Å)		26.1065(2)	22.5871(2)	41.6334(5)	32.9616(0)
Fe	x	0	0	0	0.6667
	y	0	0	0	0.3333
	z	0.2169	0.25	0.1347	0.25
	U_{iso}	0.0193	0.0346	0.0223	0.0145
Zn1	x	0	0.6667	0	0.6667
	y	0	0.3333	0	0.3333
	z	0.216 9	0.365 2	0.739 8	0.091 4
	U_{iso}	0.0250	0.0176	0.0150	0.0250
O1	x	0	0.6667	0	0.6667
	y	0	0.3333	0	0.3333
	z	0.126 3	0.450 1	0.306 9	0.040 9
	U_{iso}	0.0198	0.0303	0.0259	0.0342
O2	x	0	0	0	0
	y	0	0	0	0
	z	0.290 17	0.345 1	0.085 5	0.1118
	U_{iso}	0.0327	0.0250	0.0250	0.0140
O3	x		0.6667	0	0.6667
	y		0.3333	0	0.3333
	z		0.2500	0.8058	0.1776
	U_{iso}		0.0250	0.0197	0.0190

In (0,0,0) for all the four compounds and U_{iso} in IFZ1, IFZ2, IFZ3 and IFZ4 are 0.0180, 0.0149, 0.0197 and 0.0236 respectively; O4 in IFZ4 (0,0,0.25) and U_{iso} is 0.0370; Zn2 in IFZ3 (0,0, 0.1348) and U_{iso} is 0.0442 and IFZ4 (0,0, 0.1702) and U_{iso} is 0.0069.

The atomic positions of pentacoordinated Zn and Fe in IFZ1 and IFZ2 were constrained to be identical with 50% occupancy, and site fractions were constrained to sum to unity. The refinement proceeded more or less smoothly with reasonable refinement parameters. Initially, cell parameters were refined with a few background terms and in a stepwise manner, atomic positions, occupancies, and isothermal parameters were included. After that, profile functions were refined, and again cell parameters, atomic parameters, and isothermal parameters were refined with increasing background terms. The structural and refinement parameters are tabulated in Table 3.2. The Rietveld refinement plots are shown in Figures 3.2 and resultant bond

lengths are given in Table 3.3. The structure of this family of compounds consists of edge shared octahedra of indium with oxygen. Fe and zinc ions occupy trigonal bipyramidal (TBP) or tetrahedral (Td) geometries and form blocks whose thickness is dependent on the number of ZnO layers. These Fe/ZnO_n blocks are sandwiched between InO_2 octahedra. The coordination geometry of Zn ions was earlier believed to change between TBP and Td in m odd and even members with Fe site geometry constant in TBP as shown in Figure 3.3. However, studies on isostructural $InGaO_3(ZnO)_m$ evidenced a gradual change of pentacoordination to tetracoordination for both Ga and Zn in the sandwich layer as we go across the series with increase in ZnO amount.

These structural characteristics play a pivotal role in rendering these materials as potential candidates for spatial separation of photogenerated charges. Energetically favourable conduction pathways for the electrons are suggested to occur in the InO_6 octahedral layers in $InFeO_3(ZnO)_m$, and charge generation is believed to occur in the sandwich layer comprising of Fe/ZnO_n coordination geometries [17-18]. Hence structural detail of this region is of paramount importance. The structural studies by PXRD only give an average picture of Zn and Fe coordination, since they may be placed in a random fashion in the sandwich layer. It is desirable to use a technique that can differentiate the local variations in coordination of Zn and Fe separately in the layer.

In view of this, we studied the Zn and Fe coordination characteristics in the sandwich layer using EXAFS. At the outset, it is observed that Zn coordination changes from TBP to Td across the series; however, Fe coordination is found to remain in TBP in all the four members. Normalized EXAFS spectra of all four compounds at Fe K-edge and Zn K- edge are given in Figure 3.4a and Figure 3.4b respectively.

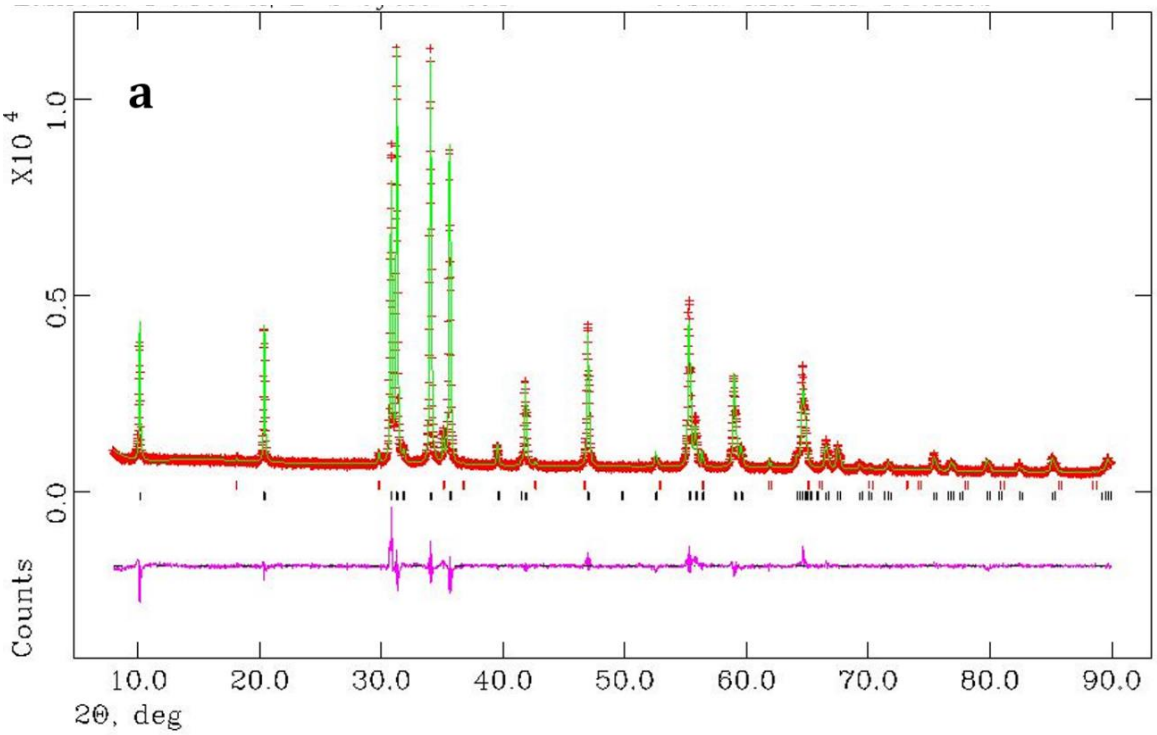
a
X10 4
1.0
0.5
0.0
Counts
10.0
20.0
30.0
40.0
50.0
60.0
70.0
80.0
90.0
2Θ, deg

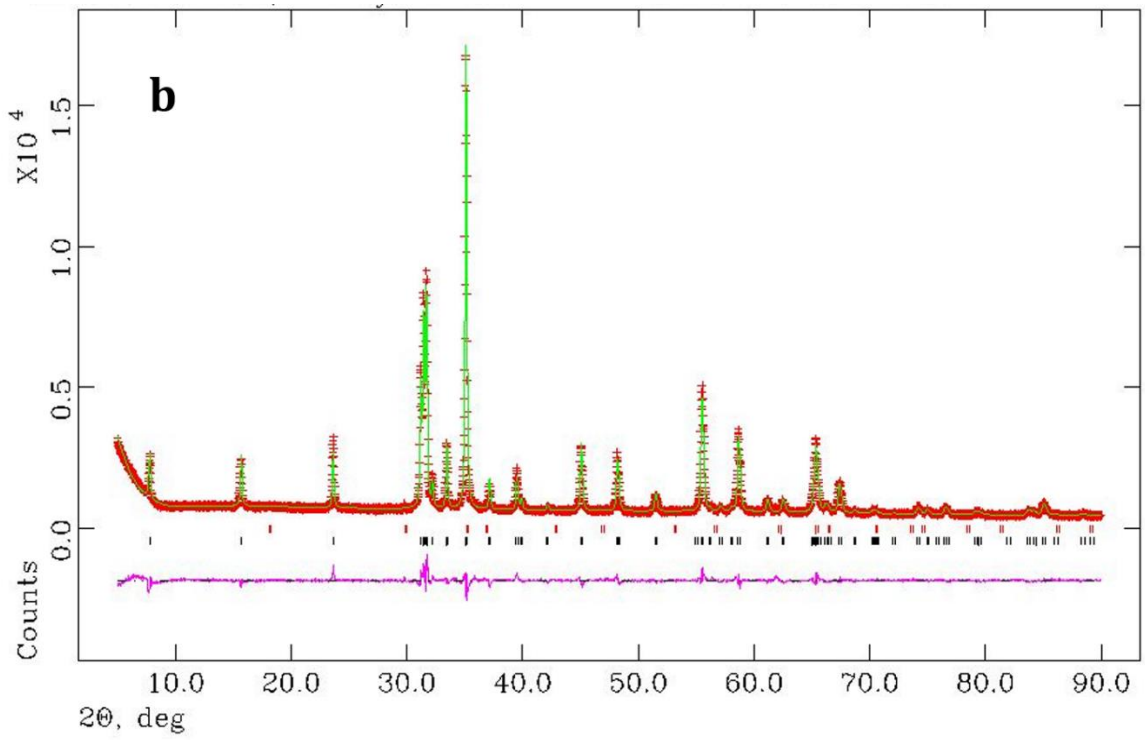
b
X10 4
1.5
1.0
0.5
0.0
Counts
10.0
20.0
30.0
40.0
50.0
60.0
70.0
80.0
90.0
2Θ, deg

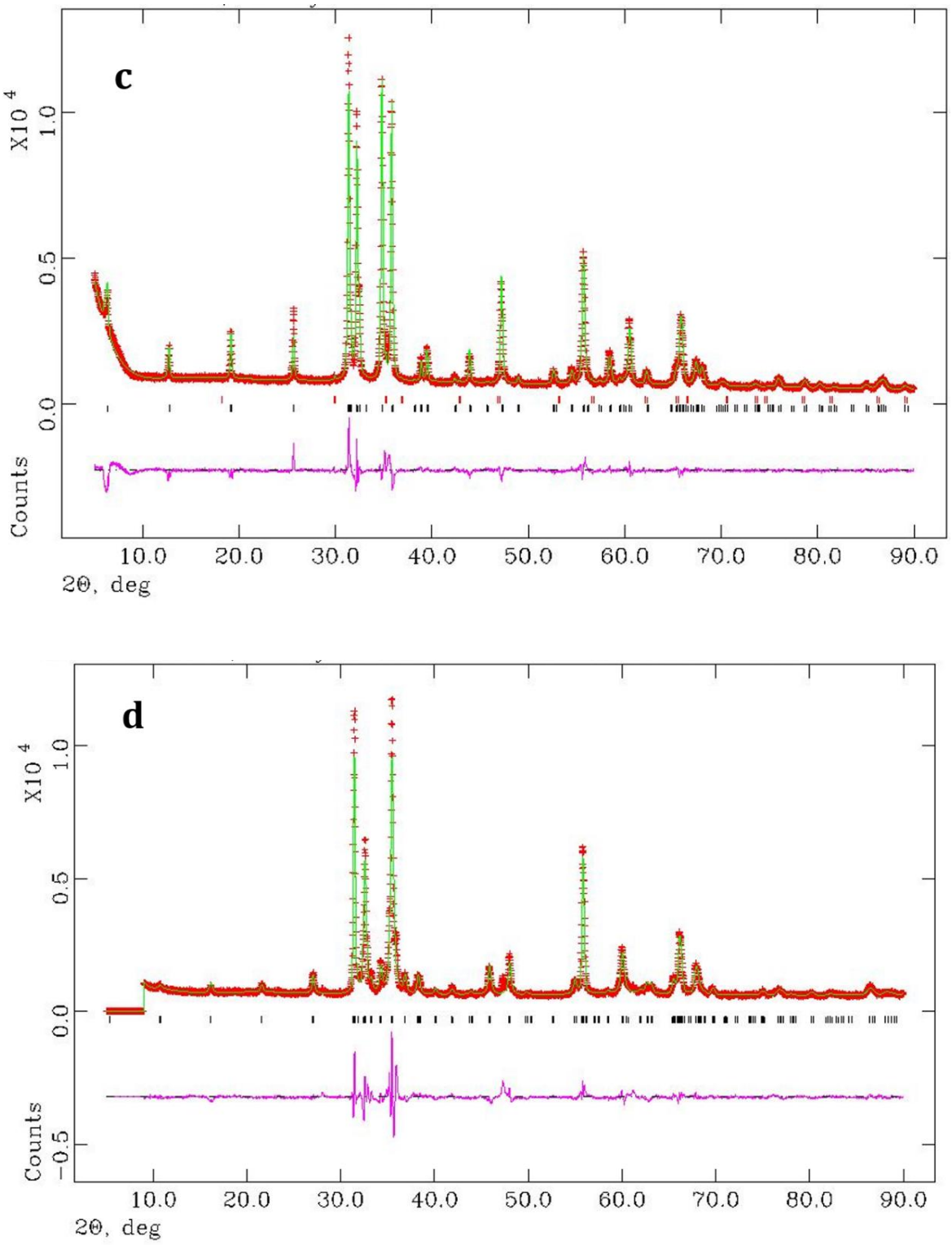

Figure 3.2. Rietveld refinement of the PXRD pattern of (a) IFZ1, (b) IGF2, (c) IGZ3 and (d) IFZ4. Red line represents experimental data, green line is the Rietveld fit and pink line represents difference plot. Vertical lines (black) are the expected positions for main phase and vertical lines (red) are the expected positions for the impurity phase.

Table 3.3 Bond lengths of cation polyhedra in $InFeO_3(ZnO)_m$ as obtained from PXRD refinement.

IFZ1		IFZ2		IFZ3		IFZ4	
In-O2(x6)	2.249	In-O1(x6)	2.219	In-O1(x6)	2.179	In-O1(x6)	2.331
Fe-O1(x4)	1.946	Fe-O2(x2)	2.147	Fe-O2(x1)	2.139	Fe-O3(x2)	2.387
Fe-O2 (x1)	1.887	Fe-O3(3)	1.911	Fe-O3(x3)	1.903	Fe-O4(x3)	1.901
Zn1-O1 (x3)	1.943	Zn1-O1(x1)	1.917	Fe-O3(x1)	2.472	Zn1-O1(x1)	1.664
Zn1-O1 (x1)	2.225	Zn1-O2(x3)	1.965	Zn1-O1(x1)	1.951	Zn1-O2(x3)	2.016
Zn1-O2 (x1)	1.905			Zn1-O2(x3)	1.959	Zn2-O2(x1)	1.926
				Zn2-O2(x1)	2.059	Zn2-O3(x1)	1.916
				Zn2-O3(x3)	1.909	Zn2-O3(x2)	1.917

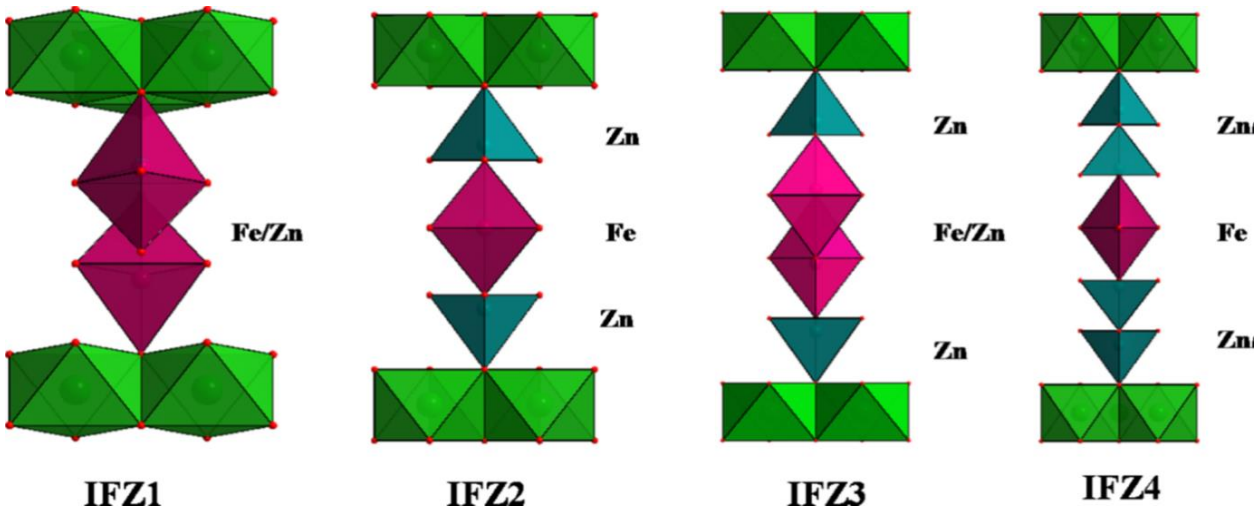

Figure 3.3. Polyhedral representations of $InFeO_3(ZnO)_m$ (m = 1 – 4) based on PXRD refinement parameters.

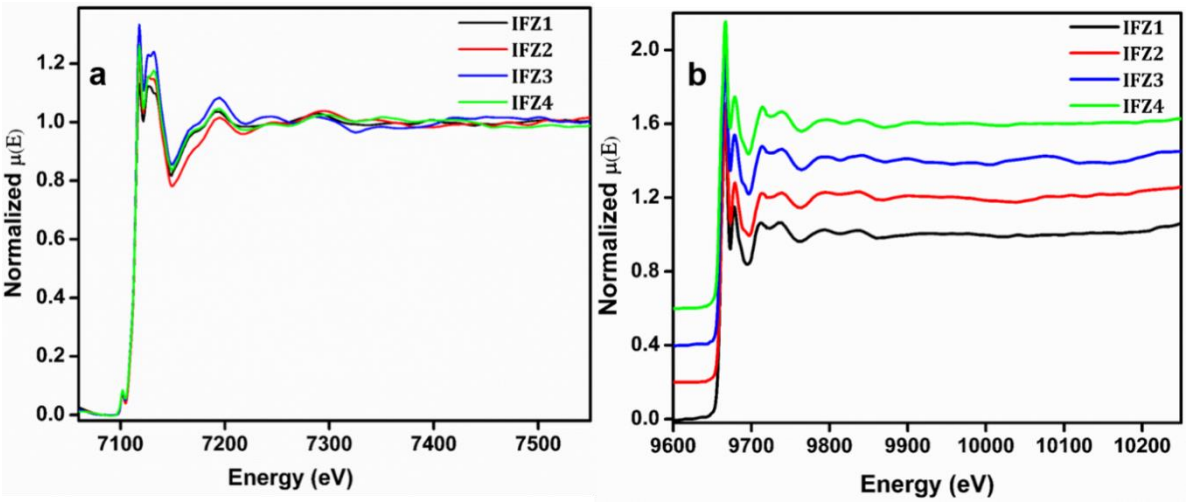

Figure 3.4. Normalized EXAFS spectra of $InFeO_3(ZnO)_m$ for (m=1 – 4), a) at Fe K-edge and b) at Zn K-edge.

Fourier-transformed EXAFS spectra for the $InFeO_3(ZnO)_m$ samples with IFZ1, IFZ2, IFZ3, and IFZ4 measured at Zn edges and Fe K-edge are shown in Figure 3.5a and Figure 3.5b respectively. The fitted spectra are given in Figure 3.6. For IFZ1 and IFZ2, the EXAFS spectra are fitted with a model where the Zn atom is surrounded by five oxygen atoms. However, for IFZ2, Zn is considered in Td structure, whereas for IFZ1 the coordination is taken as TBP. Zn is found to be pentacoordinated in IFZ1 and IFZ2 with four bonds with lengths ~1.9 Å and a long bond of ~2.3 Å. The contribution of fifth oxygen atom is because of non-bonded oxygen from Fe polyhedra.

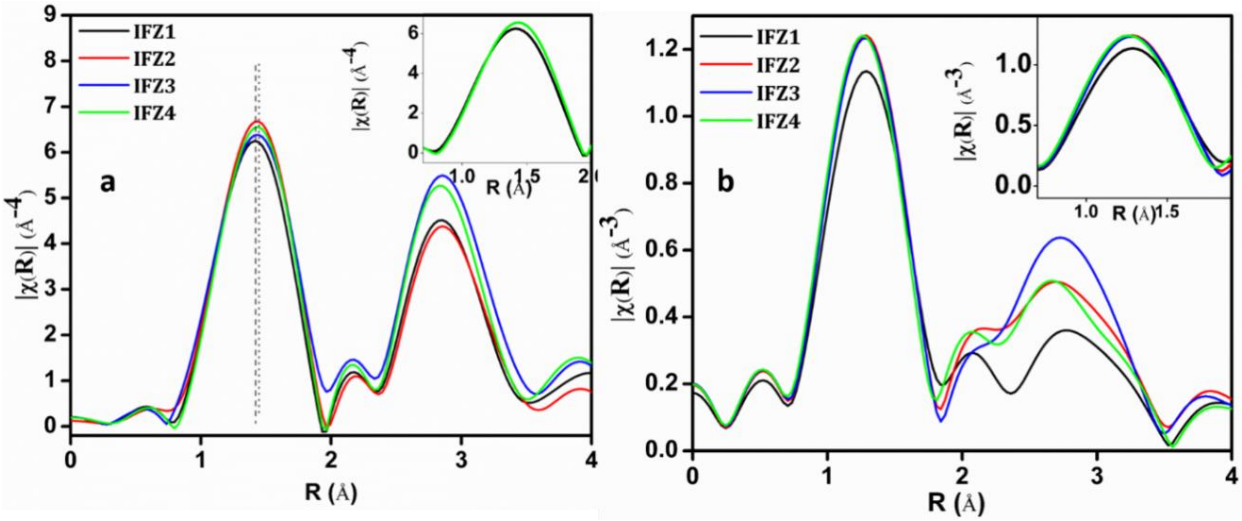

Figure 3.5. Fourier transformed EXAFS spectra of $InFeO_3(ZnO)_m$ (m = 1 – 4) at (a) Fe K-edge and (b) Zn K-edge; (inset) first coordination shell of all the compounds.

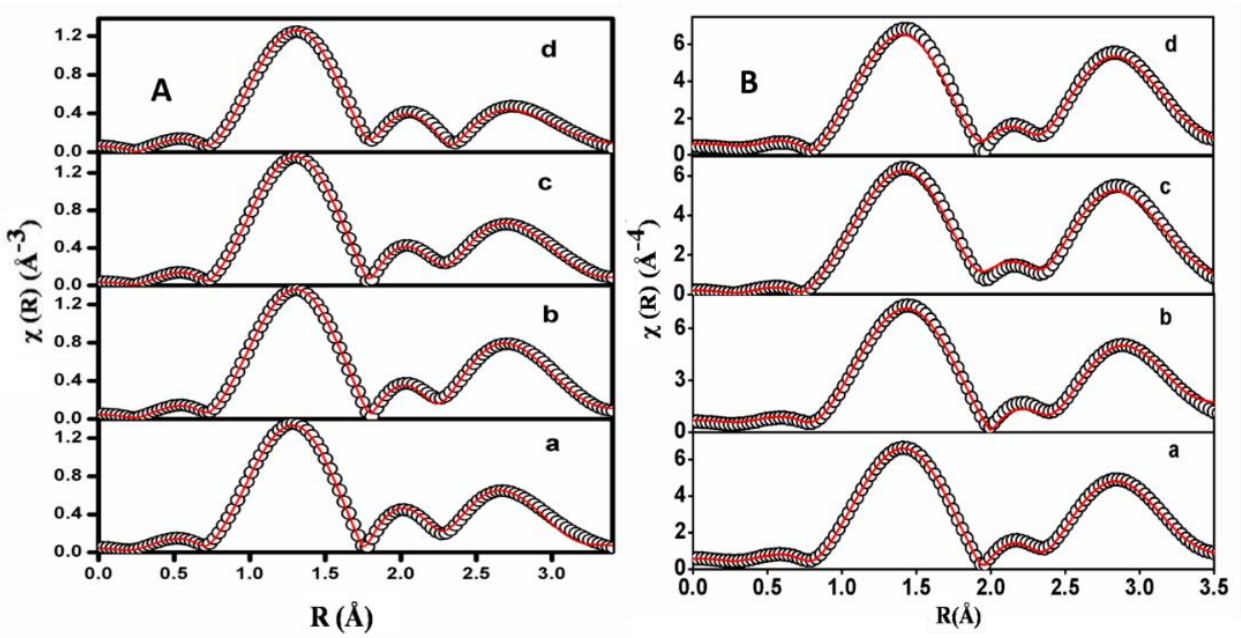

Figure 3.6. Fitted Fourier transformed EXAFS spectra of (a) IFZ1, (b) IFZ2, (c) IFZ3 and (d) IFZ4 at (A) Fe K-edge and (B) Zn K-edge, (scatter points) and theoretical fit (solid line).

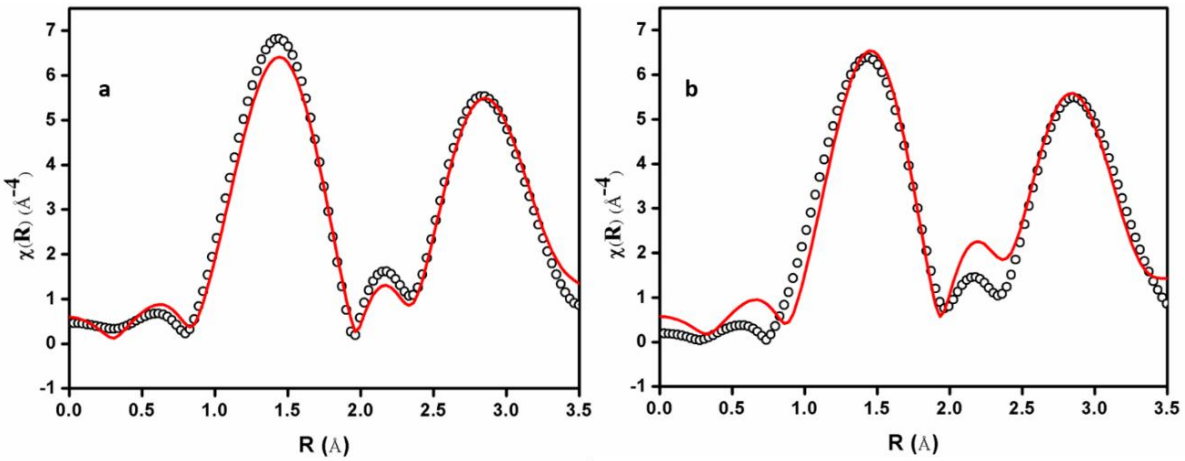

Figure 3.7. Fitted Fourier transformed EXAFS spectra of (a) IFZ3 and (b) IFZ4 at Zn K-edge (scatter points) and theoretical fit (solid line) fitted with TBP structure. The fitting parameters are not sensible for Zn coordination in TBP. The fitted spectra also shows that Zn is not in TBP.

Figure 3.7 shows the attempt to fit Zn in TBP coordination for FT EXAFS spectra of IFZ3 and IFZ4. Better results are obtained when experimental data are fitted with Td Zn sites for both IFZ3 and IFZ4 as represented in Figure 3.6B. Here, Zn occupies Td coordination with bond lengths ranging from 1.82 to 1.94 Å. Note that the contribution of Zn–O coordination in the above spectra (phase not corrected) up to ~2.0 Å is due to the two Zn–O shells. For IFZ3 and IFZ4 this contribution comes from oxygen shells at

~1.9 and 2.0 Å having oxygen coordination of 1 and 3, respectively, for Td structure and 3 and 1 for TBP structure, TBP having another oxygen at 2.3 Å. The first coordination shell, which is shown in the inset of Figure 3.5 in enlarged scale, is found to shift toward higher R values from IFZ1 to IFZ4. Since contributions at higher R values are larger in case of Td structure, samples with higher m value have shown better fitting with Td structure. Note that the FT-EXAFS spectra in the range from 2.0 to 3.5 Å is due to the contributions from further shells of Fe, Zn, and In. Also note that for all the samples, fitting of FT- EXAFS spectra was carried out assuming both TBP and Td structures and the best fit results obtained by $\chi 2$ minimization were accepted. Figure 3.6A shows the Fourier-transformed EXAFS spectra of all the compounds measured at Fe edges along with the best-fit theoretical spectra using a model where Fe coordination corresponds to TBP structure. It can be seen from Table 3.4 that, in all the compounds, Fe is surrounded by three oxygen atoms at a distance of 1.91–1.94 Å and two at a distance of 2.22–2.27 Å.

Table 3.4. Local structural parameters for $InFeO_3(ZnO)_m$ (m = 1 – 4) evaluated by EXAFS measurements at Zn and Fe K-edge.

Paths	Parameters	IFZ1	IFZ2	IFZ3	IFZ4
Zn-O	R (Å)	1.94	1.96	1.85	1.82
	N	4	4	1	1
Zn-O	R (Å)	2.33	2.36	1.93	1.94
	N	1	1	3	3
Fe-O	R (Å)	1.93	1.91	1.92	1.91
	N	3.09	3.09	3.09	3
Fe-O	R (Å)	2.27	2.23	2.23	2.22
	N	2.2	2	2	2

In comparison to the reasonably uniform trigonal bipyramidal bond lengths of Fe, pentacoordinated geometry of Zn seems to be highly distorted with one apical bond shortened subsequently elongating the other apical bond. Note also that the oxygen coordinations in the Fourier-transformed EXAFS spectra mainly contribute up to 1.9 Å. As can be seen from the inset of Figure 3.5 in enlarged scale, the first peak position is

exactly similar in all the four samples, which has led to similar oxygen coordination in all the samples. Only difference is that in case of the m = 1 sample, the first peak amplitude is reduced and its width is increased because of higher σ^2, which indicates structural and thermal disorder. The spectra in the range of 1.9 to 3.5 Å, however, is indeed different from sample to sample, and this is due to contributions from Fe–Fe and Fe–Zn bonds.

Computational studies on the Ga analogues reported earlier have evidenced that the bottom of the conduction band consists of contributions from In 5s only, and valence band contribution is from O 2p orbitals [18]. It is possible that presence of Fe with partly filled 3d orbitals will lead to a better orbital mixing with the ligand orbitals, and this is observed in case of the pre-edge structure of EXAFS spectrum in Fe K-edge. It can be seen from Figure 3.8 that the pre-edge feature (1s to 3d/4p transition) is quite prominent and that the peak height is marginally increasing as ZnO layer number increases. This may be due to slightly enhanced Fe 3d–O 2p mixing although local coordination remains the same. The pre-edge is quite sensitive to the coordination number and orbital geometry and hence may indicate an increase in the coordination of Fe [19] or to a perturbation in the covalent mixing of 3d orbital with ligand valence orbital [20].

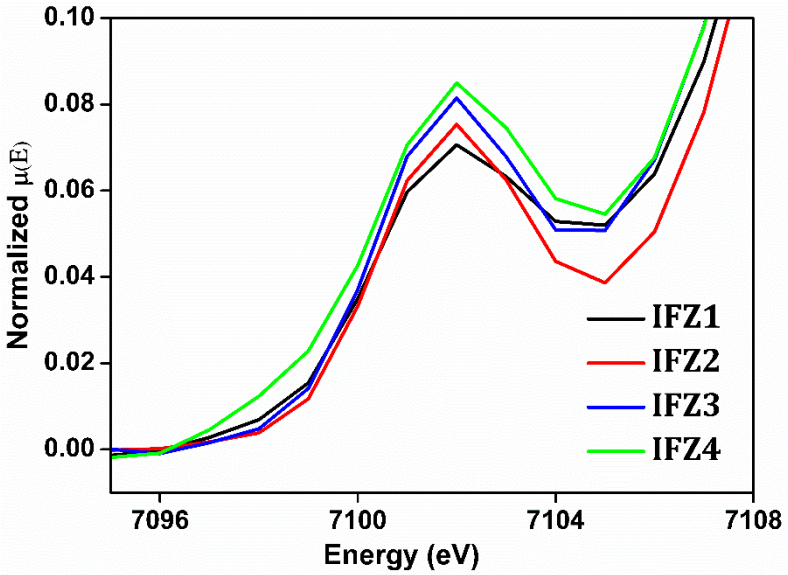

Figure 3.8. Pre-edge feature in the EXAFS spectra of IFZ1, IFZ2, IFZ3 and IFZ4.

The centroids of the pre-edge features for all the samples are at same energy and are coinciding with that of Fe_2O_3 standard sample. This is a clear indication [21] that oxidation state of Fe remains in +3 in all the samples. This would also have an effect in the band gap energies of the compounds. UV–vis absorbance spectra of the series indeed show visible light absorption, which indicates much lower band gap energy compared to their Ga analogues. This may point to some contribution from Fe electronically or structurally.

A relation of reflectance to Kubelka–Munk factor, $F(R) = (1 - R)^2/2R$ [22], was used to calculate the band gap energies. The band gap energies are estimated in this way to be 2.85, 2.96, 2.97, and 3.02 eV for m = 1–4 compounds, respectively (Figure 3.9). No marginal enhancement of band gap energy occurs with increase in ZnO amount. However, as expected these compounds have much smaller band gap energies when compared to their Ga analogous. It is interesting to examine the signature of Fe in the diffused reflectance spectra. The colours of oxides containing Fe have been of interest due to their use as pigments. For oxides containing Fe^{3+}, a Fe^{3+}- O^{2-} charge transfer transition leads to a strong optical absorption in the near UV. The resultant peak typically extends far enough into the visible region to give a yellow colour. Usually the lower energy d-d transitions are forbidden; however they are allowed under various conditions. In the case of iron oxides, this happens due to the broadening of d states into bands as a consequence of the close packing of atoms in the solid state and this broadening increases as the Fe-Fe distances decrease with increasing Fe concentration [23].

An attempt in calculating flat band potentials based on Mulliken electronegativity was taken up [24]. Details of the calculations are given in appendix 2.4, and the band positions are represented in relation with standard hydrogen electrode in Figure 3.10. It is clear that the conduction band levels of all four compounds are placed energetically close to hydrogen reduction potential, which would be very advantageous in electron transfer and catalysis. Also, it is observed that as ZnO amount increases, valence band values become deeper. An interesting zigzag pattern is observed in the conduction band values with *m* even members showing slightly enhanced values when compared to m odd members.

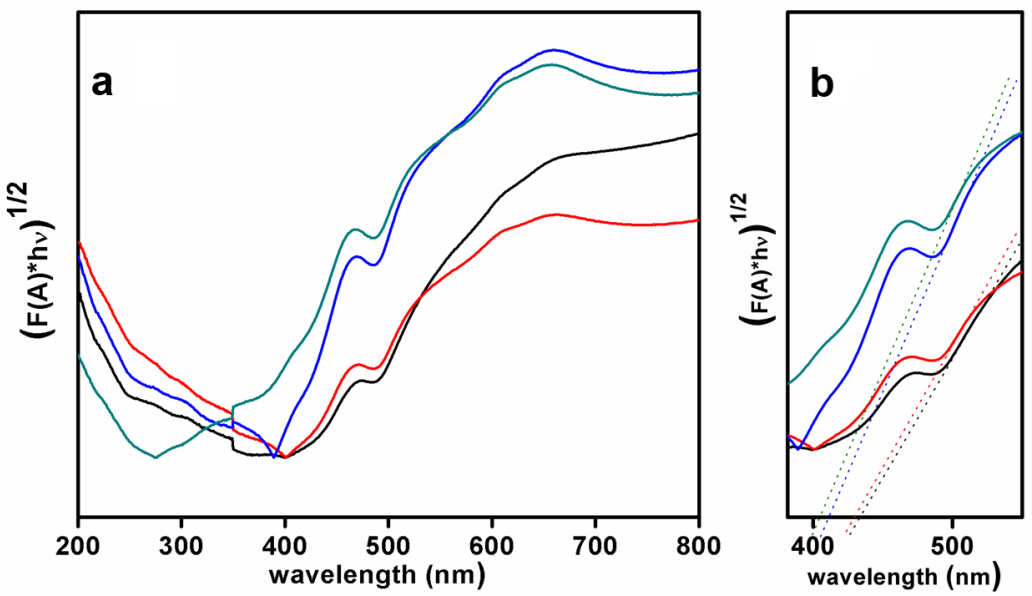

Figure 3.9. (a) Diffused reflectance spectra of IFZ1, IFZ2, IFZ3 and IFZ4. (b) The dotted lines indicate band gaps in the visible region.

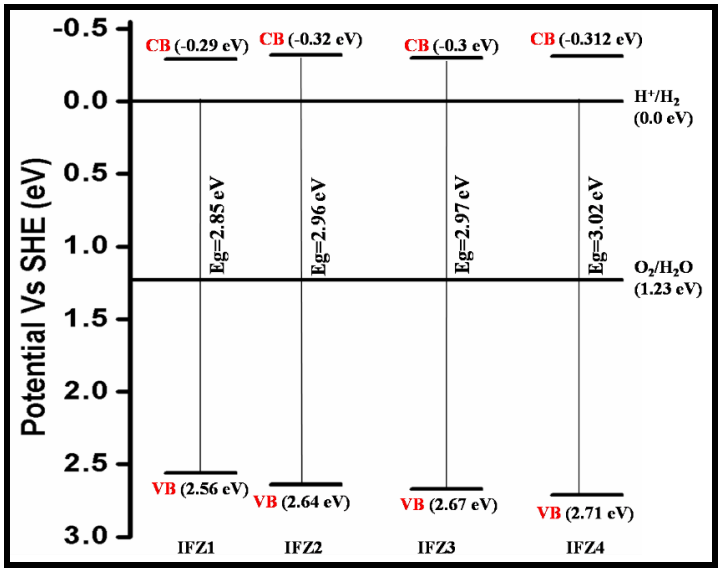

Figure 3.10. Valence band and conduction band positions of IFZ1 to IFZ4.

The synthesized materials were evaluated for their activity for hydrogen generation from water–methanol mixtures under visible light irradiation. For an optimization of conditions, we used 20 mL of water, 5 mL of methanol, and 50 mg of catalyst as a standard under steady-state conditions for irradiation duration of 2 h. On the outset, all four catalysts exhibited very good hydrogen evolution activity with

standardized hydrogen evolution of ~19.5 mmol g^{-1} h^{-1} for all the catalysts. The surface areas for IFZ1–4 were estimated from N_2 adsorption studies and are tabulated in Table3.5. Even though high surface area is usually considered to be ideal for conventional catalysis, in photocatalysis, high crystallinity and consequent reduction in defect sites and surface sites are preferred. Optimization of the methanol volume was also carried out, and an unexpected increase in the hydrogen evolution rate (HER) occurs with 3 mL of methanol (12% v/v methanol in water) as shown in Figure 3.11. But as the methanol concentration increases further, the HER decreases. Stability of the hydrogen evolution was studied under steady-state conditions by following hydrogen evolution rates at different durations (Figure 3.12).

Table3.5. Surface area obtained from N_2 adsorption.

Compound	BET surface area (m^2 g^{-1})
IFZ1	12.06
IFZ2	11.54
IFZ3	11.58
IFZ4	11.77

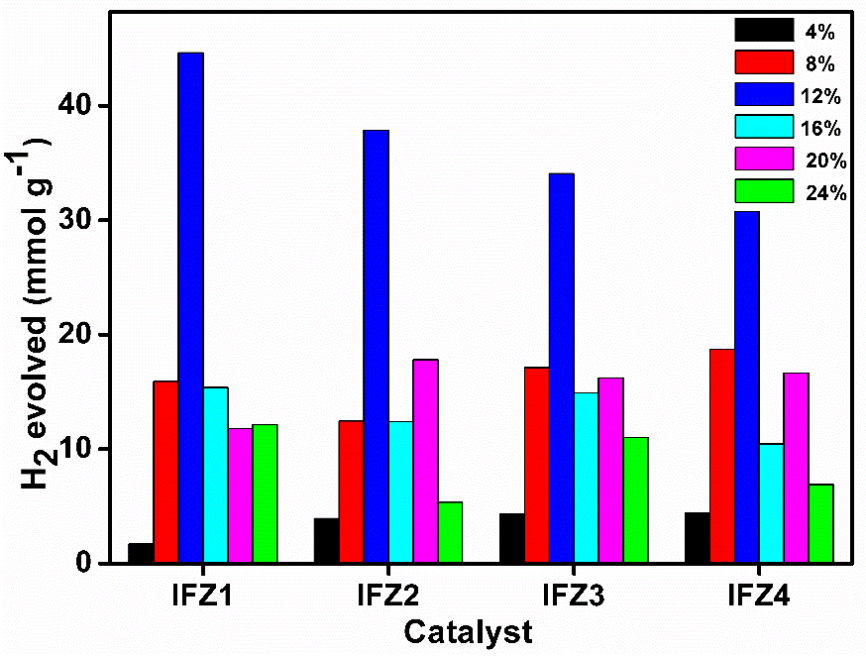

Figure 3.11. Photocatalytic hydrogen evolution with various methanol – water v/v ratios, (black) 4%, (red) 8%, (blue) 12%, (cyan) 16%, (magenta) 20%, and (green) 24% methanol.

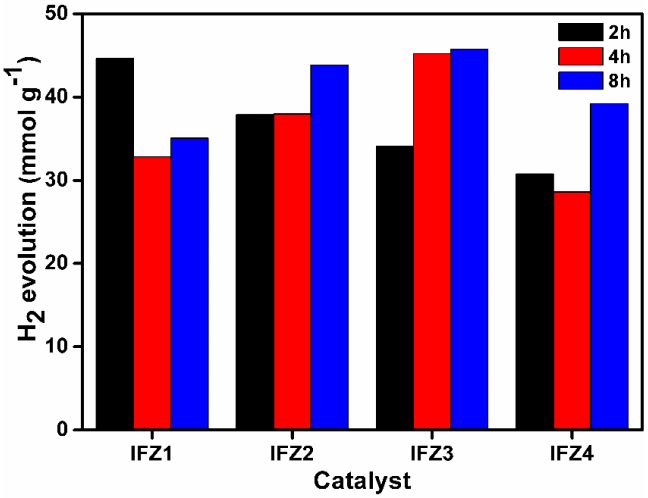

Figure 3.12. Hydrogen evolution at different reaction time intervals (black) 2 h, (red) 4 h, and (blue) 8 h with 12% v/v methanol – water mixture.

Interestingly, the hydrogen evolution attains good yields at 2 h and stays stable until 8 h. The saturation in HER is expected due to the steady-state conditions and head space analysis method we followed. Control experiments without methanol, namely, pure water splitting and with IO_3^-/I^- as hole scavenger, did not yield any hydrogen. This shows that methanol not only acts as hole scavenger, but also as electron enricher and contributes to H_2 generation. It is understood that the hole in valence band abstracts a proton from methanol, which forms a radical and injects an electron into the conduction band. This process is called current doubling and can enhance hydrogen production by assisting water splitting [25]. This was also confirmed by observation of CO and CO_2 in our experiments (Figure 3.13).

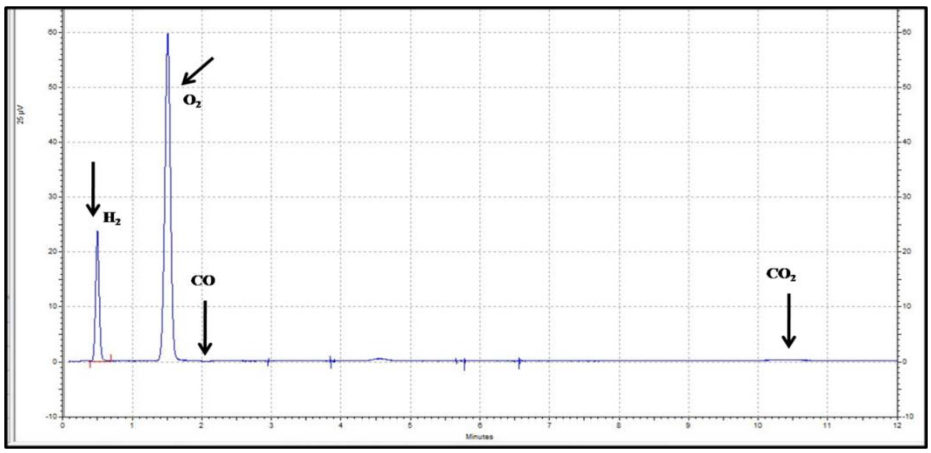

Figure 3.13. Chromatogram of H_2 evolution of IFZ1 under visible light irradiation from 12% methanol 88% v/v methanol- water mixture for 2 h.

Photocatalytic water splitting reactions were also carried out with glycerol as sacrificial agent (Figure 3.14). While comparing the results with that of methanol (Figure 3.12), it can be understood that the hydrogen production was substantially very low with glycerol. The lower amounts of H_2 can be correlated to the higher viscosity of glycerol compared to methanol which results on a lower dispersion of the catalyst in the reaction medium. The reaction was ascertained to be photocatalytic by absence of H_2 production in dark. Other likely products like formaldehyde and formic acid could not be detected in the reaction mixture. This photocatalytic reaction was also found not to proceed without water ruling out any degradation of methanol as the sole reaction responsible for H_2 generation. The contribution of photocatalytic hydrogen evolution of $ZnFe_2O_4$ (synthesized separately), the impurity phase fraction present in IFZ1, IFZ2, and IFZ3 was found to be negligible at an evolution rate of only 3.5 mmol g^{-1} h^{-1}. The crystal structure of the samples remains the same even after the experiments, which is clear from the PXRD (Figure 3.15). After the irradiation the reaction mixture was filtered and ICP-AES analysis was carried out with the filtrate to determine the presence of any leached elements. We could not detect any of the constituent elements in the solution after reaction indicating that the materials are highly stable against photocorrosion or leaching.

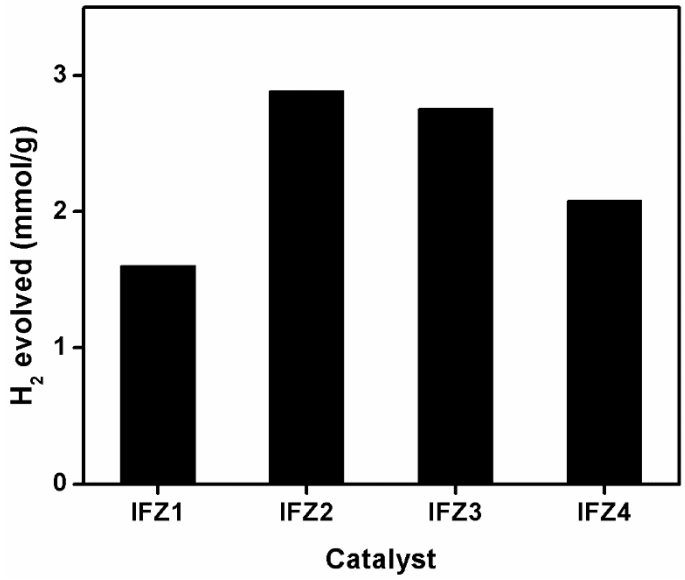

Figure 3.14. Hydrogen evolution for 2 h with 12% v/v glycerol – water mixture under visible light irradiation.

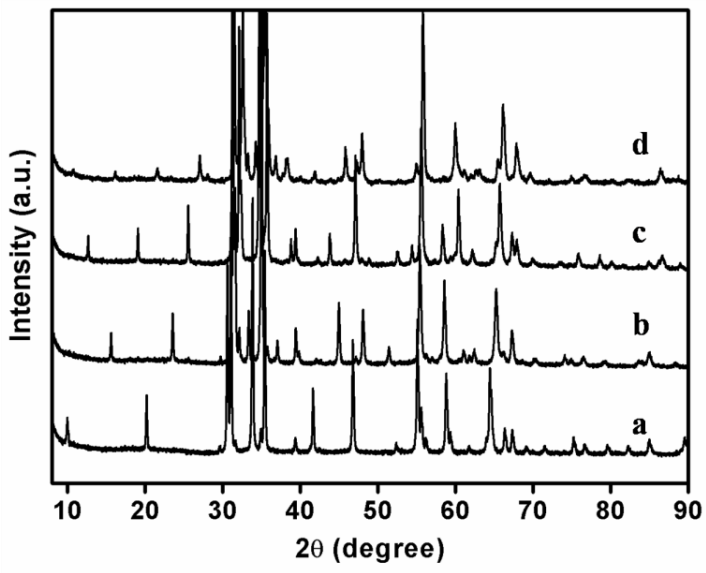

Figure 3.15. PXRD patterns of $InFeO_3(ZnO)_m$ (a) m=1, (b) m=2, (c) m=3, and (d) m=4 after 2 h of H_2 evolution reaction under visible light irradiation from 12% v/v methanol - water mixture.

The higher hydrogen evolution even without the cocatalyst can be attributed directly to the unique structural properties of the compounds. The inherent spatial separation and the low-lying conduction band may be the driving force behind the higher activity. Orbital mixing of Fe 3d orbitals with those of O 2p may also have contributed to a reduction in band gap energy as well as advantageous band positions. To prove the hypothesis, a mixed oxide system $In_2O_3/Fe_2O_3/ZnO$ was used as the catalyst under same conditions. HER was found to be only 2.7 mmol/g indicating a structural contribution to the enhanced activity of these compounds. Comparison of these results with other layered compounds reported in literature also indicates an unprecedented HER from water–methanol mixtures under visible light irradiation from these anisotropic compounds of the series $InFeO_3(ZnO)_m$.

3.4. Conclusions

Structurally anisotropic compounds like $InFeO_3(ZnO)_m$ are found to be highly active in H_2 generation from water– methanol mixtures. Structural studies in analogous compounds in the series like $InGaO_3(ZnO)_m$ reveal a layered structure type with InO_6 octahedral layers sandwiching B/ZnO_n polyhedral layers. Computational studies suggest that the InO_6 octahedral layers facilitate fast electron conduction and charge generation

occurs in the sandwich layer. EXAFS studies indicate that Zn exists as trigonal bipyramids in IFZ1 and IFZ2 and tetracoordinated in IFZ3 and IFZ4 whereas Fe is in pentacoordination in all the four compounds. This unique structural feature helps in inherent spatial separation of charge generation sites and electron conduction pathways minimizing charge recombination. Band gap energies observed from UV–vis absorbance spectroscopy indicate visible light absorbance. The presence of Fe largely contributes to the visible light absorbance. Flat band potentials are calculated from Mulliken electronegativities, and they show appropriately placed conduction band to enable H_2 evolution. EXAFS studies indicate a possible orbital mixing of Fe 3d and O 2p assisting in Fe contribution to the conduction band and lowering of the band gap conducive for visible light catalytic activity. Methanol in the system acts as hole scavenger as well as facilitates current doubling enhancing H_2 evolution rates. Most of the active catalysts reported are supported noble metal catalysts or use $AgNO_3$ as scavenger. The $InFeO_3(ZnO)_m$ materials are active without employing any cocatalyst, which is also advantageous. Moreover, these compositions are highly conducive for further band gap engineering by isotypical substitution. The catalytic sites also can be varied in this manner, and further insights into the mechanism of H_2 evolution and its dependence on various structural and compositional aspects will pave the way for novel water-splitting catalysts.

References

1. Kudo, A.; Miseki, Y. *Chem. Soc. Rev.* **2009**, *38*, 253.

2. Reber, J. F.; Meier, K. *J. Phys. Chem.* **1984**, *88*, 59033.

3. Ming, W.; Wanzhen, G.; Wenzhao, L.; Xian wet, Z.; Fudong, W.; Shiting, Z. *Stud. Surf. Sci. Catal.* **1995**, *92*, 257.

4. Hara, M.; Hitoki, G.; Takata, T.; N. Kondo, J.; Kobayashi, H.; Domen, K. *Catal. Today* **2003,** *78*, 555

5. Sato, J.; Saito, N.; Yamada, Y.; Maeda, K.; Takata, T.; Kondo, J. N.; Hara, M.; Kobayashi, H.; Domen, K.; Inoue, Y. *J. Am. Chem. Soc*. **2005**, *127*, 4150

6. Kasahara, A.; Nukumizu, K.; Hitoki, G.; Takata, T.; Kondo, J. N.; Hara, M.; Kobayashi H.;

Domen, K. *J. Phys. Chem. A* **2002**, *106*, 6750

7. Shchukin, D. G.; Schattka, H. J.; Antonietti, M.; Caruso, R. A. *J. Phys. Chem. B*, **2003**, *107,* 952.

8. Li, D.; Haneda, H. *J. Photoch. Photobio. A* **2003**, *160*, 203.

9. Seabold, J. A.; Choi, K. S. *J. Am. Chem. Soc*., **2012**, *134*, 2186

10. Niu, M.; Huang, F.; Cui, L.; Huang, P.; Yu, Y.; Wang, Y. *ACS Nano* **2010**, 4, 681

11. Kimizuka, N.; Mohri, T.; Matsui, Y. *J. Solid State Chem.***1988**, *74*, 98.

12. Zhao, L.; Pei, Y.; Liu, Y.; Berardan, D.; Dragoe, N. *J. Am. Ceram. Soc.* **2011**, *94*, 1664.

13. Zhang, C.; Pei, Y.; Zhao, L.; Berardan, D.; Dragoe, N.; Gong, S.; Guo, H. *J. Eur. Ceram. Soc.* **2014**, *34*, 63.

14. Isobe, M.; Kimizuka, N.; Nakamura, M.; Mohri, T. *ActaCrystallogr. Sect. C: Cryst. Struct. Commun.* **1994**, *50*, 332.

15. Li, C.; Bando, Y.; Nakamura, M.; Onoda, M.; Kimizuka, N. *J. Solid State Chem.* **1998**, *139*, 347.

16. Toby, B. J. *Appl. Crystallogr.* **2001**, *34*, 210.

17. Keller, I.; Assenmacher, W.; Schnakenburg, G.; Mader, W.*Z. Anorg. Allg. Chem.* **2009**, *635*, 2065.

18. Orita, M.; Tanji, H.; Mizuno, M.; Adachi, H.; Tanaka, I. *Phys. Rev. B* **2000**, *61*, 1811.

19. Zhao, J.; Huggins, F. E.; Feng, Z.; Huffman, G. P. *Clays Clay Miner.* **1994**, *42*, 737.

20. Westre, T. E.; Kennepohl, P.; Dewitt, J. G.; Hedman, B.; Hodgson, K. O.; Solomon, E. I. *J. Am. Chem. Soc.* **1997**, *119*, 6297.

21. Abreu, A. L.; Guimarães, I. R.; Anastáciol, A. S.; Guerreiro, M. C. *J. Mol. Catal. A Chem.* **2012**, *356*, 128.

22. Murphy, A. B. *Sol. Energy Mater. Sol. Cells* **2007**, *91*, 1326.

23. Jiang, P.; Li, J.; Sleight, A. W.; Subramanian, M. A. *Inorg. Chem.* **2011**, 50, 5858.

24. Kim, Y. F.; Atherton, S. J.; Brigham, E. S.; Mallouk, T. E. *J. Phys. Chem.* **1993**, *97*,

11802.

25. Hykaway, N.; Sears, W. M.; Morisaki, H.; Morrison, S. R. *J. Phys. Chem.* **1986**, *90*, 6663.

Chapter 4

Cobalt based layered hydroxides: Modifications and activity towards photocatalytic water splitting

4. 1. Introduction

As mentioned in Chapter 1, section 1.4.1, layered hydroxides have fascinating applications in various fields including catalysis, as electrodes etc. [1-2]. A large number of anionic species can be allocated between the interlayers of layered hydroxides and this structural flexibility can generate a variety of hybrid materials with different properties [3-4].

Prof. D. G. Nocera and coworkers have reported in their seminal work that Co_4O_4 core of a cobalt-oxocubane, covalently attached to Re(I) photosensitisers possesses a superior oxygen evolution capability [5]. Recently G. Mittioli *et al.* reported the molecular mechanism for oxygen evolution from water with an inorganic cobalt based catalyst film. The compound consists of several CoO_6 octahedra assembled in incomplete and complete cubane units [6]. G. S. Hutchings *et al*. studied the oxygen evolution activity of non-supported ultra-small cobalt oxide nanocubanes [7]. $Co(OH)_2$ also possesses similar Co-O frame work as that of cobalt cubanes within the structure. Two polymorphs of $Co(OH)_2$ are known, *viz*., α-$Co(OH)_2$ and β-$Co(OH)_2$. These compounds form a class of lamellar compounds made up of brucitelike layers. Co^{2+} occupies the centers of edge sharing octahedra, whose vertexes contain hydroxide ions that connect to form infinite 2D sheets. In α-$Co(OH)_2$, the layers are ionic and has an interlayer region containing charge compensating anions and solvation molecules similar to hydrotalcite structures whereas, the brucite like layers of β-$Co(OH)_2$ are not charged and does not have any interlayer anions [8-9]. This type of edge shared octahedral layers are understood to be highly conducive for electron conduction [10] as seen in the case of anisotropic layered compounds like $InMO_3(ZnO)_m$ mentioned in previous chapters.

As an extension to the oxygen evolution studies on cobalt based systems, it is relevant to add the hydrogen evolution activity also in the system by creating an active site. NiO is a well known catalyst in many reactions like hydrogenation, oxidative addition, various organic coupling reactions etc. and most importantly, is known to act as a cocatalyst in H_2 evolution reactions [11-14]. Hence it is worthwhile to dope Ni in $Co(OH)_2$

thereby generating a new H_2 evolution site in the layered structure with the added advantage of catalytic site separation due to the interlayer region. Nickel hydroxide also crystallizes in two polymorphs isostructural with $Co(OH)_2$ with the same edge shared octahedral layer motifs and hence a structural compatibility can be expected [15]. We also considered Zn as a relevant dopant since ZnO has interesting photophysical properties [16] and may impart these to $Co(OH)_2$ parent compounds in addition to providing catalytic sites for H_2 evolution.

In this chapter, the photocatalytic activity of layered hydroxides of cobalt is detailed along with the attempts at incorporation of new catalytic sites via Ni and Zn doping. Major effort is made to create a new catalytic site for hydrogen evolution in an existing cationic environment. α-Cobalt hydroxide exhibits more interesting interlayer chemistry and the structure is more promising for further modifications [17] and hence we can expect it to have better catalytic site separation than its β counterpart. So in the current study, we have given more space to alpha form and its modifications.

4.2. Experimental

4.2.1. Synthesis of α-$Co(OH)_2$

The synthesis was performed in a round bottom flask under ambient atmosphere. In a typical procedure, $CoCl_2.6H_2O$ (0.4758 g), NaCl (0.5845 g) and Hexamethyl tetraamine (HMT) (1.6822 g) were dissolved in 200 mL of a 9:1 mixture of millipore ultrapure and ethanol to give the final concentrations of 10, 50, and 60 mM, respectively. The reaction solution was then heated at about 90 °C under magnetic stirring. After being heated for about 1 h, a suspension containing green particles resulted. The solid product was filtered and washed with deionized water and anhydrous ethanol several times, and finally air-dried at room temperature [9]. The yield of α-$Co(OH)_2$ was ~30%.

Initially, the colour of the solution was pink and after about half an hour, the solution turned to bluish colour and finally suspension containing green particles was obtained.

4.2.2. Synthesis of β-$Co(OH)_2$

The synthesis procedure was similar as described in section 4.2.1, except no NaCl was added. Also the concentration of $CoCl_2$. $6H_2O$ was decreased to 5mM instead of 10 mM. $CoCl_2.6H_2O$ (0.2379 g) and HMT (1.6822 g) were dissolved in 200 mL of a 9:1 mixture of millipore ultrapure water and ethanol to give the final concentrations of 5 and 60 mM, respectively. The reaction solution was then heated at 90 °C under magnetic stirring. After being heated for about 1 h, a suspension containing pink particles resulted. The solid product was filtered and washed several times with deionized water and anhydrous ethanol, and finally air-dried at room temperature [9]. The yield was found to be ~ 35%. The colour change was same as that observed in alpha, however, the green suspension formed underwent turbostatic conversion to pink suspension.

4.2.3. Synthesis of $Ni_xCo_{1-x}(OH)_2$: An attempt to dope nickel into $Co(OH)_2$ lattice.

$CoCl_2.6H_2O$, NaCl, HMT, and $Ni(NO_3)_2.6H_2O$ were dissolved in 200 mL of a 9:1 mixture of deionized water and ethanol in a round bottom flask. The concentration of NaCl and HMT were fixed as 50 mM and 60 mM respectively in every reaction. The concentrations of $CoCl_2.6H_2O$ and $Ni(NO_3)_2.6H_2O$ were varied to get a total of 10 mM of metal concentration in solution. The reaction solution was then heated at 90 °C under magnetic stirring. After being heated for about 1 h, the solid product thus formed was filtered, washed with deionized water and anhydrous ethanol several times, and finally air dried at room temperature. Five compositions were prepared with x = 0.1, 0.2, 0.3, 0.4 and 0.5 mole%. The average yields were ~30%.

4.2.4. Incorporation of zinc

Here we followed two different procedures. The first one is post synthesis method in which α-$Co(OH)_2$ and β-$Co(OH)_2$ were mixed with $Zn(NO_3)_2.6H_2O$and then subjected to a heat treatment at 120 °C for 1 h under N_2 atmosphere in a tubular furnace to decompose zinc nitrate, as the decomposition temperature of zinc nitrate is 120-130 °C. Heating rate was 2 °C min^{-1}. The second procedure is *in situ* synthesis route, where zinc nitrate is

simultaneously added along with the precursors of α-$Co(OH)_2$ and β-$Co(OH)_2$ during the synthesis.

4.2.4a. Incorporation of zinc in β-$Co(OH)_2$ by post synthetic method

1:1 mole ratio of β-$Co(OH)_2$ (0.0304 g) and $Zn(NO_3)_2.6H_2O$ (0.0973 g) were mixed thoroughly by means of mortar and pestle. First, zinc nitrate was dissolved in minimum volume of water and then the constituents were homogenously mixed. The mixture was then heated at 120 °C under N_2 atmosphere in a tubular furnace for 1 h to decompose zinc nitrate. Heating rate was 2 °C min^{-1}. A pink coloured product was formed. The product is named as **bPCoZn** to indicate **beta-post-synthesis-CoZn hydroxide**.

4.2.4b. Incorporation of zinc in β-$Co(OH)_2$ by *in situ* synthetic method

$Zn(NO_3)_2.6H_2O$ (0.5949 g), $CoCl_2.6H_2O$ (0.4758 g), and HMT were dissolved in 200 mL of a 9:1 mixture of millipore water and ethanol to give the final concentrations of 10, 10 and 60 mM, respectively. The reaction solution was then heated at 90 °C with magnetic stirring. After heating for about 1 h, the solid product formed was filtered and washed with deionized water and anhydrous ethanol several times, and finally air-dried at room temperature. The sample code used for the product obtained is **bISCoZn** indicating **beta-insitu-synthesis-CoZn hydroxide.**

4.2.4c. Incorporation of zinc in α-$Co(OH)_2$ by post synthetic method

1:1 mole ratio of α-$Co(OH)_2$ (0.2666 g) and $Zn(NO_3)_2.6H_2O$ (0.8532 g) were mixed thoroughly by means of mortar and pestle. Zinc nitrate was dissolved in minimum volume of water before the constituents were homogenously mixed. The mixture was then heated to 120 °C in N_2 atmosphere in a tubular furnace for one hour to decompose zinc nitrate. Heating rate was 2 °C min^{-1}. A pink colored product was formed and sample code for the compound is **aPCoZn** to indicate **alpha-posts-ynthesis-CoZn hydroxide.**

Further, the precursor mixture was heated at 50 °C and 100 °C for 1 h and the residues were analyzed to study the structural transformations. α-$Co(OH)_2$ was also treated with zinc acetate to check the effect of different zinc precursors for the synthesis of

aPCoZn. The reaction of α-$Co(OH)_2$ with sodium nitrate as well as calcium nitrate were also carried out to observe the effect of various nitrate precursors.

4.2.4d. Incorporation of nickel and zinc in α-$Co(OH)_2$ by *in situ* synthetic method

$Zn(NO_3)_2.6H_2O$ (0.5949 g), $CoCl_2.6H_2O$ (0.4758 g), NaCl (0.5845 g) and HMT (1.6822 g) were dissolved in 200 mL of a 9:1 mixture of millipore water and ethanol to give the final concentrations of 10, 10, 50, and 60 mM, respectively. The reaction solution was then heated at about 90 °C under magnetic stirring. After heating for about 1 h, the solid product formed was filtered and washed with deionized water and anhydrous ethanol several times, and finally air-dried at room temperature. The product is named as **aISCoZn** indicating **alpha-insitu-synthesis-CoZn hydroxide**. Also, same synthesis procedure was followed for Co/Ni, ratios of 9:1, 8:2 and 7:3. The products are named as **aISCoZn9**, **aISCoZn8** and **aISCoZn7** respectively, the numbers indicating the Co concentration.

4.2.4e. Incorporation of zinc in $Co_{0.8}Ni_{0.2}(OH)_2$ by post synthetic method

1:1 molar ratios of $Ni_{0.2}Co_{0.8}(OH)_2$ and $Zn(NO_3)_2.6H_2O$ are mixed thoroughly by means of mortar and pestle. Zinc nitrate was dissolved in minimum volume of water and added to $Ni_{0.2}Co_{0.8}(OH)_2$ in a mortar and homogenously mixed. The mixture was then heated to 120 °C in N_2 atmosphere in a tubular furnace for 1 h to decompose zinc nitrate. Heating rate was 2 °C min^{-1}. Finally pink colored product was obtained and the sample code is **aPNiCoZn (alpha-post-synthesis-NiCoZn hydroxide)**.

4.3. Characterization

The details of the instruments and procedures used for PXRD is same as those described in chapter 2. Variable temperature *in situ* XRD experiments were carried out in an Anton-Paar XRK900 reactor under N_2. The XRD patterns in the 2θ range 10-70° and 38-44° were collected with step size of 0.008° and time per step of 52.90 s respectively. UV-vis spectra were recorded using a Cary 5000 UV-vis-NIR spectrophotometer and the measurements were carried out in a quartz cell of 10 mm path length (volume 3.5 mL). Methanol was taken as the reference. The scanning electron micrographs of the samples

were obtained in dual beam scanning electron microscope (FEI company, model Quanta 200 3D) operating at 30 KV. Thermogravimetric analysis was carried out on a METTLER TOLEDO TGA/SDTA851e instrument. The sample was heated under N_2 with a gas flow of 40 ml/min to 500 °C at a rate of 5 °C/min.

4.4. Catalytic testing

The setup and reaction conditions used are explained in 2.3.1c in chapter 2. The photocatalyst powder (10 mg) was dispersed in a reactant solution (25 mL) by a magnetic stirrer in an irradiation cell made of quartz. 20 mL pure water and 5 mL methanol were employed as reactant solutions for water splitting.

4.5. Results and discussion

4.5.1a. α-$Co(OH)_2$ and β-$Co(OH)_2$

Figure 4.1 shows the well indexed PXRD patterns of α and β-$Co(OH)_2$. PXRD pattern of α $Co(OH)_2$ matches very well with that reported by Z. Liu *et. al*. [9] and PXRD pattern of β-$Co(OH)_2$ matches the reported pattern corresponding to JCPDS no: 74-1057 [18]. The patterns have a broad background due to luminescence of Co based compounds normally observed with Cu X-rays. α-$Co(OH)_2$ is characterized by an intense peak at 11.11° due to the (003) plane. Another dominating peak after 20° is due to (006) plane of the hydrotalcite like phase. Taking its green colour into consideration, it can be identified as the α-$Co(OH)_2$. β-$Co(OH)_2$ was distinguished from α-$Co(OH)_2$ by its unique pink colour. The PXRD pattern of β-$Co(OH)_2$ shows a strong diffraction peak at 19.24° by (001) plane of brucite like phase. Other prominent reflections are (100), (011) and (012) at 32.56°, 38.00° and 58.07° respectively. From Table 4.1 it is clear that there is no chlorine present in β-$Co(OH)_2$. This points to the incapability of ion exchange as reported in the literature. α-$Co(OH)_2$ and β-$Co(OH)_2$ are reported to have well separated hexagonal platelets [9]. The SEM images confirmed the morphology as seen in Figure 4.2 and Figure 4.3.

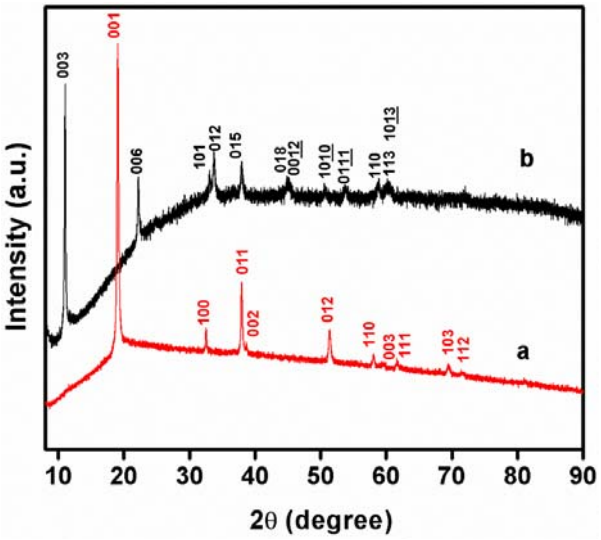

Figure 4.1. PXRD patterns of (red) β-$Co(OH)_2$ and (black) α-$Co(OH)_2$. hkl planes are indicated against the peak.

Table 4.1. Elemental fractions in α-$Co(OH)_2$ and β-$Co(OH)_2$ from EDAX mapping.

Element	Atom% α- $Co(OH)_2$	Atom% β-$Co(OH)_2$
Cobalt	64.13	67.36
Oxygen	27.93	32.64
Chlorine	7.94	-

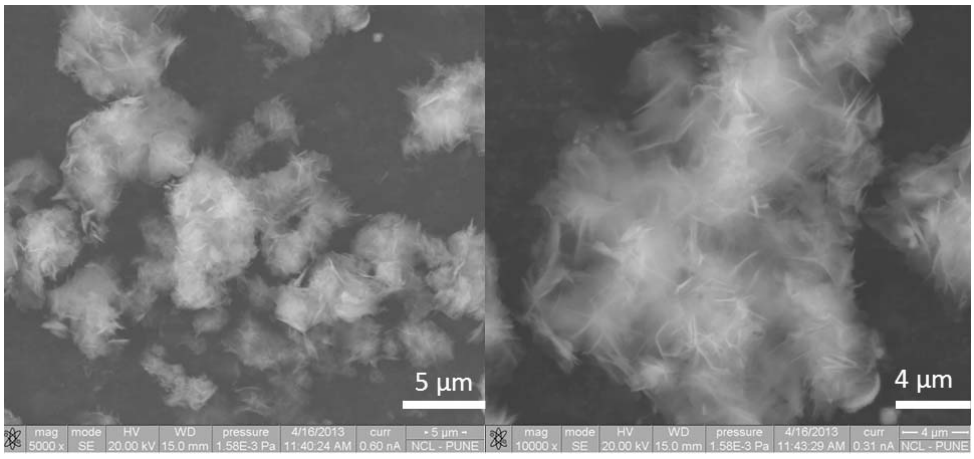

Figure 4.2. SEM images of well separated platelets of α-$Co(OH)_2$.

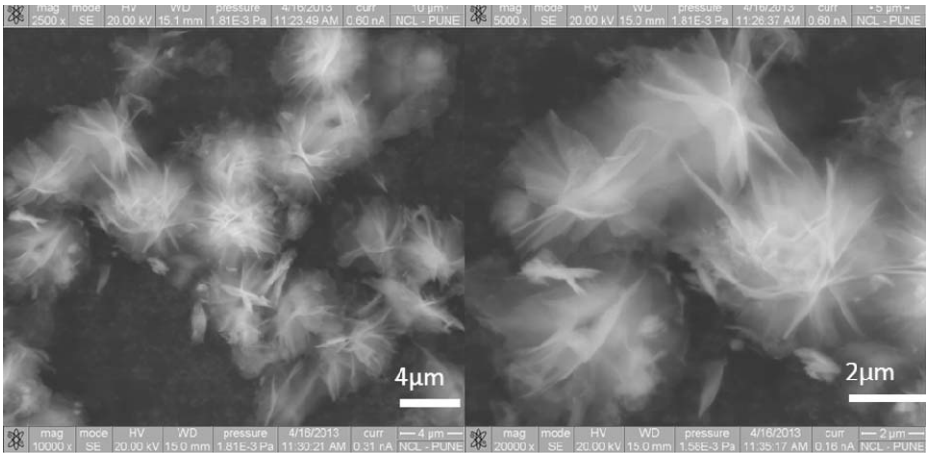

Figure 4.3. SEM images of well separated platelets of β-$Co(OH)_2$.

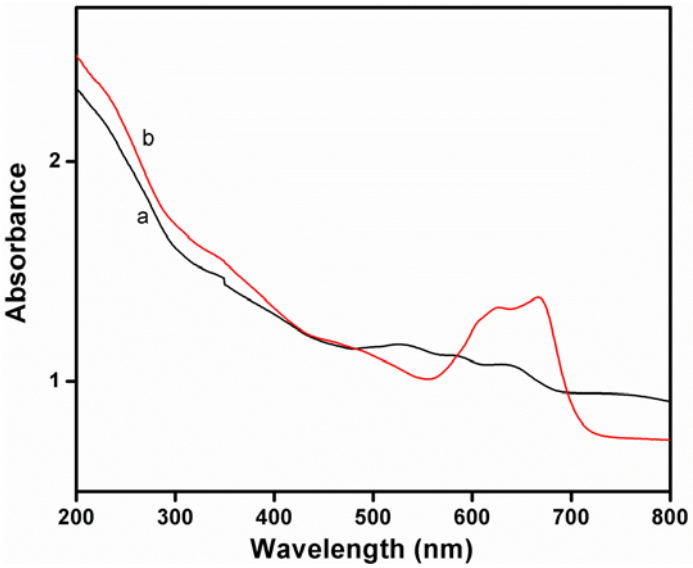

Figure 4.4. UV-vis spectra of (a) β-$Co(OH)_2$ and (b) α-$Co(OH)_2$.

UV-vis absorption spectroscopy analysis was carried out for the sample dispersed in methanol and the results are shown in Figure 4.4. It is observed that α-$Co(OH)_2$ has a strong absorption in the visible region at 675 nm. β-$Co(OH)_2$ has a weak absorbance in the visible region. Since both compounds were capable of visible light absorption, these were tested for photocatalytic hydrogen evolution activity. β-$Co(OH)_2$ was found to be inactive, but α-$Co(OH)_2$ gave ~1 mmol/g of hydrogen in 4 h. In this scenario, α-$Co(OH)_2$ was particularly selected and attempts were made to modify it. The motivation behind the

endeavor is that α-$Co(OH)_2$ has strong visible light absorption feature as well as it has the capability of ion exchange giving us more flexibility in modifying it structurally.

4.5.1b. Ni doping in α-$Co(OH)_2$

Further attempts were made to create a new catalytic site for hydrogen evolution in α-$Co(OH)_2$. A wide variety of cocatalysts are reported to act as catalytic sites for hydrogen evolution, *viz,* NiO. RuO etc. These cocatalyst kinetically favor water reduction. Especially Ni being an efficient cocatalysts, it is expected that incorporation of Ni can create active reduction sites in α-$Co(OH)_2$. Hence a systematic doping with progressively increasing amounts of Ni in the Co site was carried out by a simple coprecipiation method.

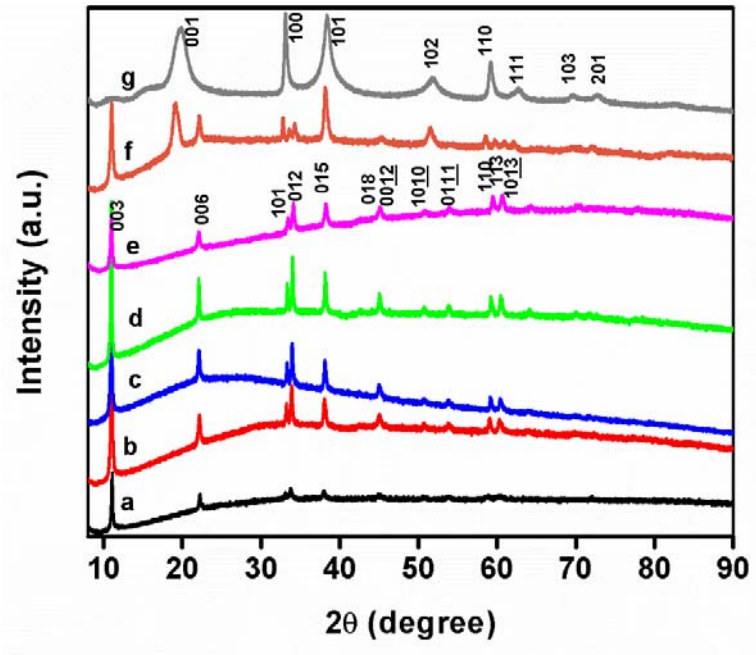

Figure 4.5. PXRD patterns of (a) α-$Co(OH)_2$,(b) $Ni_{0.1}Co_{0.9}(OH)_2$, (c) $Ni_{0.2}Co_{0.8}(OH)_2$, (d) $Ni_{0.3}Co_{0.7}(OH)_2$, (e) $Ni_{0.4}Co_{0.6}(OH)_2$ and (f) $Ni_{0.5}Co_{0.5}(OH)_2$, (g) $Ni(OH)_2$.

The phase formation of the synthesized nickel cobalt hydroxides, $Ni_xCo_{(1-x)}(OH)_2$ [x-0.1 to 0.5] was evaluated by PXRD analysis. Figure 4.5 presents the well indexed PXRD patterns of various cobalt nickel hydroxides along with the pattern of a reference $Ni(OH)_2$, which matches that of the reported compound (JCPDS card No. 14-0117) [19]. However,

the pure α-$Ni(OH)_2$ is very unstable in water and alkali and quickly transforms to the β-phase [20]. Consequent to this, in Figure 4.5, we can see the PXRD pattern of β-$Ni(OH)_2$. In literature, it is reported that stable α-$Ni(OH)_2$ can be obtained by substituting nickel ion in the nickel hydroxide lattice by other metal ions such as Al, Co, Fe, Mn and Zn etc [21-25]. It is also evident from Figure 4.5 that nickel ion can reside in the α-$Co(OH)_2$ lattice up to a composition of $Ni_{0.4}Co_{0.6}(OH)_2$. The broad features of PXRD pattern of $Ni(OH)_2$ is related to the particle size [26]. The PXRD results of various compositions of nickel cobalt hydroxide were comparable with parent α-$Co(OH)_2$ except the composition at $Ni_{0.5}Co_{0.5}(OH)_2$. At $Ni_{0.5}Co_{0.5}(OH)_2$ composition, the peak at 19.30° for nickel hydroxide is also prominent, which implies that Ni forms $Ni(OH)_2$ phase at a composition of $Co_{0.5}Ni_{0.5}(OH)_2$. EDAX analysis indicates that the composition is more or less same as that of the intended compositions (Table 4.2). For the sake of clarity, we have followed the nomenclature based on the intended compositions.

Table 4.2. Elemental fractions of Co and Ni in $Ni_xCo_{(1-x)}(OH)_2$ [x - 0.1 to 0.5] from EDAX analysis.

Indended Compound	Cobalt Atom%	Nickel Atom%	Composition obtained from EDAX easurement
$Co_{0.9}Ni_{0.1}(OH)_2$	57.44	11.52	$Co_{0.83}Ni_{0.17}(OH)_2$
$Co_{0.8}Ni_{0.2}(OH)_2$	52.84	17.5	$Co_{0.75}Ni_{0.25}(OH)_2$
$Co_{0.7}Ni_{0.3}(OH)_2$	45.32	24.87	$Co_{0.64}Ni_{0.36}(OH)_2$
$Co_{0.6}Ni_{0.4}(OH)_2$	39.7	33.5	$Co_{0.54}Ni_{0.46}(OH)_2$

Figure 4.6 shows the absorbance of the series of nickel cobalt hydroxides $Ni_xCo_{(1-x)}(OH)_2$ [x- 0.1 to 0.5]. These compounds have a strong absorption in the UV region (sharp peak at 250 nm) and weak absorption peak in visible region (broad peaks from 600-700 nm). UV light and visible light absorptions can act advantageously in utilizing these materials in solar photocatalytic water splitting. The absorption features of pure $Ni(OH)_2$ and Ni doped α-$Co(OH)_2$ were entirely different. The visible light absorption feature of α-$Co(OH)_2$ was retained in $Ni_xCo_{(1-x)}(OH)_2$ [x- 0.1 to 0.5] suggesting that Ni doping did not affect the visible light absorption capability of α-$Co(OH)_2$. Pure $Ni(OH)_2$ has a broad far

visible absorption from 700-800 nm and UV absorption at 320-450 nm [26]. The absorption characteristics of pure $Ni(OH)_2$, which is in β form, are comparable to that of β-$Co(OH)_2$ which has low visible light absorbance. The visible light absorption features of $Ni_xCo_{(1-x)}(OH)_2$ [x- 0.1 to 0.5] can be correlated to the absorption characteristics of α-$Co(OH)_2$ as the series of compound has a similar structure as that of α-$Co(OH)_2$.

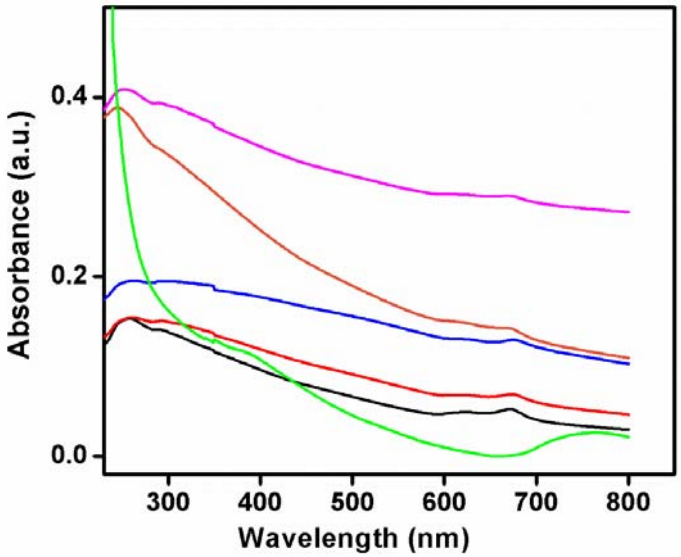

Figure 4.6. UV-vis spectra of $Ni_{0.1}Co_{0.9}(OH)_2$ (black), $Ni_{0.2}Co_{0.8}(OH)_2$ (red), $Ni_{0.3}Co_{0.7}(OH)_2$ (blue), $Ni_{0.4}Co_{0.6}(OH)_2$ (orange), $Ni_{0.5}Co_{0.5}(OH)_2$ (purple) and $Ni(OH)_2$ (green).

$Ni_xCo_{(1-x)}(OH)_2$ [x- 0.1 to 0.5] compounds were tested for their photocatalytic hydrogen evolution activities under visible light irradiation. The results obtained fromthese experiments are graphically represented in Figure 4.7. Interestingly all the compounds show exceptionally high hydrogen evolution activity under visible light irradiation. The hydrogen evolution increases more or less proportionately as duration of irradiation increases. It is worthwhile to note that pure $Ni(OH)_2$ could generate 17.6 mmol/g of H_2 and the rate of H_2 evolution for Ni doped compounds is more or less similar to $Ni(OH)_2$ except $Ni_{0.1}Co_{0.9}(OH)_2$. This may be attributed to the synergestic effect of Co and Ni at low concentrations of the latter. After the optimal concentration, the catalytic effect of Ni predominates. The negligible hydrogen evolution in α-$Co(OH)_2$ is attributed to the lack of reaction site within the structure. Hence, it is clear from the above result that doping

with Ni in appropriate concentrations makes α-$Co(OH)_2$ a potential candidate for photocatalytic water splitting which is unexplored in the existing literature.

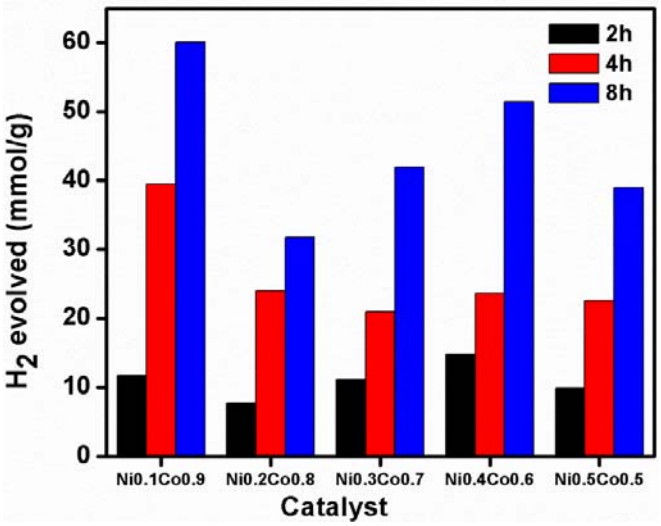

Figure 4.7. H_2 evolution in $Ni_{0.1}Co_{0.9}(OH)_2$, $Ni_{0.2}Co_{0.8}(OH)_2$, $Ni_{0.3}Co_{0.7}(OH)_2$, $Ni_{0.4}Co_{0.6}(OH)_2$ and $Ni_{0.5}Co_{0.5}(OH)_2$ from 20% v/v methanol-water mixture under visible irradiation for 4 h

Even if a catalytic site separation is achieved in this material, the presence of methanol in the reaction medium could not be avoided. This indicates that the reaction mechanism involves the current doubling phenomenon which enriches the electron density for water reduction [27]. The higher activity can also be correlated to the role of cobalt based compounds in oxidation reaction [28].

4.5.2. Zinc loaded cobalt hydroxides

Further we have investigated the role of zinc in cobalt hydroxides. As ZnO is an excellent photocatalyst with a favorable band gap, it is expected that zinc along with cobalt hydroxide can act as a good photocatalyst by contributing to excellent catalytic site separation. As described in section 4.2.4, we followed two different strategies for the zinc incorporation on both α and β-$Co(OH)_2$. However, unlike in case of Ni, 50% Zn loading led to new products similar to layered hydroxyl nitrates and hydrates even at low temperatures and α and β-$Co(OH)_2$ resulted in different products. This shows that parent layered hydroxide structure is crucial in determining the product structure in case of zinc

incorporation. Zinc based layered hydroxyl nitrates are well known in literature and extensive studies are carried out on zinc hydroxide nitrates as their anion intercalation is a vast area of research. The widely studied systems are $Zn_5(OH)_8(NO_3)_2{\cdot}2H_2O$, $Zn(OH)(NO_3).H_2O$ and $Zn_3(OH)_4(NO_3)_2$ [29-31]. P. Li *et al.* studied the use of $Zn_5(OH)_8(NO_3)_2{\cdot}2H_2O$ as long term foliar fertilizer by utilizing its aqueous stability and capability of zinc ion release [29]. The most exciting feature regarding zinc hydroxide nitrates are related to low temperature synthesis and phase transformations. Apart from these known phases, zinc incorporation in layered cobalt hydroxides resulted in interesting new structures also.

4.5.2a. Zinc incorporation in β-$Co(OH)_2$

4.5.2a.1. Post synthesis route

Figure 4.8 shows a comparison of PXRD patterns of **bPCoZn** and β-$Co(OH)_2$. Post synthesis led to yet another layered compound isostructural with $Zn_3(OH)_4(NO_3)_2$ (JCPDS No. 70-1361), which also belongs to monoclinic class with a=7.0380Å; b=9.6580Å; c=11.1820 Å and β=100.96° [31]. The structure of the compound is shown in Figure 4.9. The unit cell has two layers of edge shared octahedra of ZnO_6 and the interlayer is occupied by NO_3^- and H^+ ions.

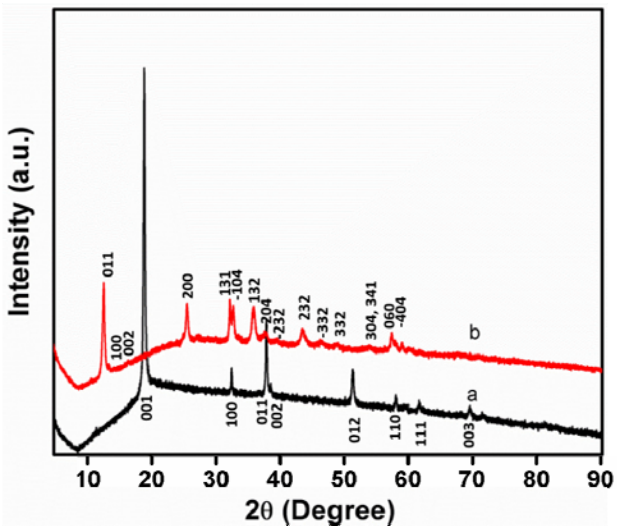

Figure 4.8. PXRD patterns of (a) β-$Co(OH)_2$ and (b) **bPCoZn.**

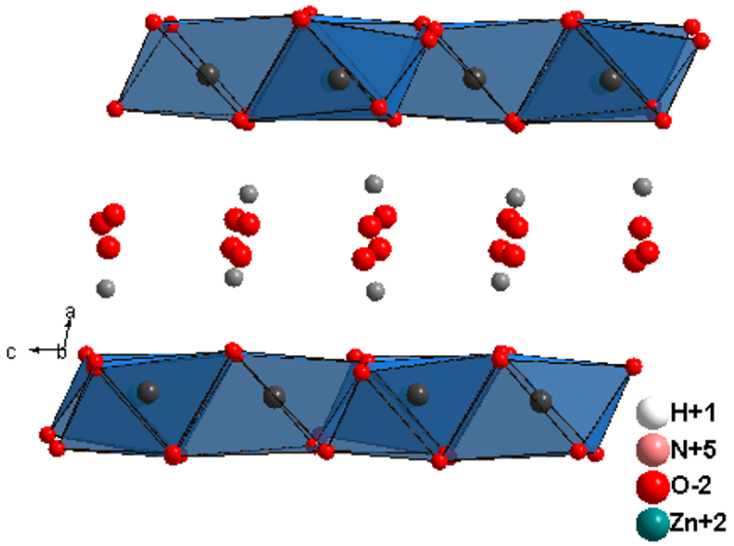

Figure 4.9. Crystal structure of $Zn_3(OH)_4(NO3)_2$ which has layers of edge shared ZnO_6 octahedra and NO_3^- ions are located in between the layers.

The well separated morphology in β-$Co(OH)_2$ was lost in **bPCoZn** which is clear from the SEM image (Figure 4.10). Elemental analysis shows the presence of Co in the system which indicates the formation of Co doped $Zn_3(OH)_4(NO_3)_2$. In literature it is reported that similar hydroxide nitrates can release the octahedral ions in solution and a similar effect cannot be ruled out here [29]. So it can be anticipated that Co^{2+} and Zn^{2+} can interchange and there can be a reorientation of intercalated anions to form a stable mixed metal hydroxide nitrate phase.

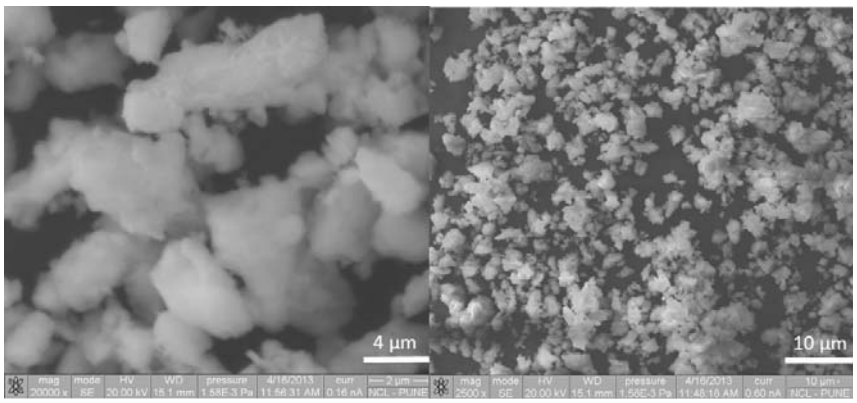

Figure 4.10. SEM images of **bPCoZn** shows destruction of separated hexagonal platelets in β-$Co(OH)_2$.

Table 4.3. Elemental fractions of **bPCoZn** from EDAX mapping.

Element	Atom% **bPCoZn**
Cobalt	28.43
Zinc	32.73
Oxygen	32.19
Nitrogen	6.66

Further efforts were taken to understand the effect of zinc on the building of **bPCoZn** structure. When zinc acetate was used as the precursor, no crystalline product could be obtained. Sodium nitrate and calcium nitrate were loaded in β-$Co(OH)_2$ to find the effect of other nitrate salts. In this case also the products were sticky and no crystalline product was formed. Hence the phase formation observed can be unambigously attributed to zinc incorporation.

4.5.2a.2. *In situ* synthesis route

When *in situ* synthesis route is followed for β-$Co(OH)_2$, the product (**bISCoZn**) has more of ZnO phase with a small amount of spinel of Co and Zn. It is clearly visible in the PXRD pattern of **bISCoZn** as shown in Figure 4.11. Since **bISCoZn** did not yield any layered structures conducive for catalytic site separation, further experiments were restricted only to zinc incorporation in α-$Co(OH)_2$.

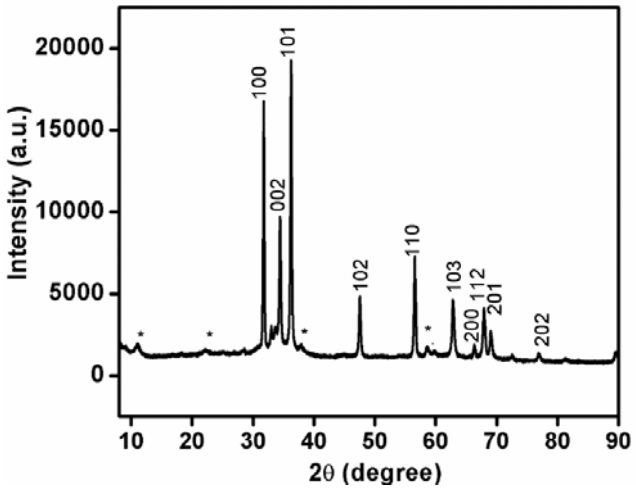

Figure 4.11. PXRD pattern of **bISCoZn** shows ZnO is the major phase. Reflections corresponding to spinel phase are marked as *.

4.5.2b. Zinc incorporation in α-$Co(OH)_2$

4.5.2b.1. Post synthesis route

PXRD patterns of **aPCoZn** by post synthesis route is given in Figure 4.12. **aPCoZn** has a phase isostructural with $CoNO_3OH{\cdot}H_2O$ which belongs to monoclinic structure (JCPDS Code: 48-0091) with a=17.7570 Å, b=3.1420 Å, c=14.1880 Å and β= 113.55° respectively [32]. No impurity phases corresponding to either Co or Zn were observed. In $CoNO_3OH{\cdot}H_2O$, each cobalt atom is coordinated to oxygens of three hydroxyl ions, two water molecules and one oxygen atom belonging to a nitrate group, thus making an octahedral environment as shown in the Figure 4.13. Also EDAX analysis shows atom% of zinc and presence of Cl in the interlayer. **aPCoZn** has a different morphology compared to α-$Co(OH)_2$. Figure 4.14 shows that the individual flakes in α-$Co(OH)_2$ got agglomerated in **aPCoZn**.

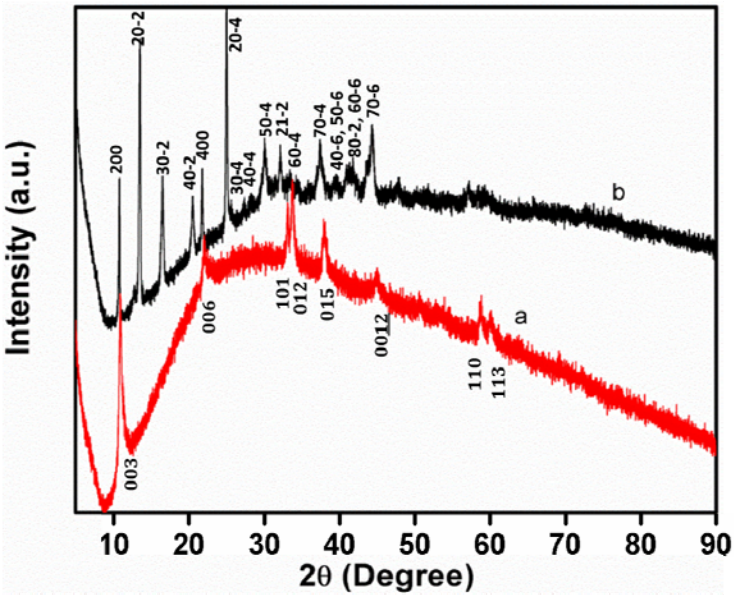

Figure 4.12. PXRD patterns of (a) pure α-$Co(OH)_2$ and (b) **aPCoZn.**

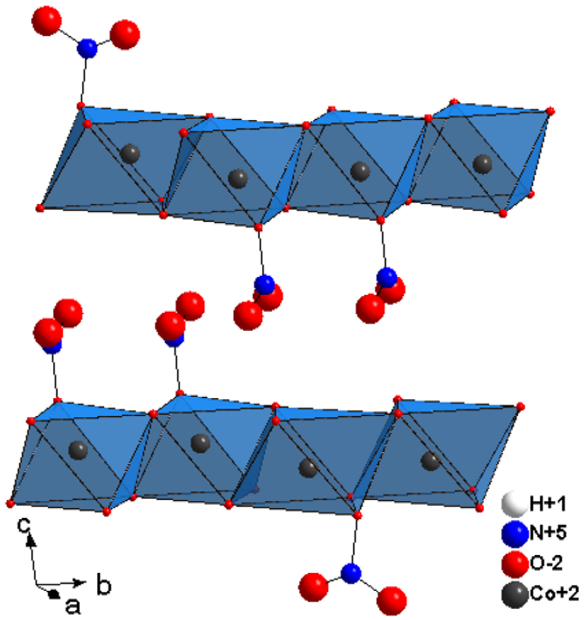

Figure 4.13. Crystal structure of $CoNO_3OH.H_2O$ which forms edge shared octahedra of CoO_6.

Table 4.4. Elemental fractions of **aPCoZn** from EDAX mapping

Element	Atom% in **aPCoZn**
Cobalt	24.62
Zinc	24.84
Oxygen	39.24
Nitrogen	8.32
Chlorine	2.99

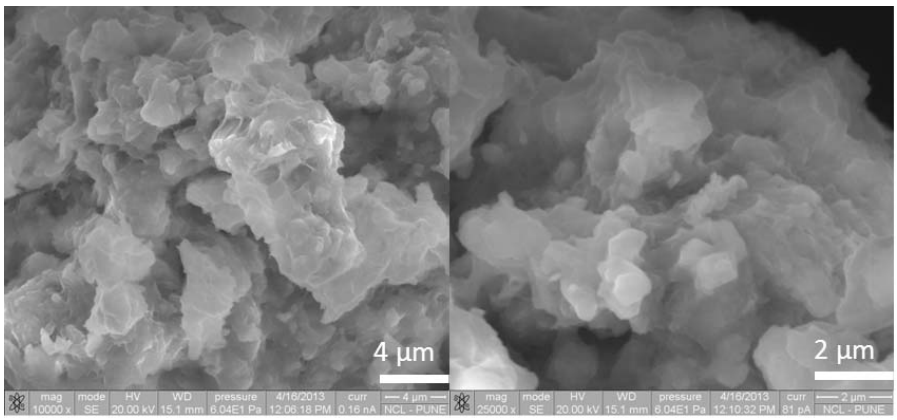

Figure 4.14. SEM images of **aPCoZn**.

The compound was heated at higher temperatures up to 400 °C. The PXRD patterns of the heated samples contained peaks corresponding to individual ZnO as well ZnCo spinel phases. This points to the presence of zinc in **aPCoZn** and it can be inferred that zinc is incorporated in **aPCoZn.** In order to find the mechanism of zinc incorporation by post synthesis method, the precursors for **aPCoZn** (α-$Co(OH)_2$ and $Zn(NO_3)_2.6H_2O$) were heated at 50 °C and 100 °C and PXRD analysis of these samples was done (Figure 4.15). The precursor mixture at room temperature was also analyzed by PXRD.

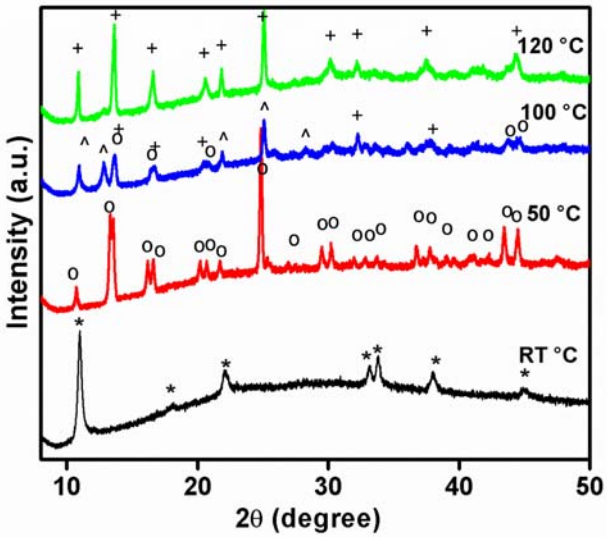

Figure 4.15. PXRD patterns of precursors of **aPCoZn,** (α-$Co(OH)_2$ and $Zn(NO_3)_2.6H_2O$) at room temperature and after heating for 1 h at 50 °C, 100 °C and 120 °C. Various phases are indicated; ∗: α-$Co(OH)_2$, o: isostructural $CoNO_3OH{\cdot}H_2O$, ^: $Zn_3(OH)_4(NO_3)_2$ and +: aISCoZn.

From the Figure 4.15, it is clear that at room temperature there is no phase transformation in α-$Co(OH)_2$ on addition of $Zn(NO_3)_2.6H_2O$. We can clearly see the peaks corresponding to α-$Co(OH)_2$ phase at room temperature. At 50 °C the phase transformation to Zn/Co hydroxide nitrate started. The mixture at 50 °C had the unique green colour of α-$Co(OH)_2$, but the PXRD pattern shows there was a phase transformation from α-$Co(OH)_2$ to $CoNO_3OH{\cdot}H_2O$ phase isostructural to **aPCoZn** with slight variations in cell parameters (JCPDS Code: 48-0092; a= 17.933 Å, b=3.1435 Å ,c=14.25 Å and β= 114.8°) [32]. At 100 °C there was a colour change to pink indicative of existence of cobalt in the structure. The phase formed was identified to be mixed phases isotructural to $Zn_3(OH)_4(NO_3)_2$ and

$Zn(NO_3)_2(OH)\cdot 6H_2O$, latter being isostructural with **aPCoZn**. Finally a complete transformation to **aPCoZn** occurred at 120 °C . These interchanges between Zn and Co hydroxide nitrate phases identified shows that the final product is a mixed metal hydroxide nitrate chloride layered compound. It is interesting to note that the presence of $Zn(NO_3)_2.6H_2O$ is the most influential factor for the formation of **aPCoZn** which is tested with another zinc precursor (zinc acetate) as well as nitrate precursor (sodium nitrate). The products did not contain any crystalline phase.

A representative compound of nickel doped α-$Co(OH)_2$, $Ni_{0.2}Co_{0.8}(OH)_2$, was chosen and post synthesis was followed with $Zn(NO)_3.6H_2O$ to get **aPNiCoZn**. PXRD studies ascertained the formation of $CoNO_3OH\cdot H_2O$ phase (JCPDS Code: 48-0091) and it can be assumed that a mixed Co, Ni, Zn hydroxy nitrate is formed. This is an expected result as α-$Co(OH)_2$ forms the same phase with $Zn(NO_3)_2.6H_2O$ (Figure 4.16) and $Ni_{0.2}Co_{0.8}(OH)_2$ is isostructural with $Co(OH)_2$. The intense peak at 13.77° was indexed to be of the reflection due to (202) planes which can be observed in the case of **aPCoZn** also. The PXRD pattern of **aPNiCoZn** is exactly the same as that of **aPCoZn** implying that there is no change in the interlayer distances with the incorporation of zinc within **aPNiCoZn.** It is noteworthy that the diffractogram of the sample does not possess any peak assigned to cobalt hydroxide and nickel hydroxide.

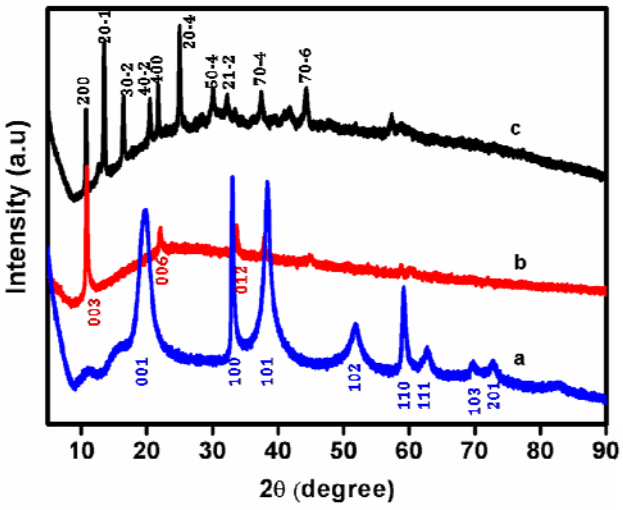

Figure 4.16. PXRD patterns of (a) $Ni(OH)_2$, (b) α-$Co(OH)_2$ and (c) **aPNiCoZn.**

aPNiCoZn has absorptions in UV and visible region. The compound is found to have a small shoulder peak around 510 nm and is observable from the Figure 4.17.

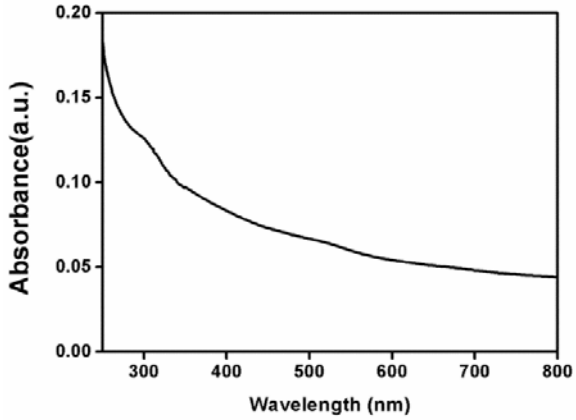

Figure 4.17. UV-vis spectum of **aPNiCoZn.**

aPCoZn and **aPNiCoZn** were tested for photocatalyic water splitting activity. It can be noted that **aPCoZn** did not show any photocatalytic activity while **aPNiCoZn** contributes to hydrogen production significantly. Also photocatalytic hydrogen evolution activity of **aPNiCoZn** is much higher compared to α-$Co(OH)_2$ (Figure 4.18) and similar to that of $Ni_{0.2}Co_{0.8}(OH)_2$. This shows that the contribution of Zn to the catalytic activity is negligible, at least in this structure form. Here also, the kinetics of O_2 evolution is not conducive for a pure water splitting and a sacrificial agent was found to be necessary [27].

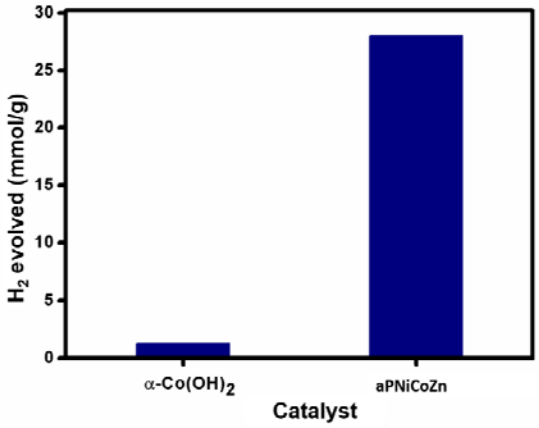

Figure 4.18. H_2 evolution in α-$Co(OH)_2$ and **aPNiCoZn** from 20% v/v methanol-water mixture under visible irradiation for 4 h.

4.5.2b.2. *In situ* synthesis route

The *in situ* synthesis route gave a highly crystalline phase, **aISCoZn** which was found to have a new structure and the PXRD pattern could not be matched to any known phases (Figure 4.19a). The SEM image in the Figure 4.19b shows the well separated hexagonal platelets forming a flower like structure. Figure 4.20 compares the PXRD patterns of α-$Co(OH)_2$ and **aISCoZn**. The peak at 11.44^0 due to the (003) plane is also present in **aISCoZn**. It can be inferred that the layering of α-$Co(OH)_2$ is also retained in **aISCoZn**.

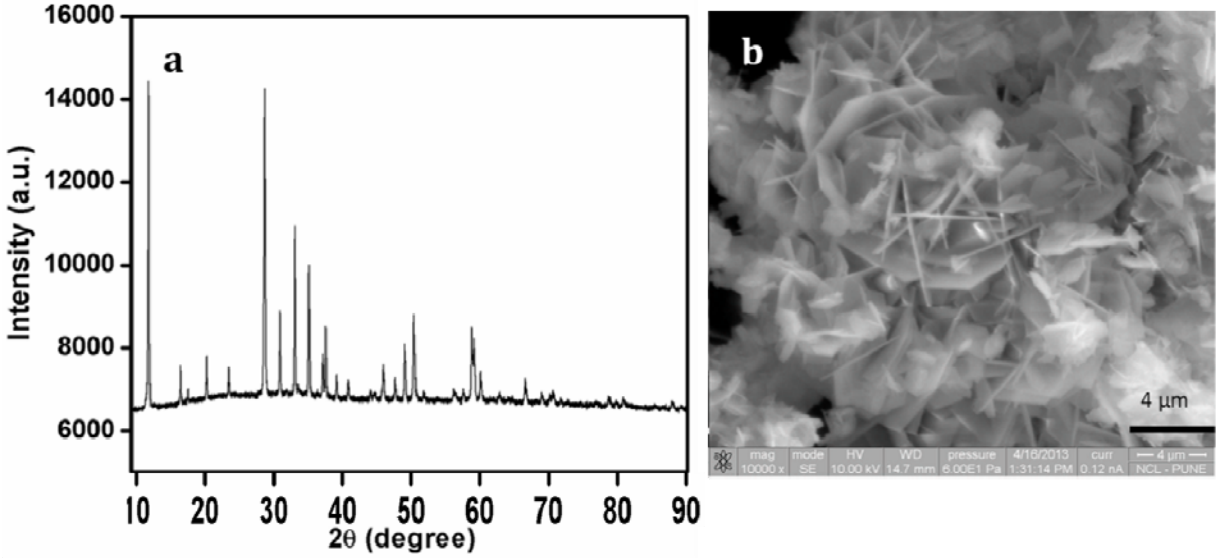

Figure 4.19. (a) PXRD pattern of **aISCoZn** and (b) SEM image of **aISCoZn.**

We have made an attempt to solve the crystal structure of **aISCoZn** from the available PXRD pattern. The obtained PXRD of **aISCoZn** pattern was analysed and indexing was carried out through Louer algorithm. Obtained crystal parameters are: a= 5.4519 Å, b=15.3161 Å, c= 3.1508 Å and β= 90.115^0 in monoclinic system. Unfortunately we could not identify any structure type fulfilling the restrictions of the above crystal parameters.

Further, the well crystalline **aISCoZn** was analyzed for its thermal stability using TGA (Figure 4.21) to identify the interlayer species. The number of water of hydration could be deduced from the first weight loss at 155 °C as two.

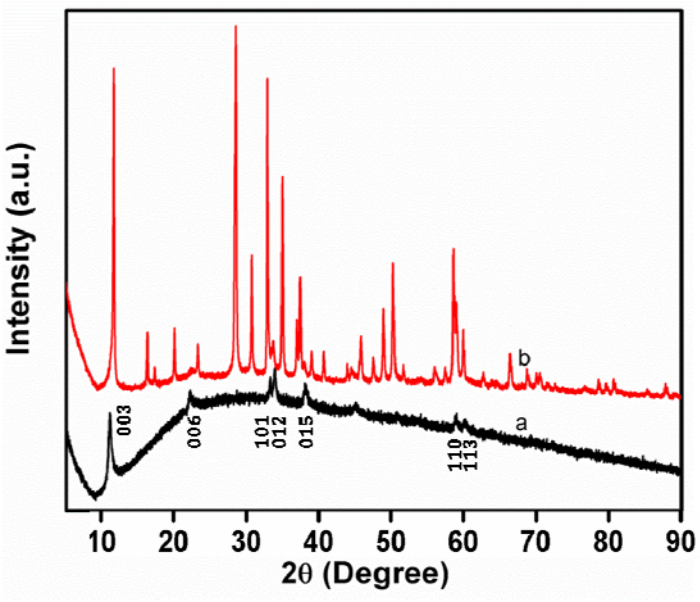

Figure 4.20. PXRD patterns of (a) α-$Co(OH)_2$ and (b) **aISCoZn.**

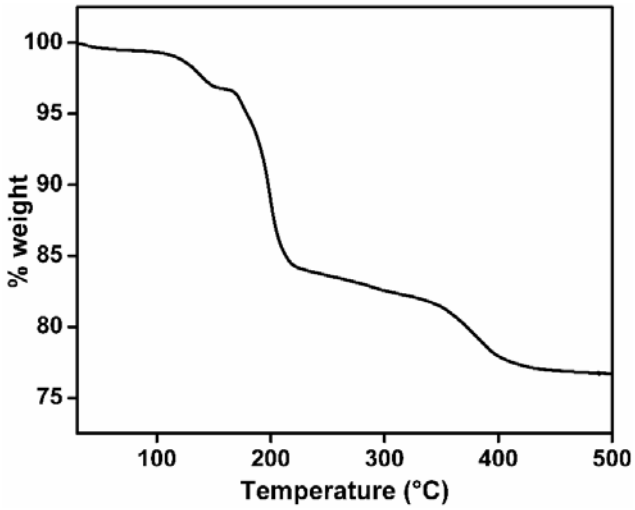

Figure 4.21. Thermogram of **aISCoZn** shows weight loss at 155 °C, 286 °C and 500 °C.

Accordingly non ambient PXRD measurements were done at different temperatures corresponding to the weight loss steps in TGA. The patterns are shown in Figure 4.22. At 155 °C the parent phase started to collapse along with the formation of ZnO. At 286 °C ZnO and a small fraction of spinel phase, $Zn_{0.96}Co_{2.04}O_4$ were formed. The peaks are found to be broad pointing to the presence of amorphous content. At 500 °C the ZnO and $Zn_{0.96}Co_{2.04}O_4$

phases became more crystalline. This also indicates the presence of a single compound with both Zn and Co present in the structure.

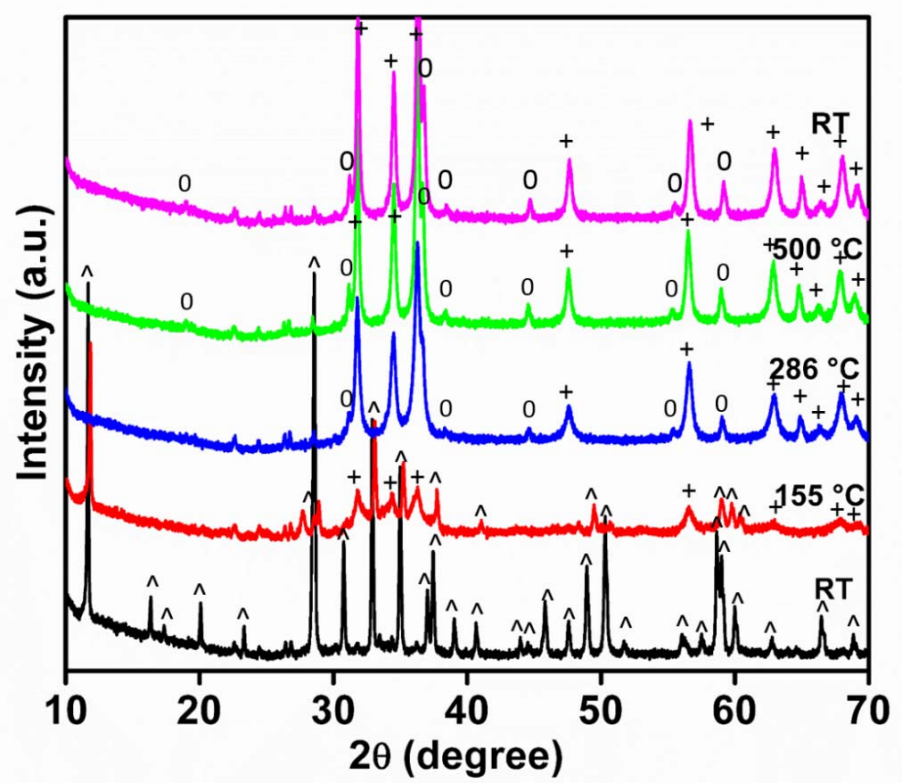

Figure 4.22. PXRD patterns of **aISCoZn** at different temperatures. Patterns are obtained from non-ambient PXRD analysis. Various phases are marked, ^: aISCoZn, +: ZnO and 0: $Zn_{0.96}Co_{2.04}O_4$.

Also the residual sample (2.4466 mg) from the TGA analysis was further checked with PXRD. The powder pattern was refined using Rietveld refinement method to find out the amount of phase fractions of $Zn_{0.96}Co_{2.04}O_4$ and ZnO. The refinement proceeded smoothly and the goodness of fit was reasonable. The refined pattern is shown in Figure 4.23. The table 4.5 shows that at 500 °C **aISCoZn** has 90.77% ZnO and 9.23% of $Zn_{0.96}Co_{2.04}O_4$ spinel phase. By combining the weight loss, and the phase fractions obtained by Rietveld refinement, the formula of the **aISCoZn** was assigned tentatively as $Zn_{2.44}Co_{0.46}(OH)_{3.8}(NO_3)_{1.97}.2H_2O$. Tha calculations are given in appendix 2.5.

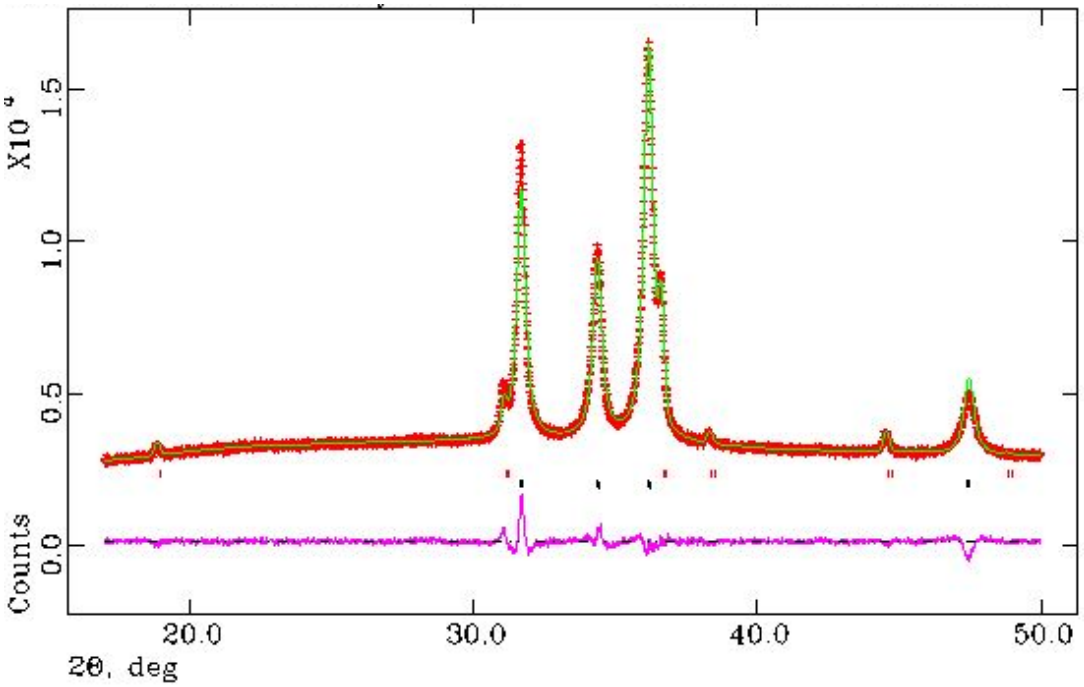

Figure 4.23. Rietveld refinement of the PXRD pattern of **aISCoZn** heated at 500 °C. The pattern shows two phases, *viz*., ZnO and $Zn_{0.96}Co_{2.04}O_4$. Red line represents experimental data, green line is the Rietveld fit and pink line represents difference plot. Vertical lines are expected positions for $Zn_{0.96}Co_{2.04}O_4$ phase (red) and ZnO (black).

Table 4.5. Rietveld refinement parameters for **aISCoZn** heated at 500 °C

Compound	**aISCoZn**
χ^2	2.240
Rp	1.73
wRp	2.48
% ZnO	90.77
% Spinel ($Zn_{0.96}Co_{2.04}O_4$)	9.23

Our next attempt was to identify a correlation of the indexed parameters to any other known structure types. Louer, M. *et al*. reported the crystal structure of $Zn_3(OH)_4(NO_3)_2$ and found that the compound crystalizes in monoclinic system with cell parameters a= 7.038 Å, b= 9.658 Å, c= 11.182 Å and β= 100.96° [33]. A close inspection of the cell parameters obtained after the indexing with the cell parameters for $Zn_3(OH)_4(NO_3)_2$, led us to derive a unit cell for **aISCoZn** out of the unit cell of

$Zn_3(OH)_4(NO_3)_2$ (Figure 4.24) by transforming the cell parameters and atomic coordinates using the relation,

$$\begin{bmatrix} a' \\ b' \\ c' \end{bmatrix} = \begin{bmatrix} a \\ b \\ c \end{bmatrix} \begin{bmatrix} 0 & 0 & 0.5 \\ 2 & 0 & 0 \\ 0 & 1/3 & 0 \end{bmatrix}$$

The transformed parameters are tabulated in Table 4.6. The PXRD pattern simulated using the above transformation matched well with the pattern of the compound as shown in Figure 4.25. However, further refinement did not proceed smoothly and hence we can conclude about the structure only partially. The structure may contain a mixed Co/Zn layered hydroxide phase along with NO_3^- ion intercalation. These cations can be interconnected with edge shared octahedra which is expected to be formed by the oxygens from the hydroxyl as well as nitrate ions.

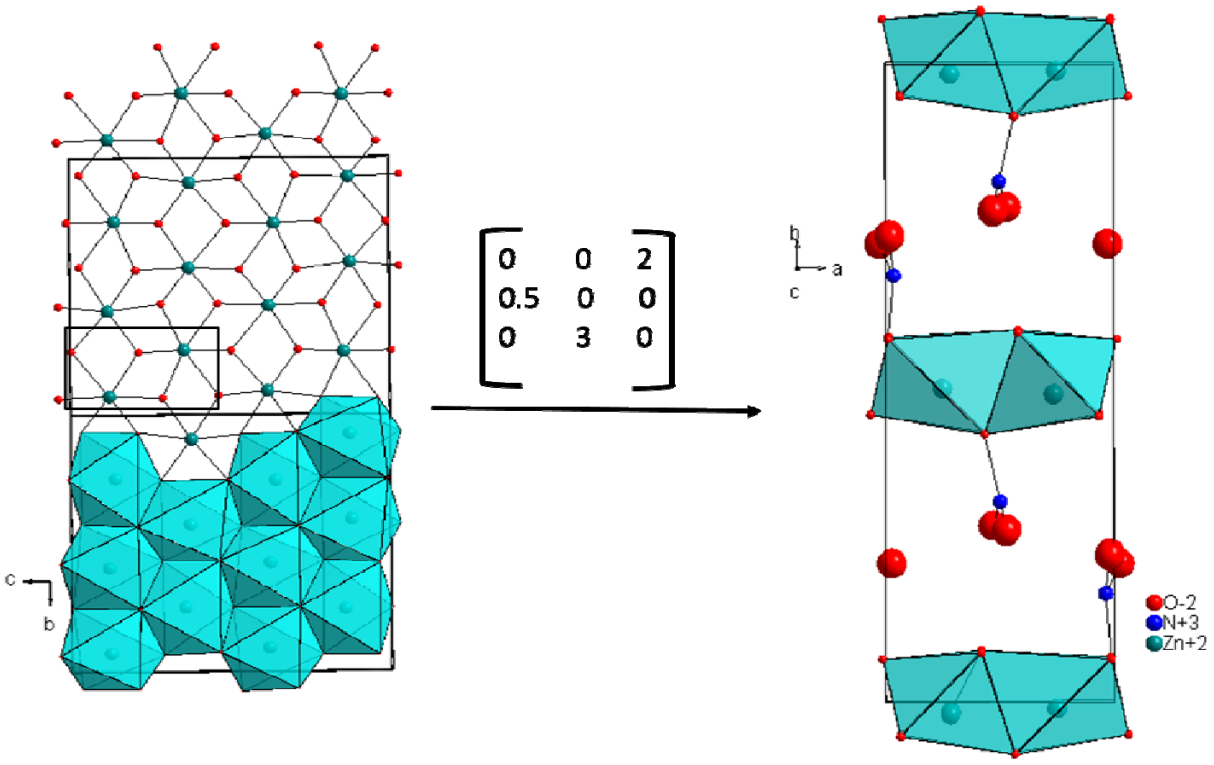

Figure 4.24. The structure of **aISCoZn** derived from the crystal structure of $Zn_3(OH)_4(NO_3)_2$ using the transformation.

Table 4.6. Crystal structure parameters obtained for **aISCoZn** after the transformation.

Atoms	x	Y	z
Zn1	0.7506	0.9900	0.7780
Zn2	0.2836	0.9830	0.2392
O1	0.0652	0.9495	0.7708
O2	0.5652	0.91970	0.2629
O3	0.4722	0.7697	0.9477
O4	0.5290	0.7755	0.6014
O5	0.9730	0.7170	0.3939
O6	0.0176	0.7306	0.0422
O7	0.0120	0.5692	0.7446
O8	0.5802	0.5813	0.1980
N1	0.4974	0.8145	0.2636
N2	0.0364	0.6682	0.7020

Space group *P* 21/a; a=5.4519 Å, b=15.3161 Å , c=3.1508 Å , α=90° , β=90.115° and γ=90°

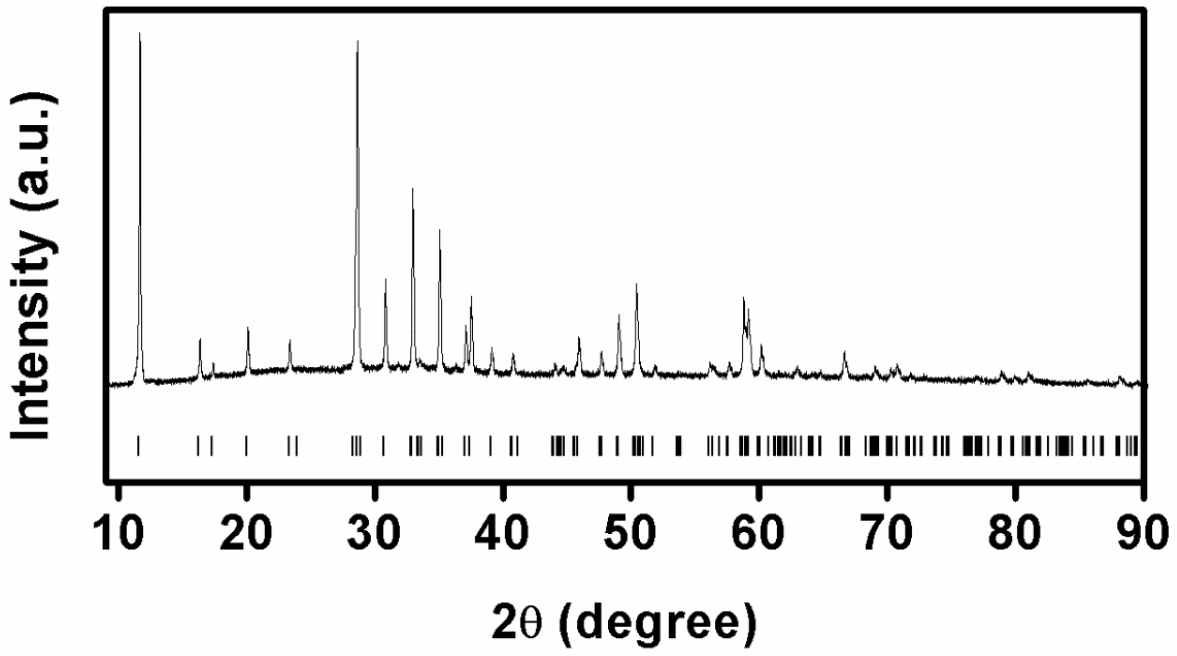

Figure 4.25. PXRD pattern of **aISCoZn** and the simulated pattern as small vertical lines.

4.5.2b.3. Simultaneous incorporation of Ni and Zn in α-$Co(OH)_2$

Since **aISCoZn** is inactive for photocatalytic hydrogen evolution reaction, an attempt was made to incorporate Ni along with Zn in α-$Co(OH)_2$ in order to create a new catalytic site. For that, various amounts of $Ni(NO_3)_2$, with a Co/Ni ratio of (9:1, 8:2 and 7:3) were added to the reaction mixture during the course of reaction. The obtained phases are named as **aISNiCoZn9**, **aISNiCoZn8** and **aISNiCoZn7 respectively.** The Figure 4.26 shows the PXRD patterns of the Ni incorporated **aISCoZn**. It is found that a new phase was forming along with **aISCoZn**. The new phase has prominent PXRD peaks at 11.05°, 22.22°, 33.6°, 37.8° etc. The pattern has a close matching with the PXRD pattern of green rust which is a layered double hydroxide of Fe^{2+}/Fe^{3+} ions [34]. Hence we can conclude that the added Ni exists as a separate phase structurally similar to iron hydroxide. Figure 4.27 shows a magnified portion of the PXRD pattern which clearly shows that the amount of the new phase grows with increasing amount of Ni.

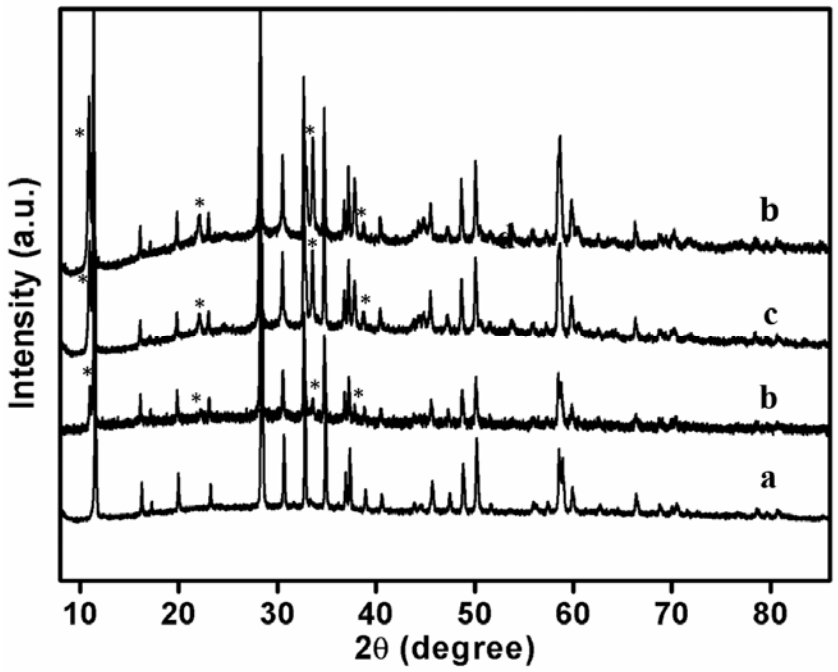

Figure 4.26. PXRD patterns of a) **aISCoZn**, b) **aISNiCoZn9**, c) **aISNiCoZn8** and d) **aISNiCoZn7.** The new phase is indicated with *.

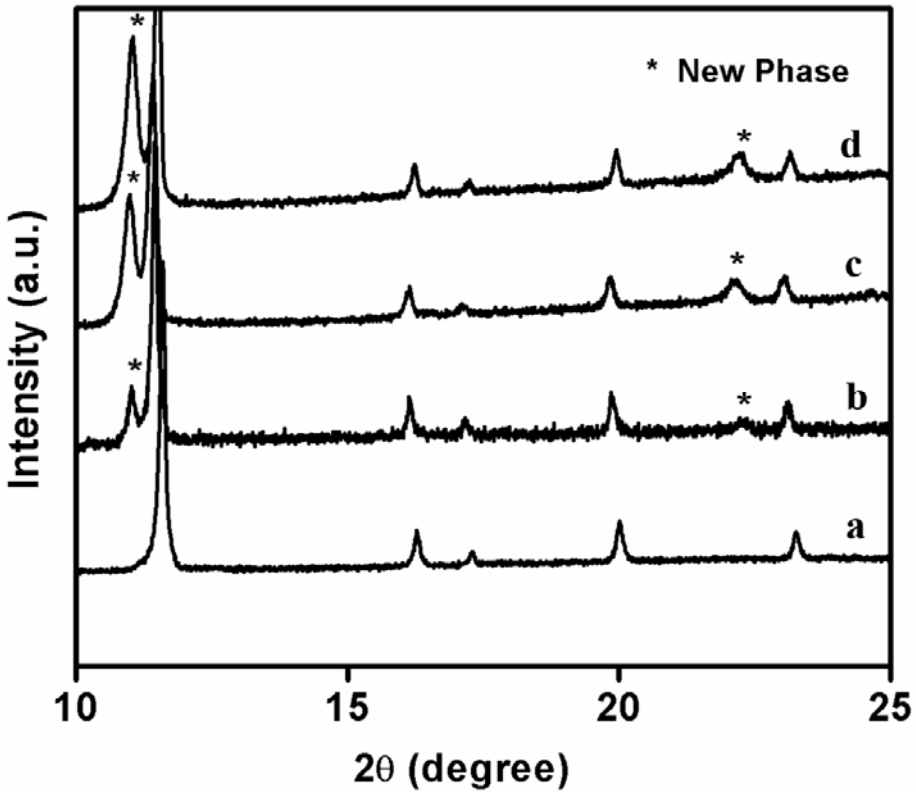

Figure 4.27. PXRD pattern of a) **aISCoZn**, b) **aISNiCoZn9**, c) **aISNiCoZn8** and d) **aISNiCoZn7**. Peaks marked * show peaks corresponding to the new phase.

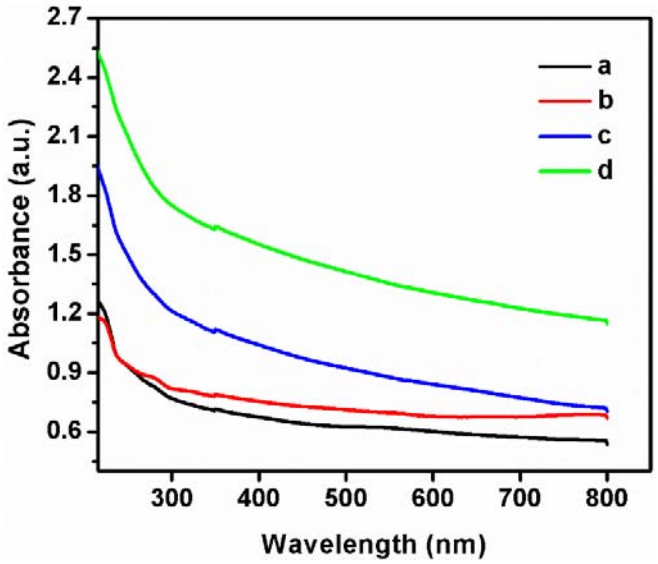

Figure 4.28. UV-vis spectra of a) **aISCoZn**, b) **aISNiCoZn9**, c) **aISNiCoZn8** and d) **aISNiCoZn7.**

All the four samples were dispersed in methanol and analyzed by UV-vis spectroscopy (Figure 4.28). These catalysts did not show any absorption characteristics in the visible region.

In further experiments the photocatalytic activities of **aISCoZn** as well **aISNiCoZn9**, **aISNiCoZn8** and **aISNiCoZn7** were tested with and without methanol (Figure 4.29). The catalysts were found to have very low but equal catalytic activity in the presence of sacrificial agent indicating that the concentration of the new Ni phase has no effect on the activity in the presence of sacrificial agent. Surprisingly all catalyst were active, albeit poor, even without methanol, except the one without nickel, under visible irradiation. This places these catalysts in a separate league when compared to other layered compounds presented here. Also, it is to be noted that the activity increases with the amount of Ni phase, which may indicate that the new Ni phase may be responsible for pure water splitting.

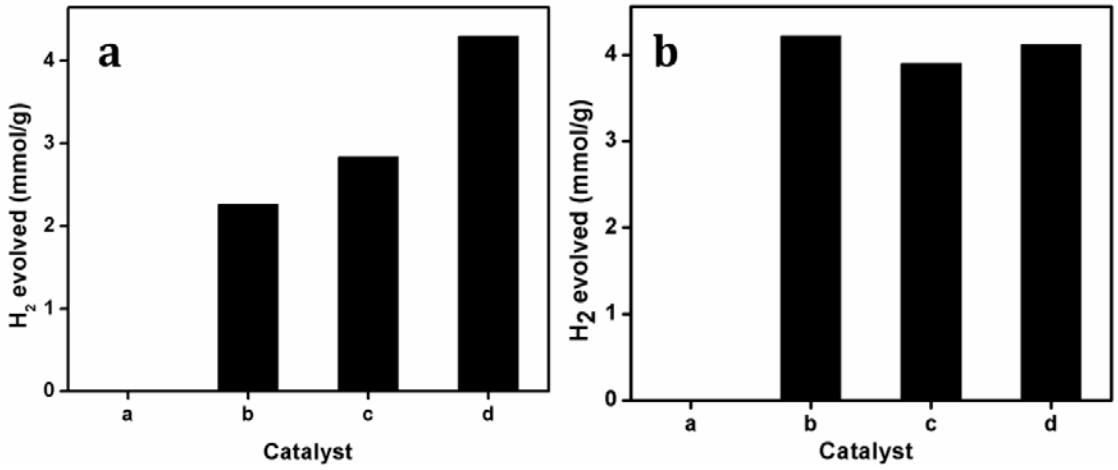

Figure 4.29. H_2 evolution activity of a) **aISCoZn**, b) **aISNiCoZn9**, c) **aISNiCoZn8** and d) **aISNiCoZn7** from (a) pure water and (b) from 20 v/v% methanol - water mixture under visible irradiation for 4 h with 10 mg of the catalysts.

4.6. Conclusions

Layered double hydroxides of cobalt and their modifications were studied for photocalytic water splitting. Well known α-$Co(OH)_2$ and β-$Co(OH)_2$ were synthesized through a reported procedure and further efforts were made to modify the layered hydroxides. Our interest is restricted to α-$Co(OH)_2$ because it has a wide tunability with the

reaction with other metals as well as it possesses large inter layer space. Addition of zinc nitrate hydrate was done through two different processes i.e.; *in situ* addition and post synthesis. Both routes resulted in different products. New catalytic sites were created using Ni as a dopant. Ni doping in α-$Co(OH)_2$ resulted in a photocatalyst for water splitting which in not reported in the literature. The series of photocatalysts, $Ni_xCo_{1-x}(OH)_2$ [x= 0.1, 0.2, 0.3, 0.4 and 0.5] are active under visible light irradiation in aqueous methanol. Nickel and zinc incorporated in α-$Co(OH)_2$ through *in situ* route is found to be a potential candidate as it evolves hydrogen from pure water under visible irradiation. Figure 4.30 depicts comparative information on the photocatalytic activities of different photocatalysts discussed in this chapter.

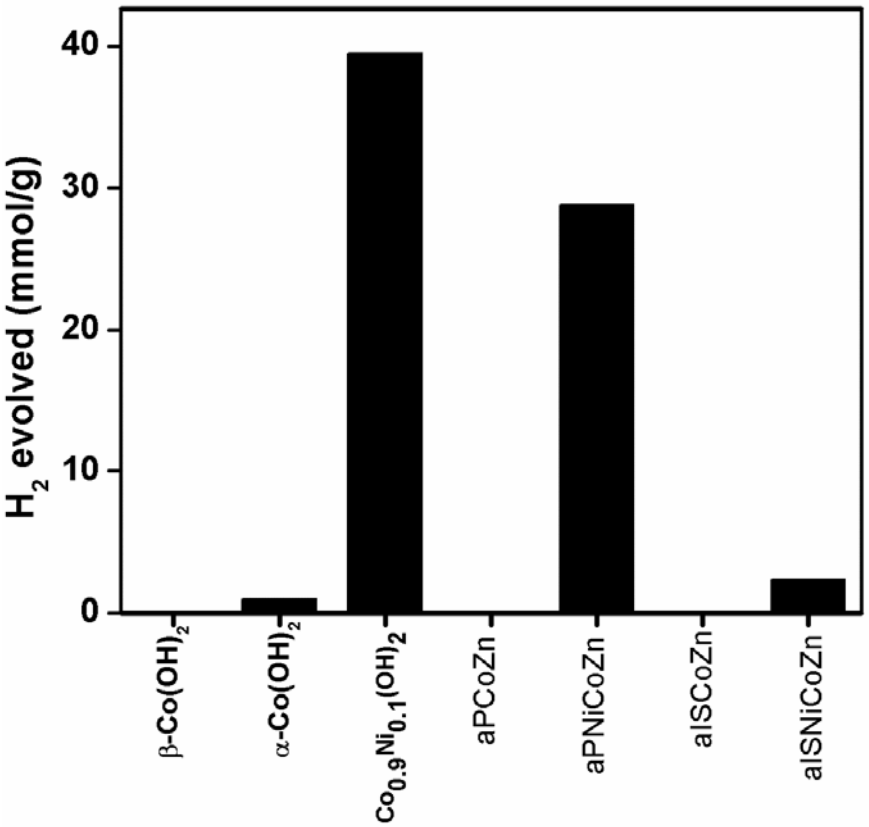

Figure 4.30. Comparison of various catalysts for photocatalytic H_2 under visible light irradiation for 4 h. The reaction medium is 20 v/v% methanol - water mixture in all cases except **aISNiCoZn** (nickel and zinc incorporated in α-$Co(OH)_2$ through *in situ* route) for which the reaction was carried out in pure water.

β-$Co(OH)_2$ is inactive for photocatalytic hydrogen evolution while α-$Co(OH)_2$ shows very low activity in aqueous methanol solution under visible light irradiation compared to other catalysts. On loading nickel into α-$Co(OH)_2$, there is a significant increase in the photocatalytic hydrogen evolution. This can be correlated to the creation of H_2 evolution sites by incorporating nickel as well the new catalytic site separation for water oxidation and reduction. Higher nickel doping reduces the activity of α-$Co(OH)_2$. This may be attributed to the enhanced recombination of the photogenerated charge carriers or to the backward reaction to produce water. Incorporation of zinc by post as well as *in situ* synthesis method did not create any catalytic site for hydrogen evolution in α-$Co(OH)_2$. But the presence of nickel played an intriguing role here also. **aPNiCoZn** (zinc incorporated through post synthesis method in $Co_{0.8}Ni_{0.2}(OH)_2$) can also evolve hydrogen from aqueous methanol under visible light irradiation. Interestingly, incorporation of nickel in **aISCoZn** (zinc incorporated in α-$Co(OH)_2$ through *in situ* route) leads to an overall water splitting catalyst which works even without a sacrificial agent under visible irradiation. But the activity is less compared to other nickel incorporated catalyst discussed in this chapter. Zinc incorporation did not affect the photocatalytic activity in any of the compounds discussed in this chapter. But nickel doping in appropriate concentrations in α-$Co(OH)_2$ yields good hydrogen evolution catalysts.

References

1. Wang, Q.; O'Hare, D. *Chem. Rev.* **2012**, *112*, 4124.
2. Rogez, G.; Massobrio, C.; Rabu, P.; Drillon, M. *Chem. Soc. Rev*. **2011**, *40*, 1031.
3. Chen, H.; Hu, L.; Chen, M.; Wu, Y. Y. *Adv. Func. Mater.* **2014,** *24*, 934.
4. Xu, Z. P.;Zeng, H. C. *Chem. Mater*. **1999**, *11*, 67.
5. Symes, M. D.; Lutterman, D. A.; Teets, T. S.; Anderson, B. L.; Breen, J. J.; Nocera, D. G. *ChemSusChem.* **2013**, *6*, 65.
6. Hutchings, G. S.; Zhang, Y.; Li, J.; Yonemoto, B. T.; Zhou, X.; Zhu, K.; Jiao, F. *J. Am. Chem. Soc*. **2015**, *137*, 4223.
7. Mockenhaupt, C.; Zeiske, T.; Lutz, H. D. *J. Mol. Struct.* **1998**, *443*, 191.

8. Ma, R.; Liu, Z.; Takada, K.; Fukuda, K.; Ebina, Y.; Bando, Y.; Sasaki, T. *Inorg. Chem.* **2006**, *45*, 10.
9. Liu, Z.; Ma, R.; Osada, M.; Takada, K.; Sasaki, T. *J. Am. Chem. Soc*. **2005**, *127,* 13869.
10. Orita, M.; Tanji, H.; Mizuno, M.; Adachi, H.; Tanaka, I. *Rev. B* **2000**, *61*, 1811.
11. Natalia, J.; Costa, S.; Guerrero, M.; Collière, V.; Teixeira-Neto, E.; Landers, R.; Philippot, K.; Rossi, L. M. *ACS Catal.* **2014**, *4*, 1735
12. Breitenfeld, J.; Wodrich, M. D.; Hu, X. *Organometallics* **2014**, *33*, 5708
13. Kudo, A.; Sayama, K.; Tanaka, A.; Asakura, K.; Domen, K.; Maruya, K.; Onishi, T. *J. Catal*. **1989**, *120*, 337.
14. Sayama, K., Yase, K.; Arakawa, H.; Asakura, K.; Tanaka, A.; Domen, K.; Onishi, T. *J. Photochem. Photobiol. A* **1998**, *114*, 125.
15. Li, J.; Yang, M.; Wei, J.; Zhou, Z. *Nanoscale* **2012**, *4*, 4498
16. Kamat, P. V.;Patrick, B. *J. Phys. Chem.* **1992**, *96*, 6829
17. Cao, L.; Xu, F.; Liang, Y. Y.; Li, H. L. *Adv. Mater.* **2004***, 16*, 1853.
18. Zhao, T.; Jiang, H.; Ma, J. *J. Power Sources* **2011**, *196*, 860.
19. Gao, M.; Sheng, W.; Zhuang, Z.; Fang, Q.; Gu, S.; Jiang, J.; Yan. Y. *J. Am. Chem. Soc.* **2014**, *136*, 7077.
20. Hu, W. K.; Nore´us, W. K. *D. Chem. Mater.***2003**, *15*, 974.
21. Delmas, C.; Braconnier, J. J.; Borthomieu, Y.; Hagenmuller, P. *Mater. Res. Bull.* **1987**, *22*, 741.
22. Demourgues-Guerlou, L.; Braconnier J. J.; Delmas, C. *J. Solid State Chem.* **1993**, *104*, 359.
23. Demourgues-Guerlou, L.; Delmas, C. *J. Power Sources* **1994**, *52*, 269.
24. Kamath, P. V.; Dixit, M.; Indira, L.; Shukla, A. K.; Kumar, V. G.; Munichandraiah, *J. Electrochem. Soc.* **1994**, *141*, 2956.
25. Tessier, C.; Demourgues-Guerlou, L.; Faure, C.; Basterreix, M.; Nabias, G.; Delmas, C. *Solid State Ionics* **2000,** *133*, 11.
26. Hall, D. S.; Lockwood, D. J.; Bock, C.; MacDougall, B. R. *Proc. R. Soc. A* **2015**, *471*, 20140792.
27. Hykaway, N.; Sears, W. M.; Morisaki, H.; Morrison, S. R. *J. Phys. Chem.* **1986**, *90*, 6663.
28. Surendranath, Y.; W. Kanan, M. W.; Nocera, D. G. *J. Am. Chem. Soc.* **2010**, *132*, 16501

29. Li, P.; Xu, Z. P.; Hampton, M. A.; Vu, D. T.; Huang, L.; Rudolph, V.; Nguyen, A. V. *J. Phys. Chem. C* **2012**, *116*, 10325.
30. Cursino, A. C. T.; Gardolinski, J. E. C.; Wypych, F. *J. Colloid and Interf. Sci.* **2010,** *347,* 49.
31. Wu, J. H.; Varghese, B.; Zhou, X. D.; Teo, S. Y.; Sow, C. H.; Ang, S. G.; Xu, G. Q. *Chem. Mater.* **2010**, *22*, 1533.
32. Angelov, S.; Drillon, M.; Zhecheva, J, E.; Stoyanova, R.; Belaiche, M.; Derory, A.; Herrlb, A. *Znorg. Chem*. **1992**, *31*, 1514.
33. Louer, M.; Louer, D.; Grandjean, D. *Acta Crystallogr. B,* **1973**, *29*, 1696.
34. Drissi, S. H.; Refait, P.; Abdelmoula, M.; Génin, J. M. R. *Corros. Sci.* **1995**, *37*, 2025.

Chapter 5

Summary, conclusions and future perspectives

5.1. Summary

Chapter 1 presents a general introduction to photocatalytic water splitting reaction over numerous metal oxide photocatalysts. The essential criterion for a photocatalyst to split water and the mechanistic steps involved in photocatalytic water splitting reactions are discussed in detail. Various strategies used in visible light utilization as well as photocatalysts are also presented in this chapter. Layered materials garnered special attention in photocatalytic water splitting reaction due to the favourable structural features which can minimize the recombination of the photogenerated charge carriers. The chapter further presents a comprehensive review of literature on various layered materials used as photocatalyst including metal oxides and hydroxides. Semiconductors possessing spatial separation of photogenerated charge carriers can be utilized for photocatalytic water splitting since the charge generation and conduction pathways are well separated within the 3D bulk structures. In addition, it describes the interesting structural aspects of layered hydroxides based on nickel and cobalt along with a few reports on photocatalytic activities of layered hydroxides. The chapter briefly describes the role of layered materials in photocatalytic water splitting reaction. Finally the scope and objective of the thesis are stated.

Chapter 2 discusses layered oxides of the series $InGaO_3(ZnO)_m$ (m = 1– 4) which are interesting due to their structural anisotropy. This chapter describes a comprehensive study of their structural details, focusing on the local cationic environment in bulk powder samples by MAS NMR and EXAFS, which is hitherto not attempted. It is found that the Ga geometry varies gradually from pure pentacoordinated to a mixture of penta and tetracoordinated with increasing amounts of tetracoordination as we move across the series, contrary to previous reports suggesting exclusively trigonal bipyramidal coordination in all the compounds. A similar observation is also made in the case of Zn and structural evolution involving the dissolution of Ga in a ZnO_4 tetrahedral network in a sandwich layer can be discerned, as the insulating ZnO layer size increases. $InGaO_3(ZnO)_m$ series of oxides is found to be active for photocatalytic H_2 evolution from water-methanol mixtures. The structure of this series is highly anisotropic with InO_6 octahedral layers sandwiching Ga/ZnO_n

polyhedra. The structural anisotropy in which the conducting layer is spatially separated from the charge generation sites may help in suppressing charge recombination and consequently enhance the catalytic activity. The band gaps of the series are above 3.6 eV and hence they are not active under visible light irradiation. H_2 evolution is considerably enhanced under UV light on employing NiO as cocatalyst due to facile electron transfer from $InGaO_3(ZnO)_m$ to NiO. However, when CuO is used as cocatalyst, visible light activity could be brought out. Due to the very low band gap of CuO, it can act as a sensitizer absorbing in visible light. The band positions become conducive for H_2 evolution due to band alignments consequent to electron accumulation in CuO conduction band.

Chapter 3 presents $InFeO_3(ZnO)_m$ series of oxides which are found to give unprecedented H_2 evolution from water–methanol mixtures without using any cocatalysts. This family of compounds has an anisotropically layered structure in which Zn/FeO_n polyhedra are sandwiched between InO_6 octahedral layers. Local structure characterization by X-ray absorption spectroscopy reveals that Zn coordination changes from pentacoordinated to tetrahedral geometry across the series, whereas Fe geometry remains trigonal bipyramidal in all the compounds. This peculiar structure is conducive for spatial separation of photogenerated charges, reducing the recombination losses. Band gap energies calculated from absorption spectra indicate potential visible light activity, and this may be due to the orbital mixing of Fe 3d and O 2p as revealed by pre-edge features of X-ray absorption spectra. Band positions are also advantageously placed for a visible light H_2 generation and is indeed found to be the case in methanol-assisted water splitting with standardized hydrogen evolution of ~19.5 mmol g^{-1} h^{-1} for all the catalysts.

Chapter 4 describes the synthesis and modifications of α-$Co(OH)_2$ and β-$Co(OH)_2$ with zinc was attempted. Ni catalytic site incorporation by doping was tried in α-$Co(OH)_2$ which created a new catalytic site for photocatalytic hydrogen evolution under visible light. Various methods of synthesis like post-synthetic modification and *in situ* methods were attempted which led to the formation of a layered Zn-Co-Ni hydroxide composite which was found to absorb in visible region and acted as

hydrogen evolution catalyst even without a sacrificial agent under visible irradiation. Nickel incorporated in post synthesized zinc loaded α-$Co(OH)_2$ was also found to be active in aqueous methanol under visible light irradiation.

5.2. Conclusions

- The ^{71}Ga MAS NMR and EXAFS analysis indicate the existence of sandwich layer (between In–O layers) in $InGaO_3(ZnO)_m$ (m = 1– 4), which has a stratified structure: an outer strata of ZnO tetrahedra and an inner strata of Ga–O/Zn– O with random mixing of Ga and Zn sites.
- Both Ga and Zn exist in increasingly tetrahedral coordination as we go across the series.
- This inner strata most probably has gallium oxide solubilized in ZnO, especially at high m values (due to high amounts of ZnO) and hence, has a wurtzite type structure with corner sharing tetrahedra.
- Series of compounds $InGaO_3(ZnO)_m$ (m = 1– 4) are identified as UV active photocatalysts for H_2 evolution from aqueous methanol.
- The photocatalytic activity is enhanced two-fold by employing NiO as cocatalyst due to facile electron transfer from conduction bands of $InGaO_3(ZnO)_m$ to NiO.
- Band gap energies observed from UV–vis absorbance spectroscopy indicate visible light absorbance in CuO loaded $InGaO_3(ZnO)_m$.
- H_2 evolution activity for parent compounds under UV irradiation and their CuO composites under visible light irradiation are found to be similar. This indicates that the catalytic sites are present on $InGaO_3(ZnO)_m$ in both the cases.
- Band gap energies observed from UV–vis absorbance spectroscopy indicate visible light absorbance in CuO loaded $InGaO_3(ZnO)_m$.
- The EXAFS analysis indicates that Fe is in pentacoordination in $InFeO_3(ZnO)_m$ (m=1 – 4)
- Flat band potentials are calculated from Mulliken electronegativities, and they show appropriately placed conduction band to enable H_2 evolution.

- EXAFS studies indicate a possible orbital mixing of Fe 3d and O 2p assisting in Fe contribution to the conduction band and lowering of the band gap conducive for visible light catalytic activity.
- $InFeO_3(ZnO)_m$ materials are active photocatalysts for H_2 evolution without employing any cocatalyst under visible light in presence of methanol.
- Co based layered hydroxide systems with proper incorporation of hydrogen evolving site can act as an excellent photocatalytic water splitting catalyst.
- Attempts were made to incorporate zinc and nickel in layered cobalt hydroxides.
- Nickel doped α-$Co(OH)_2$ is found to be effective for photocatalytic hydrogen generation from aqueous methanol.
- The catalytic site separation is achieved here by modifying the synthesis strategy. Here post synthesis route and *in situ* synthesis route were followed.
- Nickel incorporation in α-$Co(OH)_2$ through *in situ* synthesis route resulted in a catalyst which work even without a cocatalyst and in the absence of a sacrificial agent in visible light. Zinc incorporation in $Ni_{0.2}Co_{0.8}(OH)_2$ also led to a photocatalyst for water splitting from aqueous methanol under visible light irradiation.
- In these compounds, nickel and cobalt sites may act as redox sites.

5.3 Future perspectives

Based on the outcomes of the present studies on $InGaO_3(ZnO)_m$ and $InFeO_3(ZnO)_m$ series of compounds, it is expected that the work can be extended to make the above catalysts much more efficient for photocatalytic H_2 generation. Aliovalent doping, which is capable of bringing visible light activity in $InGaO_3(ZnO)_m$ series still remains as a challenge. Doping in $InGa/FeO_3(ZnO)_m$ is not possible through simple solid state method or solution combustion route. Other synthesis routes need to be investigated for doping in these materials. Since conduction bands of the series of compounds consist of In 5s orbitals, the metal ion doping in In position can change the conduction band level. The dopants are to be chosen in such a way that it will form a conduction band below In 5s which will effectively reduce the band gap. If a dopant can go to the position of Zn, Ga or Fe it may increase the carrier concentration. Here the

dopants should possess a valence band position which is above the Zn 3d or O 2p levels. Anion doping is another possibility to improve the visible light activity in these compounds. The synthesis conditions need to be improved for modification of the compounds by doping.

Cobalt based layered hydroxides are much more susceptible to structural transformations with the incorporation of different ions. In the present study, a few metal ions were chosen and the results were promising. It is worthwhile to study the incorporation of various transition metal ions in layered cobalt hydroxides. The effect of different parameters like concentration, temperature etc. need to be investigated to design layered hydroxides with improved structural and optical properties.

List of Publications

1. Investigations into variations in local cationic environment in layered oxide series $InGaO_3(ZnO)_m$ (m = 1–4) **Soumya B. Narendranath**, Ashok Kumar Yadav, T. G. Ajithkumar, Dibyendu Bhattacharyya, Shambhu Nath Jha, Krishna K. Dey, Thirumalaiswamy Raja and R. Nandini Devi, *Dalton Trans.*, **2014**, *43*, 2120.

2. Photocatalytic H_2 Evolution from Water–Methanol System by Anisotropic $InFeO_3(ZnO)_m$ Oxides without Cocatalyst in Visible Light **Soumya B. Narendranath**, Ashok Kumar Yadav, Dibyendu Bhattacharyya, Shambu Nath Jha, and R. Nandini Devi, *ACS Appl. Mater. Interfaces* **2014**, *6*, 12321.

3. Photocatalytic H_2 evolution from water-methanol mixtures on $InGaO_3(ZnO)_m$ with an anisotropic layered structure **Soumya B. Narendranath**, Saranya V. Thekkeparambil, Leena George, Shibin Thundiyil and R. Nandini Devi, *Journal of Molecular Catalysis A: Chemical*, **2016**, *415***,** 82.

4. Water splitting activity of layered oxides R. Nandini Devi and **Soumya B. Narendranth.** Patent international publication number: WO 2015/029071 A1 dated 5th march 2015.

Contributions to Symposia/Conference

1. Presented poster entitled "Layered solid state compounds for solar energy utilization" at CSIR-National Chemical Laboratory, Pune on science day held in February 2012.

2. Presented poster entitled "Layered $InGa/FeO_3(ZnO)_m$ for photocatalytic water splitting" at CSIR-National Chemical laboratory, Pune on science day held in February 2013.

3. Presented poster entitled "Layered $InGaO_3(ZnO)_m$ series of compounds for photocatalytic water splitting" for CATSYMP 2013 at CSIR-Indian Institute of Chemical Technology, Hyderabad held in February 2013.

4. Presented poster entitled “Layered $InGaZnO_4$ for photocatalytic water splitting under UV light irradiation” for TAPSUN conference at CSIR-CLRI, Chennai held in September 2013.

Appendix 1

Physicochemical Characterizations

Various physicochemical techniques can be used for the characterization of the perovskite materials. The principles of techniques, used in the present study like powder diffraction using laboratory X-rays, Rietveld refinement, ^{71}Ga MAS NMR, EXAFS, SEM EDAX, UV-visible spectroscopy, Surface area analysis using N_2 adsorption, Impedance spectroscopy and XPS.

1. Powder Diffraction

Understanding and predicting the properties of scientific and technologically important materials require the exact knowledge of its structure. The structure of an idealized crystal lattice consists of periodic arrangement atoms and single crystal analysis is the most suitable technique to understand it. However, because of the unavailability of suitable single crystals in many cases and to extract information on the bulk material, alternative technique, powder diffraction is routinely used. Moreover it can be used for the determination of microstructural properties, disorder in materials, studies of macroscopic stresses in components, and texture of polycrystalline samples.

X-rays are electromagnetic waves having wavelengths of the order of 1Å, which is comparable with the spacing between lattice planes in crystals. X-ray diffraction, based on wide-angle elastic scattering of X-rays, is the most important and common tool to determine the structure of the materials characterized by the long range ordering. X-ray diffraction involves the measurement of the intensity of X-rays scattered from electrons or neutrons bound to atoms. Waves scattered at atoms at different positions arrive at the detector with a relative phase shift. Therefore, the measured intensities yield information about the relative atomic positions. The diffraction patterns gives information about structure formation, phase purity, degree of crystallinity, and unit cell parameters of the materials. The formation of a structural phase can be confirmed by comparing the powder diffraction patterns with that of pure reference phases distributed by International Center for Diffraction Data (ICDD).

The use of Bragg's equation is the easiest way to get to the structural information in powder diffraction, the derivation of which considers X-ray diffraction as a reflection of X-

rays by sets of lattice planes. As the X-rays penetrate deeply, additional reflections occur at thousands of consecutive parallel planes. The overlap of the scattered X-rays occurs since all are reflected in the same direction.

The Braggs equation is $n\lambda = 2d\sin\theta$, where d is the interplanar spacing of parallel lattice planes and 2θ is the diffraction angle, the angle between the incoming and outgoing X-ray beams.

Sharp intensities emerge from the sample only at the special angles where Bragg's equation holds. For crystalline materials, the destructive interference results in a completely destruction of intensity in all the other directions. In the modern flat-plate powder X-ray diffractometer, used most commonly in industrial and academic laboratories, the divergent incident beam is allowed to reflect from the sample and converges at a fixed radius from the sample position. This configuration is commonly referred to as "Bragg–Brentano" geometry (shown in Figure 6). The spinning of sample about an axis normal to the flat plate results in a good powder average.

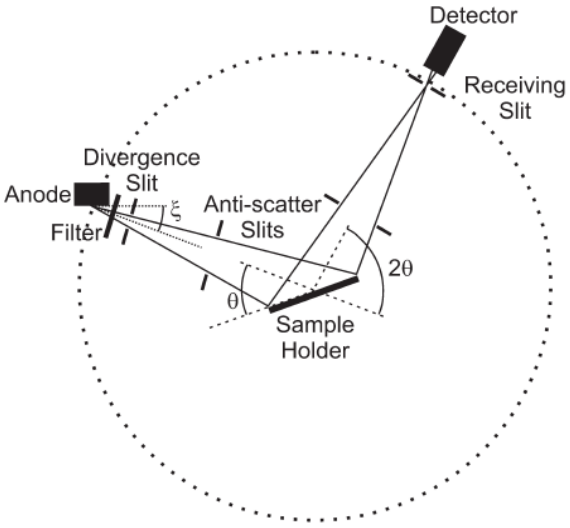

Figure 1. Schematic representation of Bragg–Brentano geometry.

Powder diffraction experiments, exploits X-rays from a laboratory generator or from a high energy storage ring (synchrotron radiation), or neutrons produced in a reactor or spallation source. A typical wavelength used lies in the range 0.1-5 Å, comparable with the spacings between lattice planes in crystals. Data can be collected in transmission or reflection modes, depending on the absorption of radiation by the sample.

A brief description of the different sources used for the powder diffraction experiments are given here.

1.1. Laboratory X-ray Sources

In a standard laboratory instrument, the X-rays are produced in a sealed-tube source where electrons, accelerated by a potential difference of up to 60 kV, bombard a metal anode inside a vacuum tube. This results in the formation of a characteristic radiation spectrum composed of discrete peaks arising from the filling of vacant level in the inner shell (created from the ejection of electron by the incoming electron) by a higher atomic level electron. The emission of an X-ray photon is characterised by the difference in energy between the two levels. A higher resolution copper X-ray spectrum consists of components labeled as $K_{\alpha 1}$ (1.54056Å) and $K_{\alpha 2}$(1.54439Å). The most commonly used target element is Cu but Mo, Cr, Fe, Co, Ag and W are also used for specialist applications . Cu tube is the most common choice for routine analysis, which gives X-rays of shortest wavelength above 1A°. Also relatively high power can be applied to the target because of the good thermal conductivity of copper.

Table 1. Approximate principle emission lines for various anode targets.

Anode	Cu	Mo	Cr	Fe	Co	Ag	W
$\lambda(K_\alpha)$ Å	1.54	0.71	2.29	1.94	1.79	0.56	0.21

1.2. Rietveld refinement

The development of Rietveld method in 1969 breaks out the application of powder diffraction method as a quantitative tool. Rietveld method is a powerful technique that makes use of the entire powder pattern instead of analyzing individual, non-overlapped, diffraction peaks for crystal structure refinement. The advantage of this method is that it calculates the entire powder pattern of a crystalline model, including various experimental and sample dependent effects. Rietveld method essentially tries to fit a structural model based on a number of crystal structure parameters to the experimental diffraction data. This model utilizes a least-squares approach where various parameters such as lattice parameters, atomic positions and parameters such as peak shape, background, scale

factors, peak broadening, that describe the experimental and sample conditions, are allowed to vary to reach an agreement between the calculated and measured diffraction profiles. However to employ this method, a good initial knowledge of the structure is needed which is refined by small adjustments. The method can be utilized to refine several powder or single crystal diffraction data including reactor neutron data, laboratory X-ray powder diffraction data, synchrotron powder diffraction data, time-of-flight neutron data from pulsed spallation sources, and to refinements of magnetic structures. Rietveld analysis is carried out mostly for the determination the structural parameters, but increasingly, the method is also used to determine relative amounts of the crystallographic phases, the preferred orientation, residual stress, crystallite size etc. This method further helps to quantitatively detect small amounts of polymorphic phases which are of great interest especially for pharmaceutical research and in the concrete business. Currently various softwares are available for the Rietveld refinement such as GSAS, GSAS-EXPGUI, Fullprof, TOPAS, JANA2000, Rietan etc.

2. Solid state nuclear magnetic spectroscopy.

The non-averaged anisotropic interactions in solid samples make the solid state NMR spectrum very broad with poor resolution. But the anistotropic interactions in the solid-state NMR are rich in information about the system under study. Chemical shift anisotropy gives atomic orientation information in a molecule while dipolar coupling give both orientation and distance information. These anisotropic interactions are measured directly or indirectly using specialized pulse sequences and are used to determine information about structure, geometry and dynamics. In diamagnetic materials, the external magnetic field induces a circulation of electronic current around the nucleus. The circulation of electronic current generates a magnetic field around the nucleus which shields the nuclei from complete exposure to external magnetic field and this shielding is responsible for chemical shift. Nuclei having different chemical environment have different electronic environments and therefore different chemical shifts. As a result, chemical shift is used as a probe for molecular structure information in NMR.

Quadrupolar interaction is observed in nuclei whose spin quantum number is greater than ½ (I> ½). It originates from the interaction of the nuclear quadrupolar

moment with the surrounding electric field gradient (EFG) tensor, and the coupling observed is called the nuclear quadrupolar coupling. Nuclear quadrupolar coupling is a function of both nuclei (nuclear quadrupolar moment) and electric field environment (EFG). The coordination geometries of metals possess quadrupolar moment in solids can be determined using solid state NMR. The various chemical shift corresponding to various geometries can be identified. The area under the peak in the NMR spectra gives the fraction of occupancy of the particular ion in that environment.

In solution-state NMR, the anisotropic interactions are averaged by fast tumbling motions of the molecules inside the solvent. When the tumbling rates are faster than the width of nuclear spin interactions, a narrow spectrum is generated. In the solid-state, the tumbling motions of molecules are absent; hence the anisotropic interactions survive resulting in a broad NMR spectrum. Mechanical spinning technique called Magic Angle Spinning (MAS) for resolution enhancement in solid-state NMR, where the sample is spun at an axis inclined 54.74° with respect to the external magnetic field. With magic angle spinning, sharp peaks similar to that of solution-state are achieved in solid-state NMR. MAS achieve this by averaging the anisotropic part of different internal spin interactions such as chemical shift, direct dipole-dipole coupling etc.

3. Extended X ray Absorption Fine structure

Through a photoelectric process the x-rays can be absorbed by all matter. Thereby the energy of the X-ray photon is used to excite a core-electron and the atom is left in an excited state with an empty electron orbital (a core hole). The excited electron is called photo-electron and the kinetic energy of this electron $E_{K.E.}$ equals the difference of the energy from the photon $\sim\omega$ and the binding energy of the electron $E_{B.E.}$ ($E_{K.E.} = \sim\omega - E_{B.E.}$). The probability that an X-ray photon is absorbed by the radiated material is given by the absorption coefficient μ and it can be observed that μ increases strongly when the X-ray energies equal the bonding energies $E_{B.E.}$ of a core-electron of an element in the investigated material.

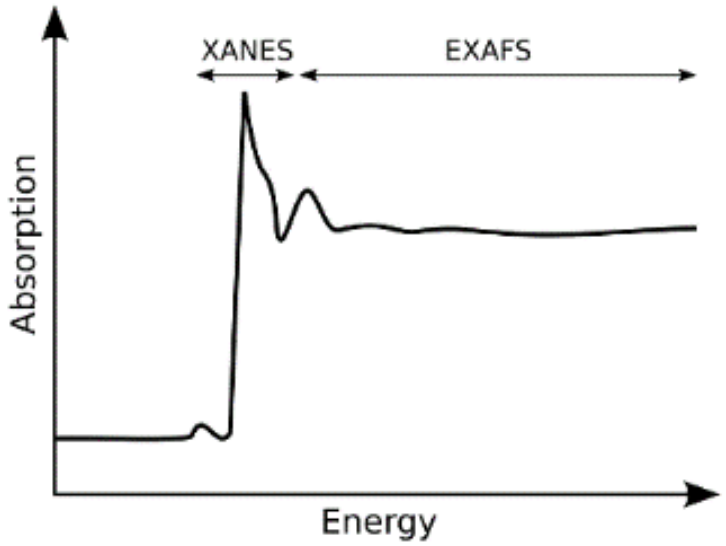

Figure 2. X ray absorption spectrum.

These step-like features in an absorption spectrum are called absorption edges. X-ray absorption spectra measured at condensed matter show oscillations just above the absorption edge. These oscillations are called X-ray absorption fine structure and result from the fact that in condensed matter all atoms are embedded in a defined structure with neighbouring atoms at specified distances. The absorption spectra contain information on the structure of the investigated material. The information content depends on the x-ray energy with respect to the binding energy of the electron E_i and thus the spectrum can be divided into two parts: the X-ray absorption near edge structure (XANES) and the extended X-ray absorption fine structure (EXAFS).

The near edge structure extends up to 50 eV above the absorption edge. In this energy region the core electron is excited to an unoccupied bound state, so that the shape of the absorption edge depends on the density of states closely above the Fermi level. Therefore, the oxidation state and binding geometry affect the XANES part of the spectrum. The region from 50 eV-1000 eV above an absorption edge is called extended X-ray absorption fine structure. This part of the spectrum contains information on the types and number of neighbour atoms to the absorbing atom.

In order to take care of the oscillations in the absorption spectra, it has been converted to absorption function defined as follows

$$\chi(E) = \frac{\mu(E) - \mu_0(E)}{\Delta\mu_0(E_0)} \qquad (1)$$

Where E_0 absorption edge energy, $\mu_0(E_0)$ is the bare atom background and $\Delta\mu_0(E_0)$ is the step in $\mu(E)$ value at the absorption edge. The energy dependent absorption coefficient $\chi(E)$ has been converted to the wave number dependent absorption coefficient using relation,

$$K = \sqrt{\frac{2m(E - E_0)}{\hbar^2}} \qquad (2)$$

where m is the electron mass. $\chi(k)$ is weighted by k to amplify the oscillation at high and the χ(k)k functions are fourier transformed in R space to generate the $\chi(R)$ versus R spectra in terms of the real distances from the center of the absorbing atom. The set of EXAFS data analysis available in within IFEFFIT software package have been widely used for EXAFS data analysis. This includes background reduction and Fourier transform to derive the $\chi(R)$ versus R spectra from the absorption spectra (using ATHENA software), generation of the theoretical EXAFS spectra starting from an assumed crystallographic structure and finally fitting of experimental data with the theoretical spectra using ARTEMIS software.

4. Scanning Electron Microscopy

Scanning electron microscopy (SEM) is one of the most widely used techniques for characterization of nanomaterials and nanostructures. The resolution of the SEM approaches a few nanometres, and the instruments can operate at A magnifications that are easily adjusted from ~10 to over 300,000. This technique provides not only topographical information like optical microscopes do, but also information of chemical composition near the surface. A scanning electron microscope can generate an electron beam scanning back and forth over a solid sample. The interaction between the beam and the sample produces different types of signals providing detailed information about the surface structure and morphology of the sample. When an electron from the beam encounters a nucleus in the sample, the resultant columbic attraction leads to a deflection in the electron's path, known as Rutherford elastic scattering. A fraction of these electrons

will be completely backscattered, remerging from the incident surface of the sample. Since the scattering angle depends on the atomic number of the nucleus, the primary electrons arriving at a given detector position can be used to produce images containing topological and compositional information. The high-energy incident electrons can also interact with the loosely bound conduction band electrons in the sample. However, the amount of energy given to these secondary electrons as a result of the interactions is small, and so they have a very limited range in the sample. Hence, only those secondary electrons that are produced within a very short distance from the surface are able to escape from the sample. As a result, high-resolution topographical images can be obtained in this detection mode.

5. UV-visible Spectroscopy

Absorption spectroscopy in the visible region has long been an important tool to the analyst [11]. Appearance of colour arises from the property of the colored material to absorb selectively and reflect its complementary colour which falls within the visible region of the electromagnetic spectrum. Absorption of energy leads to a transition of electron from ground state to an excited state which is governed by the following equation

$$\Delta E = h\nu = hc/\lambda \quad (2.11)$$

where h represents Planck's constant, ν is the frequency of radiation, c is the velocity of light and λ is the radiation wavelength. Thus from the equation it seems that the UV-energy is quantized and hence a single discrete line should be obtained from a single electronic spectrum. However, this is not the case of reality as excitation of electronic energy levels would also involve excitation of the embedded vibrational and rotational energy levels of an atom, thus giving rise to a broad absorption band [12]. The intensity of the absorption band depends on three factors namely (a) transition probability, (b) population of states and (c) concentration or path length.

Almost all relationships between intensities of incident and transmitted radiation and the concentration and path-length is governed by Beer-Lambert's law which is written as

$$I = I0 \exp(-\kappa cl)$$

$$\log(I0/I) = A = \kappa cl \quad (2.12)$$

where I = Intensity of the emitted radiation, I0 = Intensity of the incident radiation, κ = constant, c = concentration and l = path length. A is known as the absorbance or the optical density and κ, the constant generally represented as ε, known as the molar absorption coefficient.

In a dual beam spectrophotometer, light from either the visible or ultraviolet source enters the grating monochromator before it reaches the filter. Broad band filters contained in a filter wheel are automatically indexed into position at the required wavelengths to reduce the amount of stray light and unwanted orders from the diffraction grating. The light from the source is alternatively split into one of the two beams by a rotating mirror called a chopper; one beam is passed through the sample and the other through the reference. The detector alternately sees the beam from the sample and then the reference. Its output which ideally would be an oscillating square-wave gives the ratio of I to Io directly i.e. the reference correction is made automatically.

Array-detector spectrophotometers allow rapid recording of absorption spectra. Dispersing the source light after it passes through a sample allows the use of an array detector to simultaneously record the transmitted light power at multiple wavelengths. These spectrometers use photodiode arrays as the detector. The light source is a continuum source such as a tungsten lamp. All wavelengths pass through the sample. The light is dispersed by a diffraction grating after the sample and the separated wavelengths fall on different pixels of the array detector. The resolution depends on the grating, spectrometer design, and pixel size, and is usually fixed for a given instrument.

Diffuse reflectance UV-Vis measurements were performed on a spectrophotometer with Teflon pellet as the reference material.

6. Adsorption Isotherm and BET Method for surface area measurement

When a gas or vapour phase is brought into contact with a solid, part of it is remains on the outside attached to the surface. In some cases the gas molecules (referred as adsorbate) are attached to the solid surface (refered as adsorbent) by a weak Vander Waals attraction. This type of adsorption known as physisorption (physical adsorption) can be utilized to characterise materials allowing for the determination of specific surface area, pore size distribution and pore volume.

The specific surface area of a powder is determined by measuring the amount of adsorbate gas corresponding to a monomolecular layer on the surface usually at the temperature of liquid nitrogen. The amount of gas adsorbed can be measured by a volumetric or continuous flow procedure. The most common adsorbate used is nitrogen; however, other adsorbates like Ar, CO, CO_2, O_2 are also used in some instances.

In 1938, S. Brunauer, P. H. Emmett, and E. Teller put forward a theory known as Brunauer–Emmett–Teller (BET) theory to explain the physisorption of gas molecules on a solid surface which forms the basis for the technique for the determination of the specific surface area of a material. The theory is based on the following hypotheses:

(a) Gas molecules physically adsorb on a solid in layers infinitely.

(b) There is no interaction between each adsorption layer.

(c) The Langmuir theory can be applied to each layer.

(d) Uppermost layer is in equilibrium with vapor phase.

(d) First layer adsorption is governed by the heat of adsorption while heat of condensation can use for higher layers.

With these assumptions, the following equation known as BET equation is derived.

$$1/\{v[(p_0/p)-1]\} = [(c-1)/v_m c]\ (p/p_0) + (1/v_m c),$$

where, p and p_0 are the equilibrium and the saturation pressure of adsorbates at the temperature of adsorption, v is the volume of adsorbed gas, v_m is the monolayer adsorbed gas quantity and c is the BET constant given as

$$c = \exp[(E_1-E_L)/RT],$$

where E_1 is the heat of adsorption for the first layer, and E_L is that for the second and higher layers and is equal to the heat of liquefaction.

The BET Equation is an adsorption isotherm and a straight line can be plotted (only in the p/p_0 range 0.05-0.35) known as BET plot with the factor $1/v[(p_0/p)-1]$ on the y-axis and p/p_0 on the x-axis. The value of v_m and c can be calculated from the values of slope (A) and Y-intercept (I) using the equations,

$$v_m = 1/(A+I) \text{ and } c = 1+ (A/I)$$

The BET method is widely used for the calculation of surface areas of solids in heterogeneous catalysis where the number of active sites depends on the surface area which in turn related to particle size, particle morphology, surface texturing and porosity.

The total surface area (S_{total}) and the specific surface area ($S_{BET)}$ are then given by

$$S_{total} = (v_m N s)/V \quad \text{and} \quad S_{BET} = S_{total}/ a,$$

where N is the Avogadro's number, s the adsorption cross section of the adsorbing species, V the molar volume of the adsorbate gas, and a the mass of the solid sample or adsorbent.

The single-point method may be employed directly for a series of powder samples of a given material for which the material constant C is much greater than unity.

7. Electrochemical Impedance Spectroscopy

Electrochemical impedance spectroscopy (EIS) is a very versatile electrochemical tool to characterize intrinsic electrical properties of any material and its interface. This is a steady state method measuring the current response to the application of an ac voltage as a function of the frequency. The basis of impedance spectroscopy is the analysis of the impedance (resistance of alternating current) of the observed system with respect to the applied frequency and applied signal. An important advantage of EIS over other techniques is the possibility of using tiny ac voltage amplitudes exerting a very small perturbation on the system. EIS provides quantitative information about the conductance, dielectric coefficient and some interfacial properties. Also this has been widely employed to study the kinetics of electrochemical and photoelectrochemical processes including the elucidation of salient electronic and ionic processes occurring in the DSC. EIS data for electrochemical cells are most often represented in Nyquist and Bode plots. Bode plots refer to representation of the impedance magnitude (or the real or imaginary components of the impedance) and phase angle as a function of frequency. Because both the impedance and the frequency often span orders of magnitude, they are frequently plotted on a logarithmic scale. Bode plots explicitly show the frequency-dependence of the impedance of the device under test. A complex plane or Nyquist plot depicts the imaginary impedance, which is indicative of the capacitive and inductive character of the cell, versus the real impedance of the cell. Nyquist plots have the advantage that activation-controlled processes with distinct

time-constants show up as unique impedance arcs and the shape of the curve provides insight into possible mechanism or governing phenomena. The flat band potential can be calculated using a circuit which fits for the Nyquist plot. From which the capacitance (C) at various voltages can be measured. 1/C vs voltage gives rise to Mott-Schottkey plot. Using this plot flat band potential can be measured.

8. X-ray photoelectron spectroscopy

X-ray Photoelectron Spectroscopy (XPS) or Electron Spectroscopy for Chemical Analysis (ESCA) is based on the principle that when X-rays hi atoms, electrons are ejected. It is a typical surface-sensitive technique as only electrons that are generated in the top few atomic layers (mean free path ~1.5 nm) are detected, even though the absorption length of the X-rays is about 100 - 1000 nm. The technique provides quantitative information about the elemental composition of the surface of all kinds of solid material like insulators, conductors, polymers etc. The sample material is irradiated with monoenergetic soft x-rays causing electrons to be ejected. The measurement of kinetic energies of these ejected photoelectrons helps in the identification of the elements in the sample as each element produces a characteristic set of XPS peaks at characteristic binding energy values. All elements except H and He can be detected. Moreover the relative concentrations of elements can be determined from the photoelectron intensities. The most important advantage of XPS is its ability to obtain information on chemical states from the variations in binding energies, or chemical shifts, of the photoelectron lines. Most modern instruments have detection limits for most of the elements in the parts per thousand ranges. Detection limits of parts per million (ppm) are possible under special conditions such as concentration at top surface or very long collection time.

In XPS, soft X-rays with energies range from 200-2000 eV are used. The development of synchrotron radiation sources has enabled high resolution studies with much wider and more complete energy range (5 - 5000 eV). A sample placed in ultra-high vacuum is irradiated with photons of energy, hν. Electrons of the atoms on the surface absorb the photons and leave the atom by using some of its energy to overcome the

coulomb attraction of the nucleus, reducing its KE by its initial state BE. The kinetic energy of the ejected electron is related to the energy of the X-ray photon as

$$KE = h\nu - BE - \Phi$$

where BE represents the binding energy of the atomic orbital from which the electron ejected and Φ is the spectrometer work function which is an adjustable instrumental correction factor that accounts for the few eV of KE loss of the photoelectron as it becomes absorbed by the instrument's detector. An electron energy analyzer measures the kinetic energy distribution of the emitted photoelectrons and a photoelectron spectrum can thus be recorded.

The number of detected electrons is a measure for the elemental concentration. Atomic concentrations can be obtained by dividing the peak areas by standard sensitivity factors and normalizing to 100%. For bulk materials the surface concentraions can be determined with a 20% inaccuracy. However, in most cases, the surface composition varies as a function of depth, where the signal of an element in a lower layer will be attenuated more strongly than that in the top layer. In such cases either angle-resolved measurements or model calculations are performed to extract quantitative information.

The basic requirements for a XPS experiment are:

1. A fixed-energy radiation source. The most commonly employed X-ray sources are those giving rise to Mg Kα radiation (hν = 1253.6 eV) and Al Kα radiation (hν = 1486.6 eV).

2. An electron energy analyser. This separates the emitted electrons according to their KE, and measures the flux of emitted electrons of a particular energy. The most preferred design is a concentric hemispherical analyser (CHA) where an electric field is applied between two hemispherical surfaces to disperse the electrons according to their KE

3. A high vacuum environment which enables the emitted photoelectrons to be analysed without interference from gas phase collisions. XPS detectors must be operated under ultra-high vacuum (UHV, $P < 10^{-9}$ millibar) conditions in order to count the number of electrons with a minimum of error, as they are kept one meter away from the sample.

Appendix 2

2.1. Flat band potentials of IGZ1, IGZ2, IGZ3 and IGZ4 were calculated using the equation,

$$V_{fb} = EA - E_{ref} + 1/2Eg$$

Where V_{fb} is the flat band potential, EA is the electron affinity of the individual atom, E_{ref} is the energy of free electrons on the hydrogen scale, E_{ref}= 4.5 eV and Eg is the band gap of the material

For IGZ1 ($InGaO_3(ZnO)_1$)

$EA=((X_{In}) * (X_{Fe})*(X_{Zn})*(X_o)^4)^{1/7}$

Where $X_{In,}$ $X_{Ga,}$ $X_{Zn,}$ X_o are the electronegativities in Mulliken scale of Indium, Gallium, Zinc and Oxygen respectively.

The detailed calculation is given below

X_{In} = 3.1 eV

X_{Ga} = 3.2 eV

X_{Zn} = 4.45 eV

X_o = 7.53 eV

Band gap of IGZ1 is 3.7 eV

$EA = (3.1 \times 3.2 \times 4.45 \times (7.53)^4)^{1/7}$

= 5.4451 eV

Vfb = 5.4451 - 4.5 + (½ x 3.7)

= 2.7951 eV

For IGZ2 ($InGaO_3(ZnO)_2$)

$EA = (3.1 \times 3.2 \times (4.45)^2 \times (7.53)^5)^{1/9}$

= 5.5196 eV

Vfb =5.5196 - 4.5 + (½ x3.6)

= 2.8196 eV

For IGZ3 ($InGaO_3(ZnO)_3$)

EA = $(3.1 \times 3.2 \times (4.45)^3 \times (7.53)^6)^{1/11}$

= 5.5676 eV

Vfb = 5.5676- 4.5 + (½ x3.9)

= 3.0176 eV

For IGZ4 ($InGaO_3(ZnO)_4$)

EA = $(3.1 \times 3.2 \times (4.45)^4 \times (7.53)^7)^{1/13}$

=5.6010 eV

Vfb = 5.6010- 4.5 + (½ x3.022)

= 3.101 eV

2.2. Calculation of V_{fb} using Impedance spectroscopy

$[Fe(CN)_6]^3/[Fe(CN)_6]^{4-}$ is the redox couple involved in the charge transfer, which is represented by a resistance (R_{CT}) in the Randle's circuit. There will a generation of non-faradaic electrode capacitance due to IGZ1 electrode which can be represented by a constant phase element Z_{CPE} parallel to R_{CT}. Warburg impedance, Z_W, is incorporated in parallel with R_{CT} which takes into account diffusion of electroactive species towards the electrode.

The impedance of a CPE in an ac circuit, Z_{CPE}, can be represented by an equation,

$$Z_{CPE} = \sigma\omega^{-m}\left[\cos\left(\frac{m\pi}{2}\right) - j\sin\left(\frac{m\pi}{2}\right)\right]$$

where σ is the CPE prefactor, ω is the angular frequency (ω = 2πf), m is the CPE exponent (0 ≤ m ≤ 1), and j is the imaginary number (j = √-1). It can be said that if m = 1 then Z_{CPE} represents an ideal capacitor, Z_C.

Above equation implies, if m=1,

$$Z_C = -1/j\omega C$$

$$1/C^2 = Z^2_C\omega^2$$

$$= Z^2_C 4\pi^2 f^2$$

$1/C^2$ is calculated for each voltage. Mott-Schottky plot was constructed with $1/C^2$ Vs Voltage.

2.3. Indexed PXRD pattern of $ZnFe_2O_4$

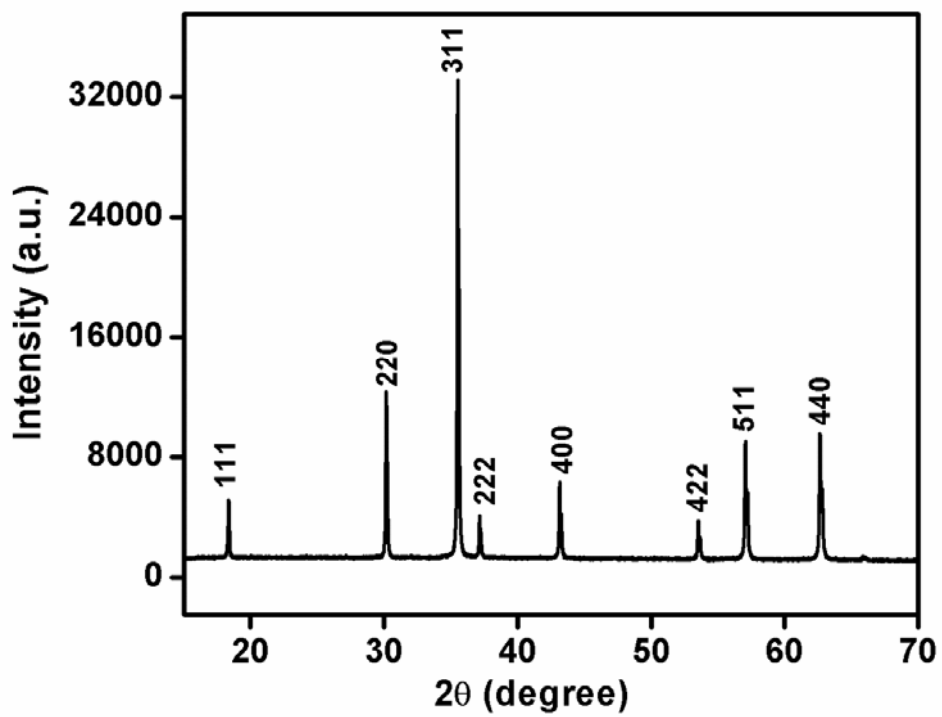

2.4. Flat band potential of IFZ1, IFZ2, IFZ3 and IFZ4 were calculated using the equation,

$$V_{fb} = EA - E_{ref} + 1/2Eg$$

Where Vfb is the flat band potential, EA is the electron affinity of the individual atom, Eref is the energy of free electrons on the hydrogen scale, Eref= 4.5 eV and Eg is the band gap of the material

For IFZ1 ($InFeO_3(ZnO)_1$)

$EA=((X_{In}) * (X_{Fe})*(X_{Zn})*(X_o)^4)^{1/7}$

Where $X_{In}, X_{Fe}, X_{Zn}, X_o$ are the electronegativities in mulliken scale of Indium, Iron, Zinc and Oxygen respectively.

The detailed calculation is given below

X_{In} = 3.1 eV

X_{Fe} = 4.06 eV

X_{Zn} = 4.45 eV

X_o = 7.53 eV

Band gap of IFZ1 ($InFeO_3(ZnO)_2$) is 2.85 eV

$EA = (3.1 \times 4.06 \times 4.45 \times (7.53)^4)^{1/7}$

= 5.6364 eV

Vfb = 5.6364 - 4.5 + (½ x 2.85)

= 2.56 eV

For IFZ2 ($InFeO_3(ZnO)_2$)

$EA = (3.1 \times 4.06 \times (4.45)^2 \times (7.53)^5)^{1/9}$

= 5.6676eV

Vfb =5.6676 - 4.5 + (½ x2.96)

= 2.64eV

For IFZ3 ($InFeO_3(ZnO)_3$)

EA = $(3.1 \times 4.06 \times (4.45)^3 \times (7.53)^6)^{1/11}$

= 5.6894eV

Vfb = 5.6894- 4.5 + (½ x2.97)

= 2.67eV

For IFZ4 ($InFeO_3(ZnO)_4$)

EA = $(3.1 \times 4.06 \times (4.45)^4 \times (7.53)^7)^{1/13}$

=5.7045 eV

Vfb = 5.7045- 4.5 + (½ x3.022)

= 2.71eV

2.5. Determination of formula of the **aISCoZn** using Rietveld refinement as well as TGA data.

Weight of the residue obtained at 500 °C from TGA analysis **= 2.4466 mg**

2.4466 mg of **aISCoZn** is used for XRD analysis.

From Rietveld refinement,

Phase fraction of **ZnO = 90.77%**

So number of mole of ZnO in 2.4466 mg **= 2.4466 x 90.77/100 = 2.22**

Phase fraction of $Co_{2.04}Zn_{0.96}O_4$ **= 9.23%**

So number moles of $Co_{2.04}Zn_{0.96}O_4$ **= 2.4466 x 9.23/100 = 0.2258**

In the final residue there will be **(2.22+(0.22588 x 0.96)) Zn ~ 2.44 Zn**

In the same way, there will be **0.2258 x 2.04 Co ~ 0.46 Co**

i.e.; $Zn_{2.44}Co_{0.46}O_{3.1232}$ will be the composition (2.22 ZnO and 0.2258 $Co_{2.04}Zn_{0.96}O_4$) of the final residue in TGA.

Molecular weight of the composition $Zn_{2.44}Co_{0.46}O_{3.1232}$ **= 235.059.**

Total weight of Zn and Co in Zn in 235.059 **= 185.376**

The percentage weight loss results in this final residue composition **= 6.1525%**

Let Z be the molecular weight of the residue at 286 °C (which is the temperature corresponds to the previous weight loss),

Z-(Z x 6.1525/100) **= 235.059** (weight of 2.22 ZnO and 0.2258 $Co_{2.04}Zn_{0.96}O_4$)

Z **= 250.4891**

The weight loss due to OH^- **= 250.4891 – 185.376**

= 65.1131

No. of OH^- **= 65.1131/17**

= 3.83

Now the composition at 286 °C is $Zn_{2.44}Co_{0.46}(OH)_{3.83}$ (Charge is not balanced)

The weight loss at 286 °C is assumed to be due to the loss of NO_3-, No. of NO_3^- can be obtained by balancing the charge in the composition $Zn_{2.44}Co_{0.46}(OH)_{3.83,}$

i.e.; (2.44+0.46) x 2 – 3.83 **= 1.97**